Inhibition of gap junctions as a novel treatment strategy for medulloblastoma

Doctoral thesis

to obtain a doctorate (PhD)

from the Faculty of Medicine

of the University of Bonn

Meng-Chun Hsieh

from New Taipei City/Taiwan

2025

Written with authorization of

the Faculty of Medicine of the University of Bonn

First reviewer: PD Dr. med. Matthias Schneider

Second reviewer: Prof. Dr. Michael Hölzel

Day of oral examination: 13.06.2025

From the Clinic and Policlinic for Neurosurgery of the University Hospital Bonn

Table of Contents

List of abbreviations

Abbreviation	Full name
Adj. p-value	Adjusted p-value
ATRT	Atypical teratoid/rhabdoid tumor
B.B.B.	Blood-brain barrier
BCA	Bicinchoninic Acid
BE	Bystander effect
BrdU	Bromodeoxyuridine
BSA	Bovine serum albumin
CCNU	Chlorethyl-Cyclohexyl-Nitroso-Urea
cGAMP	2’3’-cyclic GMP-AMP
CNS	Central nervous system
CRISPR/Cas9	CRISPR, Clustered Regularly Interspaced Short Palindromic Repeats/ Nuclease 9
CSI	Craniospinal irradiation
CT	Computed tomography
CTNNB1	Catenin β-1
Cx	Connexin
D283	D283Med
DEGs	Differentially expressed genes
DMSO	Dimethyl sulfoxide
DPBS	Dulbecco's Balanced Salt Solution
ECM	Extracellular microenvironment
FBS	Fetal bovine serum
FC	Fold change
GFI1	Growth factor independent 1
GJ	Gap junction
GJA1	Gene encoding for Cx43
Glioblastoma	Glioblastoma, CNS WHO grade 4, IDH-wildtype
GO	Gene ontology
GSEA	Gene set enrichment analysis
h/hrs	Hour/hours
HC	Hexameric hemichannels
HSVtk/GCV	Herpes simplex virus thymidine kinase/ ganciclovir

IC50	Half maximal inhibitory concentration
IF	Immunofluorescence
kDa	Kilodaltons
KO	Knockout
MB	Medulloblastoma
MBEN	Medulloblastoma with extensive nodularity
Med8A	MEB-MED8A
MFA	Meclofenamic acid
Mins	Minutes
MRI	Magnetic resonance imaging
mRNA	Messenger RNA
MTT	3-(4,5-dimethylthiazol-2-yl)-5-(3-carboxymethoxyphenyl)-2-(4-sulfophenyl)-2H-tetrazolium
MuLE	Multiple Lentiviral Expression
MYC	Myelocytomatosis oncogene
MYCN	Myelocytomatosis oncogene, neuroblastoma-derived
NSAIDs	Nonsteroidal anti-inflammatory drugs
OD	Optical density
OS	Overall survival
PCA	Principial component analysis
PF	Posterior fossa
PI	Propidiumiodide
ROI	Regions of interest
RT	Room temperature
SDS	Sodium dodecyl sulfate
sgRNA	Single guide RNA
SHH	Sonic hedgehog
SMO receptor	Smoothened receptor
TM	Tumor microtube
TME	Tumor microenvironment
TMZ	Temozolomide
TO	Tonabersat
TP53	Tumor protein 53
WB	Western blot
WHO	World Health Organization
WNT	Wingless
ZsG	ZsGreen

1. Introduction

1.1. Tumor networks

1.1.1. The role of tumor networks in oncology

In recent years, the discovery of functional and communicative tumor networks has refined our understanding of oncology (Maas and Douw, 2023; Venkataramani et al., 2022). Within brain tumors, these networks comprise cells that are spatially interconnected with one another and with the surrounding microenvironment. They play crucial roles in processes such as tissue development, homeostasis, and disease progression (An et al., 2021; Bonifazi et al., 2009; Chen et al., 2022; Venkataramani et al., 2022; Zhou et al., 2017). These cell-to-cell connections also serve as a bridge between local and distant areas of the tumor (Douw et al., 2011).

Initially described in malignant astrocytic brain tumors, tumor networks have since been identified in a variety of cancer types, including pancreatic and colon carcinomas (Desir et al., 2019; Latario et al., 2020; Osswald et al., 2015). As research progresses, these networks have become a focal point in neuro-oncology. For instance, gliomas form intricate tumor networks that are electrically active and integrate into the brain's neural circuitry. This integration occurs via specialized mechanisms, such as neuron-tumor synapses, which facilitate communication between glioma cells and surrounding brain tissue (Maas and Douw, 2023).

Besides neuron-tumor synapses, communication within homotypic tumor networks relies on various cellular mechanisms, among which gap junctions (GJs) play a particularly critical role. GJs facilitate direct intercellular signaling by enabling the exchange of ions, metabolites, and signaling molecules between tumor cells (Osswald et al., 2015). This synchronized cellular behavior supports metabolic cooperation, enhances therapy resistance, and contributes to tumor progression. Understanding the role of GJs in tumor

networks is essential for uncovering their impact on cancer development and identifying potential therapeutic targets.

1.1.2. The role of GJs and connexins in cellular communication and cancer progression

GJs were firstly identified in the heart and liver of mice in 1967 (Revel and Karnovsky, 1967). Supported by substantial evidence, intercellular GJs have been suggested to coordinate the communication between cells (**Figure 1**) (Osswald et al., 2015; Vicario et al., 2017). This connectivity contributes to self-repair, regulation of cell growth, cell differentiation, and homeostasis maintenance (Kandouz and Batist, 2010; Oliveira et al., 2022; Osswald et al., 2015). Moreover, cell-to-cell communication relies on GJs to exchange small molecules (less than 1.2–1.5 kDa), such as micro-RNA, glutamate, glucose, ATP, cAMP, IP3, and ions. These junctions also facilitate the transmission of signaling and electrical impulses to adjacent cells (Hong et al., 2015; Hu et al., 2013; Le et al., 2014; Leybaert et al., 2017; Linkous et al., 2019; Osswald et al., 2015). Meanwhile, GJs enable tumor cells to communicate with benign surrounding cells, such as stromal cells, immune cells, and neural cells, thereby creating a tumor microenvironment (TME) (Osswald et al., 2015; Virtuoso et al., 2024). Therefore, GJs are believed to play a crucial role in contributing to tumorigenesis, resistance, and recurrence of malignant tumors (An et al., 2021; Le et al., 2014; Osswald et al., 2015).

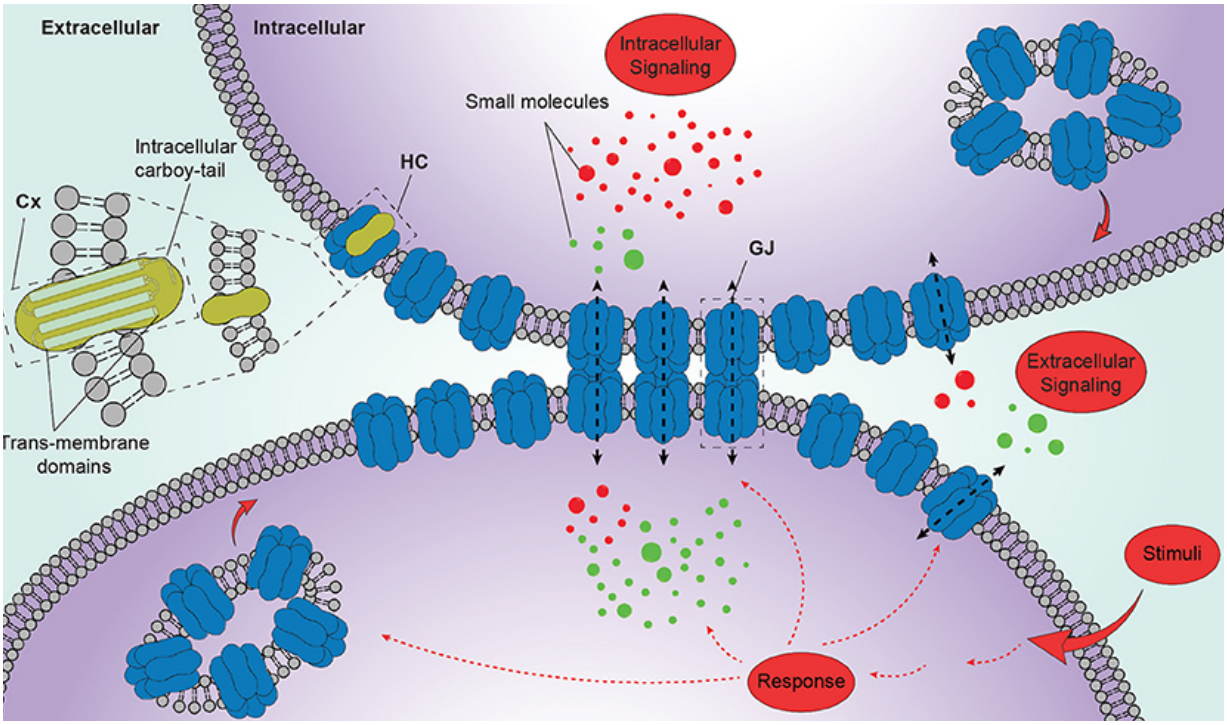

Figure 1. Schematic representation of GJs function. GJs facilitate the exchange of molecules and signals between cells, enabling effective intercellular communication (modified from (Vicario et al., 2017)).

The connexin (Cx) family was identified following the recognition of GJs. Many scientific studies aimed to understand the biophysical properties of Cx proteins (Goodenough, 1974; Goodenough and Stoeckenius, 1972; Oliveira et al., 2022). Cx is a transmembrane protein found in nearly all human cell types, particularly in the heart, liver, and brain (Leybaert et al., 2017). There is a total of 21 Cx genes identified in the human genome and followed by a numerical value corresponding to the molecular mass of the predicted polypeptide in kilodaltons (kDa), including Cx26, Cx43, Cx34, and other Cx members (Beyer and Berthoud, 2018; Leithe et al., 2018; Qi et al., 2023). A hemichannel (HC), also known as a connexon, is composed of six Cx subunits and is embedded in the cell membrane. When two HCs align and interact, they form a GJ, allowing intercellular communication (**Figure 2**) (Leithe et al., 2018). HCs can be further differentiated into homomeric or heteromeric

HCs, with the former formed between the same cell type and the latter formed between different cell types (Vicario et al., 2017).

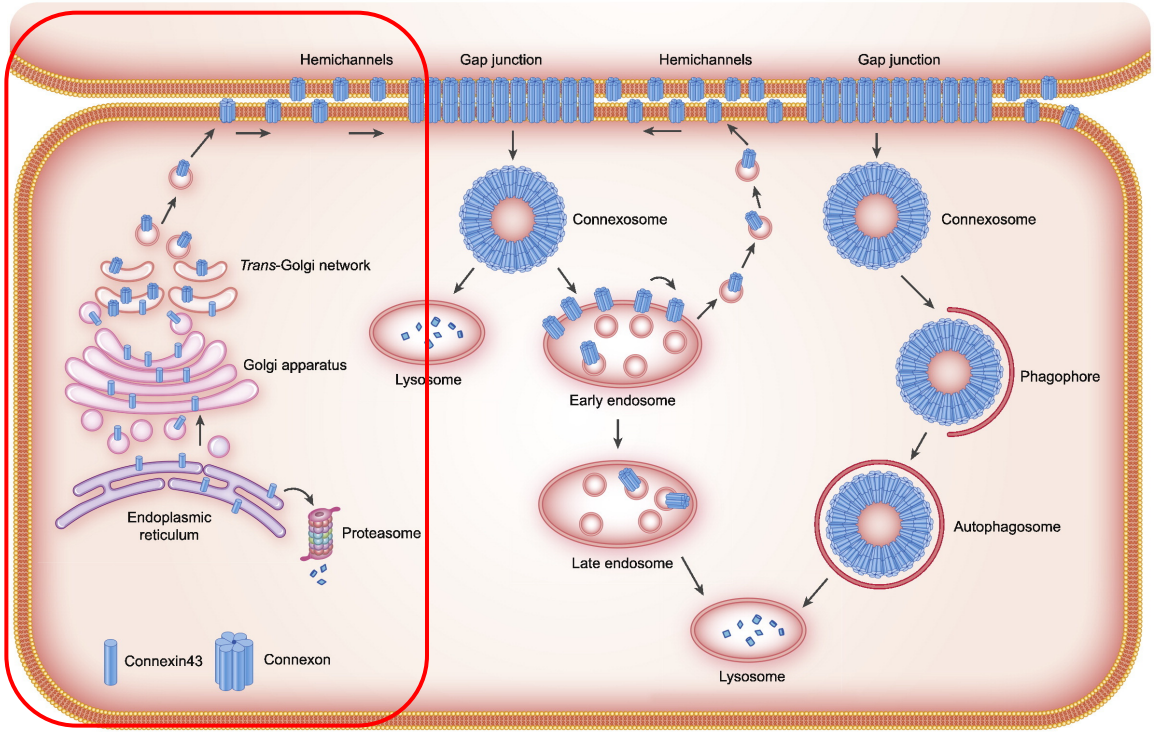

Figure 2. The schematic illustration of Cx protein intracellular trafficking. Cx proteins are synthesized in the endoplasmic reticulum. Six Cx oligomers assemble into a connexon in the trans-Golgi network. Connexons are then transported to the plasma membrane as HCs, and two opposing HCs form GJs. (as marked in red box, modified from (Leithe et al., 2018)).

Cx43 (43 kDa, GJA1) clone was isolated from rat heart tissue in 1987, it is recognized as the most expressed Cx protein. Cx43 is a transmembrane protein that is widely expressed in over half of the human organs, with particularly high prevalence in the central nervous system (CNS) (Beyer et al., 1987; Laird and Lampe, 2018; Meier and Rosenkranz, 2014). The Cx43 protein comprises an intracellular amino acid domain (AT), four transmembrane domains (TM), two extracellular loops, and one intracellular loop which contains intracellular amino- (N-tail) and carboxyl-terminal ends (C-tail) (**Figure 3**) (Hu et al., 2013). Like other Cx members, six monomers of Cx43 form connexon embedding in the plasma

membrane and form hexameric HCs. Two hexameric HCs from counterpart cells form a GJ at the intercellular interface (**Figure 2**).

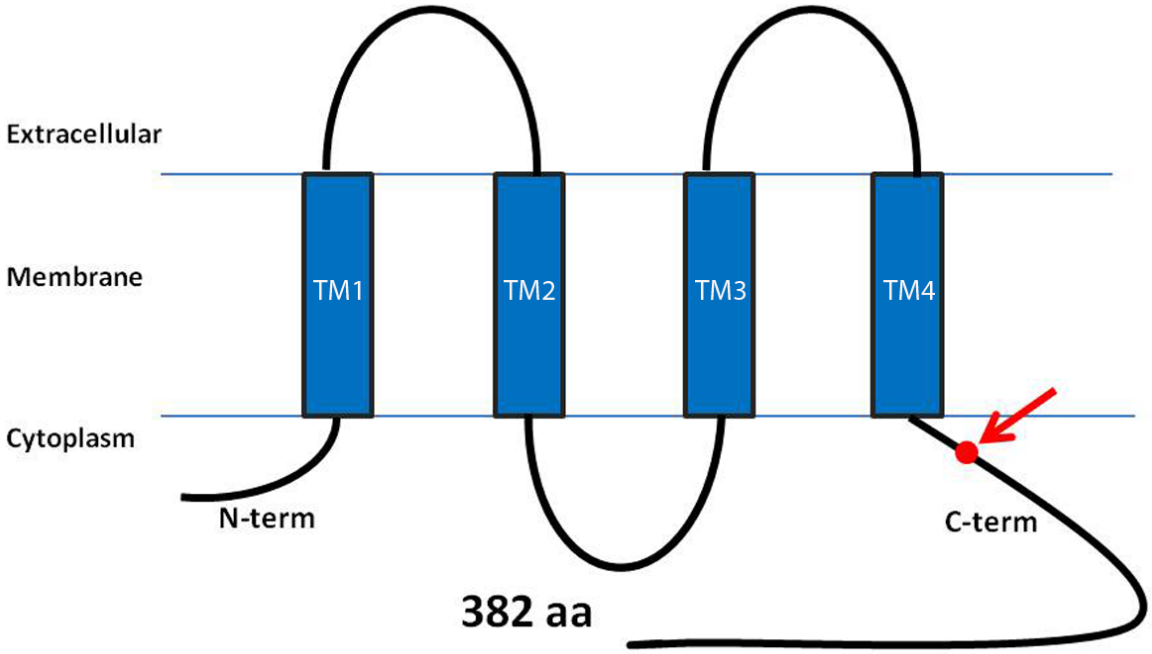

Figure 3. Cx43 protein structure diagram. Cx 43 is a transmembrane protein with four transmembrane domains, two extracellular loops, an intracellular loop, N-term, and C-term (modified from (Bonifazi et al., 2009)).

Cx43-based GJs play a critical role in human. For instance, Cx43 GJs help transmit heart action potentials, facilitate interactions between neurons and glial cells, accelerate the wound repair process, and mediate glial cell responses to CNS injury (Contreras et al., 2004; Laird and Lampe, 2018; Liang et al., 2020; Meier and Rosenkranz, 2014; Qi et al., 2023). Mutant Cx43 expression also links to some diseases (Delmar et al., 2018). Several genetic diseases such as oculodentodigital dysplasia (ODDD), erythrokeratodermia variabilis et progressiva (EKVP), and palmoplantar keratoderma (PKK) are extensively studied in the context of Cx43 abnormalities (Delmar et al., 2018; Shibayama et al., 2005; Srinivas et al., 2019). Given Cx43 unique physiological characteristics, researchers have deeply investigated its therapeutic potential. Several approaches to target Cx43 have

been developed, including Cx43 antibody, peptide mimetics, or the combination with Cx modulators, depending on the cell types and specific illness (Laird and Lampe, 2018; Riquelme et al., 2013). Currently, Cx43-targeted agents for diabetic skin wound healing, reduction of scar formation, retinal injury, and cardiac ischemic injury are evaluated in clinical trials (Laird and Lampe, 2018).

Cx43-based GJs are crucial for maintaining normal tissue homeostasis and play a significant role in oncology and neurooncology. In cancer, Cx43 influences tumor cell communication and modulates the tumor microenvironment, thereby contributing to tumor progression. Beyond these traditional roles, Cx43 is also integral to the formation of tumor microtubes (TMs)—thin membrane extensions derived from tumor cells, first identified by Osswald et al. (Osswald et al., 2015). These structures facilitate the transport of calcium ions and small molecules between cells via Cx43-based GJs. By enabling direct intercellular communication, TMs contribute to the formation of tumor networks, promoting cellular survival and resistance to therapies (Dominiak et al., 2020; Kanaporis et al., 2011; Roehlecke and Schmidt, 2020). Furthermore, Cx43 has been found to be aberrantly expressed in various types of tumors, including those of the liver, prostate, and mammary glands (Wang et al., 2023). Due to its superior capacity for transporting molecules and signaling compared to other Cx family members, Cx43 has emerged as a central focus of oncological research (Dominiak et al., 2020; Kanaporis et al., 2011). Notably, Cx43-linked GJs have been implicated in therapy resistance in glioblastoma (CNS WHO grade 4, IDH-wildtype), where they form functional multicellular networks that enhance tumor resilience and adaptability (Le et al., 2014; Osswald et al., 2015; Sun et al., 2012). Additionally, Cx43 has been linked to facilitating metastasis in various cancers, further underscoring its critical role in tumor progression.

1.1.3. Targeting Cx43-based GJs in tumor progression and metastasis

Notably, GJ communication is not limited to interactions between tumor cells but also extends to benign cells in the surrounding microenvironment, such as astrocytes (McCutcheon and Spray, 2022; Virtuoso et al., 2024). This intercellular communication between carcinoma cells and astrocytes has been implicated in promoting brain metastasis. Increasing evidence has shown that Cx43 contributes to brain metastasis, and the formation of astrocyte–carcinoma GJs has been linked to the ability of carcinoma cells to colonize and survive within the brain (Oliveira et al., 2022; Qi et al., 2023; Vicario et al., 2017; Zhou et al., 2023). Chen et al. mentioned that breast and lung cancer cell lines could engage Cx43 GJs of astrocytes via protocadherin 7 expression (Chen et al., 2016). Through Cx43-mediated GJs, metastatic carcinoma cells can establish connections with astrocytes, facilitating the transfer of ions, metabolites, and other small signaling molecules, such as 2’3’-cyclic GMP-AMP (cGAMP). cGAMP can activate the STING pathway in astrocytes, mediating the secretion of inflammatory cytokines like type-I interferon (IFN) and tumor necrosis factor (TNF). This inflammation further promotes the STAT1 and NF-κB pathways in tumor cells, supporting their growth, chemoresistance, and spread, contributing to the metastatic process (Chen et al., 2016; Schneider et al., 2024). Khair Elzarrad et al. also reported that Cx43 in breast cancer increased adhesion to lung endothelial cells, promoting metastasis to the lung in a murine experimental model (Elzarrad et al., 2008). This has sparked growing interest in exploring Cx43 as a potential therapeutic target for inhibiting metastasis (Chen et al., 2016; Laird and Lampe, 2018; Riquelme et al., 2013; Zhou et al., 2023). By blocking Cx43 channels or interfering with GJ communication between astrocytes and carcinoma cells, it may be possible to reduce metastatic colonization in the brain (Chen et al., 2016). This emerging understanding of Cx43 and its role in facilitating metastasis highlights the importance of targeting GJ

communication in oncology. Focusing on disrupting interactions between carcinoma cells and their benign surroundings, such as astrocytes, could lead to the development of more effective therapies to prevent or limit brain metastasis. It has been noted that GJs can buffer the escalation of critical intracellular substance concentrations, thus reducing cytotoxicity from radiotherapy or chemotherapy toward tumor cells. Consequently, targeting these networks has emerged as a promising strategy to enhance therapeutic efficacy. Disrupting tumor networks formed by Cx43-based GJs has gained attention as a novel therapeutic approach.

1.2. GJ inhibitors as a therapeutic approach

This approach has spurred significant interest in developing inhibitors that specifically target GJ-mediated communication, with the aim of counteracting tumor progression and therapy resistance. Over the past 20 years, GJ inhibitors have been extensively studied across various fields, including oncology, cardiology, and neurology. Among them, carbenoxolone (CBX) is a widely recognized GJ inhibitor, extensively used in experimental research since the 1980s for its ability to inhibit intercellular communication (Davidson et al., 1986; Leshchenko et al., 2006; Manjarrez-Marmolejo and Franco-Perez, 2016). However, its translational potential is limited due to challenges such as its inability to effectively cross the blood-brain barrier (B.B.B.) (Leshchenko et al., 2006). In contrast, meclofenamic acid (MFA) and tonabersat (TO) have emerged as some of the most widely studied GJ inhibitors, offering distinct advantages for clinical and translational research. Their unique properties make them particularly promising for exploring the therapeutic potential of targeting GJ communication in aggressive tumors like medulloblastoma (MB) (**Figure 4**).

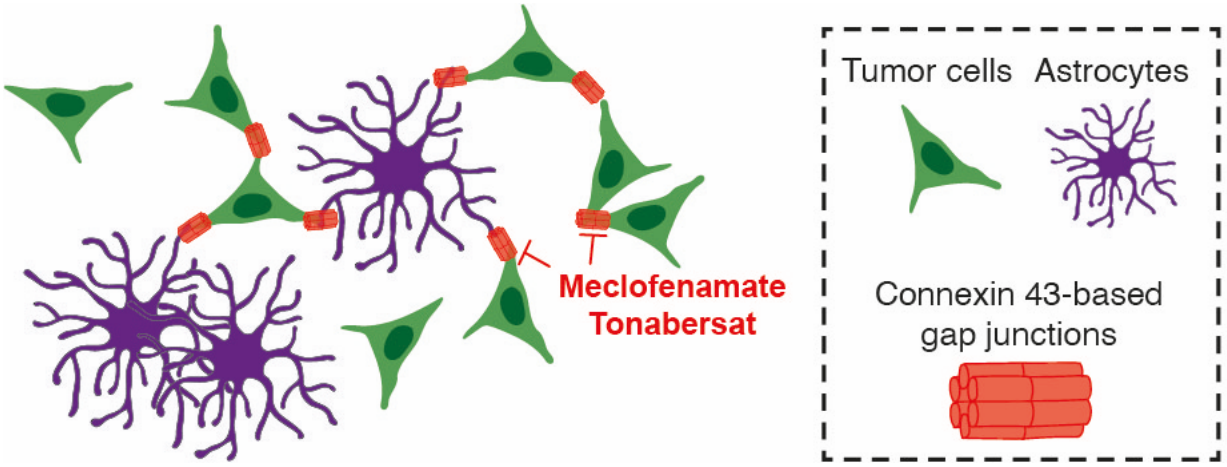

Figure 4. The function of GJ inhibitors, MFA and TO. The scheme illustrates that MFA and TO can functionally block Cx43-GJs between tumor cells and adjacent cells, such as astrocytes.

MFA is a derivative of N-phenylanthranilic acid and is also one of the commonly used FDA-approved nonsteroidal anti-inflammatory drugs (NSAIDs) in clinical practice. Originally, MFA was intended to relieve chronic pain and inflammation, such as in rheumatoid arthritis, by inhibiting COX-1 and COX-2, thereby interrupting the biosynthesis of prostaglandins from arachidonic acid (Ning et al., 2013; Schneider et al., 2021a). With increasing evidence, MFA was found to not only inhibit inflammation but also block ion channels in human retinal pigment epithelial cells and disrupt electrical synapses in the rat retina (Ning et al., 2013; Veruki and Hartveit, 2009). In the study of Veruki et al., MFA demonstrated even at high concentration, still exhibit many desirable properties: strong efficacy, water solubility, and relatively rapid reversibility (Veruki and Hartveit, 2009). Those characteristics suggest that MFA is an appropriate GJ antagonist. Although there is no strong evidence showing that MFA specifically targets Cx, it has been observed to profoundly block Cx43-mediated intercellular communication in various cell types, from rat kidney fibroblasts to human retinal pigment epithelial cells (Hauge et al., 2009; Ning et al., 2013). Furthermore, MFA has previously been reported to inhibit GJ-mediated

communication and cellular tethering in glioblastoma cells (Schneider et al., 2021a; Schneider et al., 2021b). MFA interrupted of Cx43-based tumor microtubes (TM) from functional and morphological perspectives. The decreased length of TMs led to the disconnection of the network which can reduce the cytotoxic effect, thereby making glioblastoma cells profoundly vulnerable to chemotherapeutic agents (Schneider et al., 2021a; Schneider et al., 2021b). Additionally, MFA-mediated Cx43 inhibition yielded a reduction of functional GJ coupling between human breast cancer cells and astrocytes resulting in a prevention of brain metastasis formation (Chen et al., 2016). Few studies have suggested that MFA or NSAIDs enable to cross B.B.B. in murine epilepsy models (Bannwarth et al., 1989; Sinkkonen et al., 2003; Wallenstein and Mauss, 1984). However, to date, the realistic evaluation of MFA levels in the human brain is lacking (Schneider et al., 2021a; Schneider et al., 2021b). A german-wide clinical trial (MecMeth/NOA-24 trial, EudraCT2021-000708-39) will first time measure the concentration of MFA in relapsed glioblastoma tissue and uncover this mystery.

TO, the second GJ antagonist, is a novel benzoylamino benzopyran compound that has been used to inhibit cortical spreading depression and neurogenic inflammation (Silberstein, 2009). Moreover, TO exhibits a high affinity for a stereospecific binding site, which is associated with GJs in neuronal, glial, and astrocyte cells (Silberstein, 2009; Zoteva et al., 2024). Previous studies support that TO can interrupt the connection between neurons and satellite glial cells of the trigeminal ganglion. As a result, TO may effectively abolish pain transmission from trigeminal neurons (Damodaram et al., 2009; Silberstein, 2009). Therefore, TO has been extensively studied for its potential to reduce the frequency and severity of migraine attacks and is also being investigated as a candidate for epilepsy treatment in clinical trials. It is known to effectively pass through the B.B.B. (Durham and Garrett, 2009; Hauge et al., 2009). Moreover, TO can inhibit GJs

between neurons and glial cells, which is relevant for treating migraines. Given that Cx43 shows predominant expression in the central nervous system (CNS), this suggests that TO could be a promising inhibitor of Cx43-based GJs (Zoteva et al., 2024).

MFA and TO are promising GJ inhibitors known to disrupt Cx43-mediated communication, with demonstrated potential in various cancer types and neurological conditions. However, their application to more aggressive tumors like MB remains largely unexplored. MB is a highly aggressive childhood brain tumor, and the role of Cx43 in its tumor networks has yet to be thoroughly investigated. Given the distinct cellular morphology of glioblastoma and MB cells, it is uncertain whether similar tumor networks exist in MB or if they could be effectively disrupted pharmacologically. This uncertainty underscores the need for further exploration of the therapeutic potential of targeting Cx43 in this context.

1.3. Medulloblastoma (MB)

1.3.1. MB: overview, epidemiology, and etiology

MB is the most prevalent malignant pediatric brain tumor, comprising over 20% of childhood cerebral neoplasms and accounting for approximately 20% of all intracranial tumors in children and 40% of all pediatric posterior fossa (PF) tumors (**Figure 5.**) (Choi, 2023; Rossi et al., 2008; Sun et al., 2012). It is classified as an embryonal neuroepithelial tumor, with three-quarters of cases arising from the cerebellum and the fourth cerebral ventricle. The incidence of MB is 0.41 cases per 100,000 individuals, with a peak occurrence between the ages of 5 and 7 years, although about 30% of cases occur in adults. MB is more common in males, with a male-to-female ratio of 1.7:1, although this ratio varies across different subgroups of MB (Choi, 2023). Epidemiological data, including from the SEER Program, show a higher incidence of MB in white children compared to

black children, particularly in those older than 4 years of age (Geris and Spector, 2020; Khanna et al., 2017).

The prognosis for MB varies widely, with five-year survival rates ranging from 50% to 90%. Prognostic factors include the patient's age, molecular characteristics, and the amount of residual tumor following surgery. While the exact etiology of MB remains unknown, studies suggest a potential link to risk factors such as maternal diet, childhood viral infections (e.g., human neurotropic JC virus and cytomegalovirus) (Baryawno et al., 2011; Bunin et al., 2005; Krynska et al., 1999), and inherited cancer predisposition syndromes (e.g., Li-Fraumeni syndrome, Gorlin syndrome, familial adenomatous polyposis) (Waszak et al., 2018). However, routine genetic screening is necessary to confirm these associations.

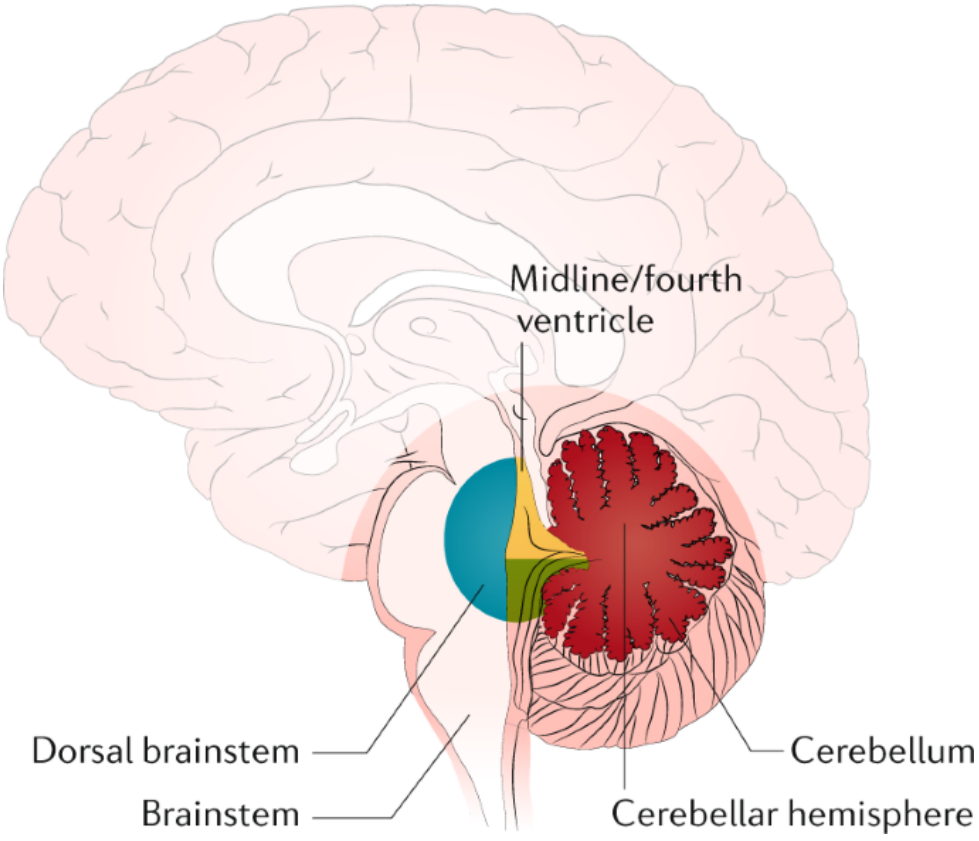

Figure 5. The location and origin of MB. MB is a neuroectodermal tumor that originates in the cerebellum or in the roof of the fourth ventricle (modified from (Northcott et al., 2019)).

1.3.2. Classification of MB

1.3.2.1. WHO Classification: Embryonal tumors group

According to the 5th edition of the WHO Classification of Tumors of the Central Nervous System, published in 2021 (WHO CNS5), embryonal tumors are categorized into two groups: MB and other CNS embryonal tumors, the later including atypical teratoid/rhabdoid tumor (ATRT) (Louis et al., 2021). This classification is based on advanced molecular diagnostics, as well as established developments in histology and immunohistochemistry for tumor characterization (Louis et al., 2021).

1.3.2.2. Molecular and histological classification

MB is the most common type of embryonal tumors which is classified as CNS WHO grade 4. In the WHO CNS5 classification, MB can be categorized according to molecularly defined or histological defined (Louis et al., 2021). Molecularly defined MB can be further divided into four principal molecular groups: WNT-activated, SHH-activated with *TP53*-wildtype, SHH-activated with *TP53*-mutant, and non-WNT/non-SHH (including former group 3 and group 4 tumors) (**Figure 6** and **Table 2**). Each molecular group has specific origins and precursor cells is distinguished based on their distinct types of somatic mutations, copy number alterations, transcriptional profiles, and clinical prognoses (Fang et al., 2022; Kurdi et al., 2023; Menyhart and Gyorffy, 2019). Furthermore, using array-based DNA methylation and transcriptome profiling, SHH-activated MB can be further subdivided into 4 subtypes, SHH-1, SHH-2, SHH-3, and SHH-4 (corresponding to α, β, γ and δ, in Cavalli et al. Figure 6B), while non-WNT/non-SHH MB can be refined into 8 subtypes, as shown in **Table 2** (Cavalli et al., 2017; Kumar et al., 2020; Louis et al., 2021; Ray et al., 2021).

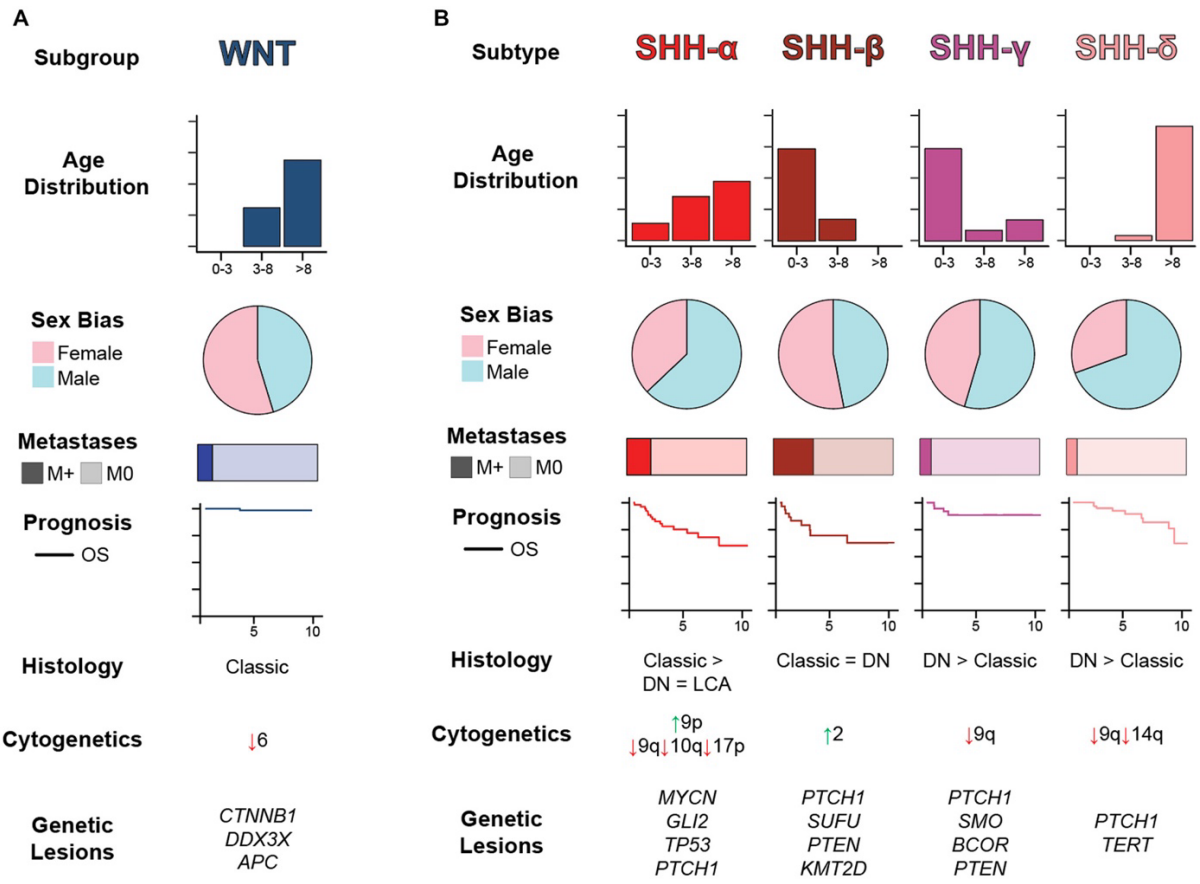

Figure 6. **The main features and characteristics of the WNT and SHH subgroups of MB are summarized.** The clinical characteristics of **(A)** WNT and **(B)** SHH are highlighted. According to the WHO CNS5 classification, SHH-activated MB can be further divided into four clinically and cytogenetically distinct subtypes based on *TP53* status, designated as SHH-α, -β, -γ, and -δ (corresponding to subtypes 1, 2, 3, and 4), with *TP53*-mutant and *TP53*-wildtype tumors exhibiting distinct clinicopathological features. (modified from (Cavalli et al., 2017; Kumar et al., 2020)).

Before WHO CNS5 released, there were four morphological types in the histopathological category: classic, large cell/anaplastic (LCA), desmoplastic/nodular (DN), and MB with extensive nodularity (MBEN). Starting with WHO CNS4 (2016), an accurate diagnosis of MB must consider both histopathological features and either molecular or genetic patterns (Franceschi et al., 2019). For example, nearly all WNT-activated tumors exhibit a classic pattern (**Figure 6A**) as most of non-WNT/non-SHH MBs (**Table 1**). The SHH-activated molecular group typically presents with DN morphology or MBEN, while the LCA type

aligns with the subtype II of non-WNT/non-SHH (Franceschi et al., 2019; Louis et al., 2021). These types are now combined into single category in the revised WHO CNS5 as MB, histologically defined (Louis et al., 2021). Given the heterogeneity of MBs, an integrated diagnosis is necessary to provide a clear definition and precise classification for subsequent risk stratification (**Table 1**).

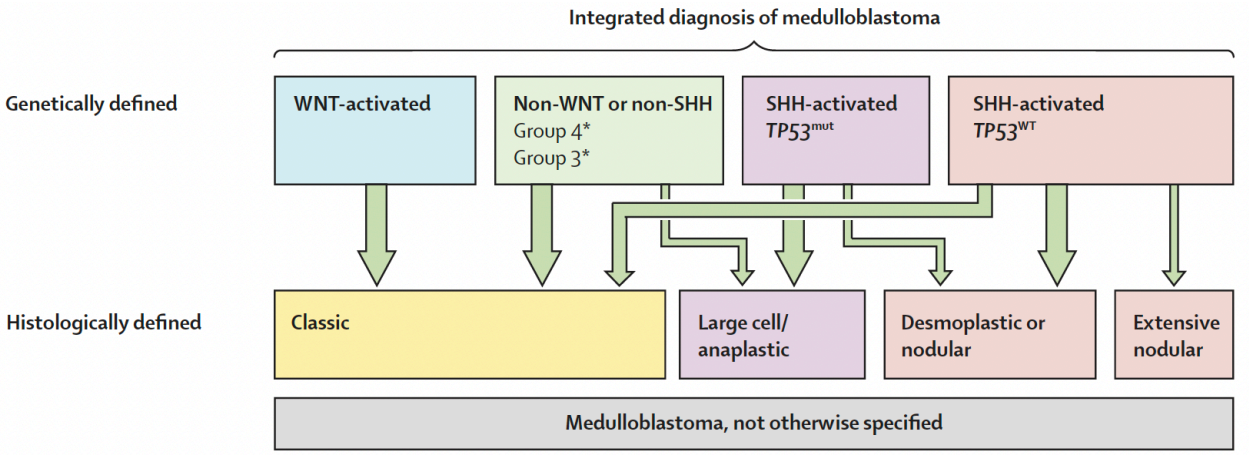

Table 1. Integrated diagnosis of MB. The overview of the correlation of genetically defined and histological defined MBs. Individual molecular group has specific association to certain morphological features (modified from (Louis et al., 2021)).

1.3.2.2.1. WNT-activated MB

WNT-activated MB arises from lower rhombic lip progenitors and is characterized by the activation of the WNT signaling pathway (Franceschi et al., 2019). WNT-activated MB accounts for the smallest portion of MB cases, representing 10% (Kumar et al., 2020). It is almost absent in infants (1%) and has an equal male-to-female ratio of 1:1, as shown in **Figure 6A**. WNT tumors have a favorable prognosis, with a 90% long-term survival rate (Clifford et al., 2006; Kool et al., 2012; Sharma et al., 2019; Taylor et al., 2012). Almost all WNT-activated MB display classic morphology. It commonly contains somatic mutations

in exon 3 of the *CTNNB1* gene (catenin β-1, also known as β-catenin) as well as monosomy of chromosome 6 (Clifford et al., 2006; Ramaswamy et al., 2016). Moreover, mutations in exon 3 of *CTNNB1* lead to the cytoplasmic accumulation of β-catenin, which then translocate to the nucleus. This process can be observed through nuclear immunohistochemical staining for β-catenin (Taylor et al., 2012). However, a gold standard diagnosis for WNT-activated MB has not yet been established. Even with a definitive WNT transcriptome profile, cases have been reported that do not present monosomy of chromosome 6 (Northcott et al., 2011). Therefore, further investigation to characterize WNT-activated WB is still required. Besides, given the high survival rate, it is a noteworthy topic to gain insight into the underlying molecular mechanisms to avoid overtreatment of patients (Taylor et al., 2012).

1.3.2.2.2. SHH-activated MB

Similar to WNT-activated MB, SHH-activated tumor exhibits abnormal activation of the SHH signaling pathway (Funakoshi et al., 2023; Menyhart and Gyorffy, 2019). It has been reported that SHH-activated MBs develop from cerebellar granule neuron progenitors. These tumors account for approximately 30% of all MB cases and have the highest incidence of germline mutations (Franceschi et al., 2019; Funakoshi et al., 2023). DN and MBEN histological patterns are specifically associated with the SHH-activated group, with the former being more common but the latter generally having a better prognosis (Cotter and Hawkins, 2022; Ray et al., 2021). Based on the status of *TP53* gene (tumor protein), SHH tumor can be further categorized as SHH-activated *TP53*-wildtype and SHH-activated *TP53*-mutant subgroups (Menyhart and Gyorffy, 2019). SHH-activated *TP53*-wildtype tumors are more commonly found in adults and young children, and they have a favorable prognosis, with an approximately 81% five-year overall survival (OS) rate

(Menyhart and Gyorffy, 2019). SHH-activated tumors with *TP53* mutation represent 21% of all SHH-activated MB cases and have a five-year OS of about 41% (Menyhart and Gyorffy, 2019). Contrast to the bimodal age distribution of SHH-activated *TP53*-wildtype, most of *TP53*-mutant SHH commonly present in between ages 5 children and ages 18 teenagers (Cotter and Hawkins, 2022; Funakoshi et al., 2023; Menyhart and Gyorffy, 2019). Except for *TP53*, *PTCH1* and *SUFU* mutations are often found in one-fifth of all SHH-activated MB cases in infants (Menyhart and Gyorffy, 2019). Those mutations are linked to genetic predispositions. For instance, Gorlin syndrome is connected with the aberrations in the *PTCH1* and *SUFU* genes, whereas Li-Fraumeni syndrome is associated with *TP53*-mutation (Cotter and Hawkins, 2022; Menyhart and Gyorffy, 2019; Smith et al., 2014). The predisposing genetic carriers can lead to multiple families' cancers, including the development of MB. Furthermore, based on clinical prognosis, the most affected population, *TP53* status, and different patterns of genetic alteration, SHH-activated group can be further categorized into four subtypes according to WHO CNS5: SHH-1 (29% of all SHH-MBs), SHH-2 (16%), SHH-3 (21%), and SHH-4 (34%) (**Figure 6B**) (Louis et al., 2021; Ray et al., 2021). Certain gene mutations typically correspond to specific subtypes. For instance, SHH-1 commonly demonstrates gene alterations in *TP53 and ELP1* while *SMO* and *SUFU* mutations are typically found in SHH-4 and SHH-1/-2, respectively (Funakoshi et al., 2023; Suzuki et al., 2019; Waszak et al., 2020). Collectively, these molecular stratifications reveal valuable targets and provide potential opportunities for clinical therapies in SHH-activated MB.

1.3.2.2.3. Non-WNT/non-SHH-activated MB

Non-WNT/non-SHH MBs constitute the majority of MBs, accounting for approximately 60% of all cases. These tumors likely arise from neural progenitor cells and are associated

with the worst outcomes (Franceschi et al., 2019; Northcott et al., 2014). In the WHO CNS5 classification, groups 3 and 4 are combined into this category, with the majority of cases belonging to group 4 (Louis et al., 2021; Ray et al., 2021). Particularly, group 3 has a comparatively worse prognosis, with a 5-year OS rate of less than 45% and a 39% incidence of metastasis, which is the highest tendency for dissemination among all MBs (Cavalli et al., 2017; Choi, 2023; Kool et al., 2012; Marquardt et al., 2023; Millard and De Braganca, 2016). Group 4 has intermediated survival rate and the second highest frequency of metastasis at 31% (Cavalli et al., 2017; Kool et al., 2012). Among non-WNT/non-SHH MBs, males are twice as often to be affected as females (Kool et al., 2012). Due to the epidemiology, histopathological differences, prognosis, and genetic alterations, it can be further subclassified into 8 subtypes as shown in **Table 2** (Mynarek et al., 2023; Sharma et al., 2019). Subtype II to IV solely belong to group 3 while subtype I and V to VIII mainly or exclusively under group 4 (Mynarek et al., 2023; Northcott et al., 2017; Sharma et al., 2019; Wu et al., 2022). Moreover, subtype I is least common whereas subtype VIII is the most frequent and exclusive in group 4 (Northcott et al., 2017; Northcott et al., 2014; Sharma et al., 2019). Notably, subtypes II and III have the poorest 5-year OS rate, as reported in the HIT2000 and I-HIT-MED cohorts (Mynarek et al., 2023; Sharma et al., 2019). Meanwhile, subgroups VI, VII, and VIII demonstrated a more favorable 5-year progression-free survival rate, from 65% to 76% (Sharma et al., 2019). From copy-number variants (CNVs) derived from the DNA-methylation array data set reveal a high correlation between specific genetic events and certain subtypes (**Table 2**). For example, subgroups II and III primarily display *MYC* amplification which is a hallmark of group 3 MBs, accompanying upregulation of *GFI1* proto-oncogene. It has been demonstrated that the combination of overexpressed *MYC and* activated *GFI1* could lead to tumor growth (Ghasemi et al., 2022; Northcott et al., 2014). Unlike *MYC*, the amplification of *MYCN* is

enriched in subgroups V and VI (Ghasemi et al., 2022; Mynarek et al., 2023; Northcott et al., 2017; Ray et al., 2021; Sharma et al., 2019). From the perspective of whole-chromosomal aberrations (WCA), subgroups IV, VI, and VII are characterized by two or more signatures, including gains of chromosome 7 or losses of chromosomes 8 or 11. These chromosomal aberrations are identified as markers of low risk in the HIT-SIOP PNET4 cohort (Ghasemi et al., 2022; Goschzik et al., 2018; Mynarek et al., 2023). Furthermore, isochromosome 17q (i17q) as a molecular feature in non-WNT/non-SHH MBs, especially in subgroup VIII (Ray et al., 2021; Sharma et al., 2019).

The subdivision of non-WNT/non-SHH MBs not only reveals the dynamics of MB development but also provides insights into risk stratification, potential therapeutic approaches, and prognosis in clinical setting.

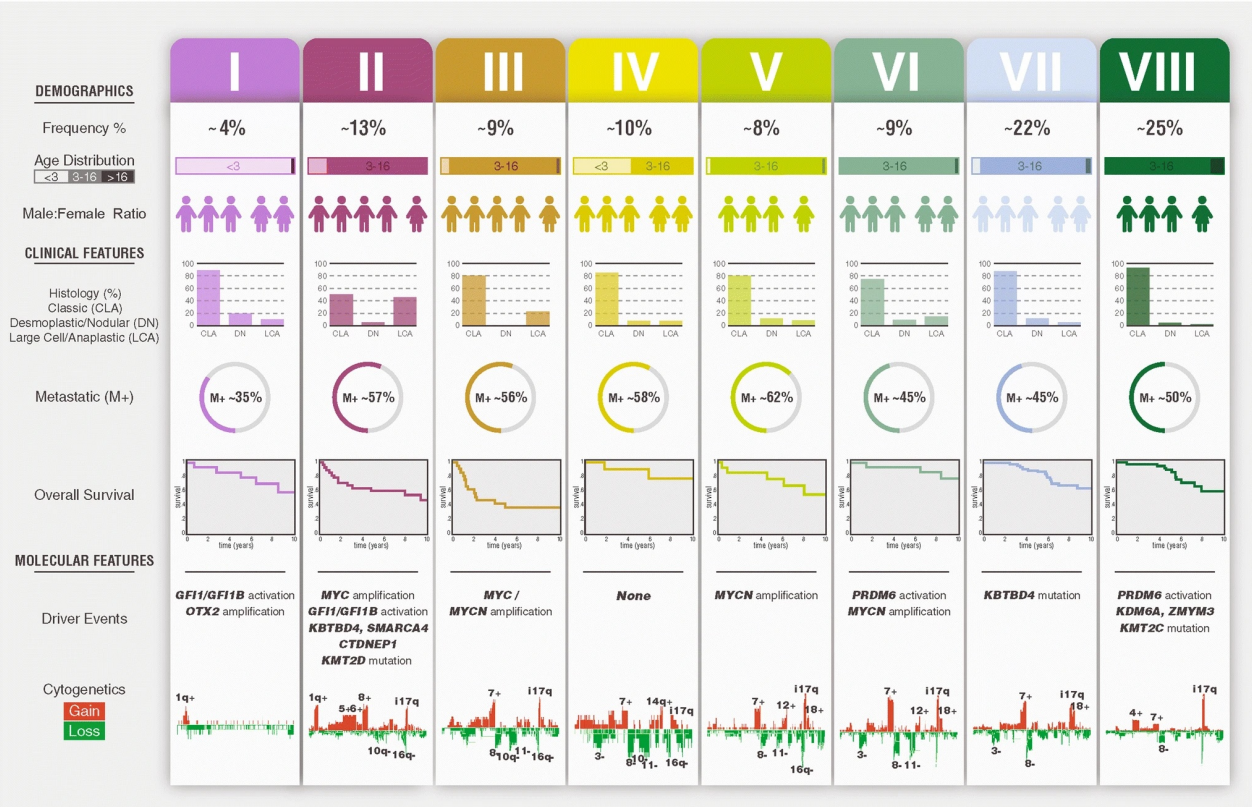

Table 2. Overview of eight non-WNT/non-SHH MB subtypes (WHO CNS5 Classification). A comparison of each subtype is made based on epidemiology,

histological morphology, prognosis, and molecular features (modified from (Sharma et al., 2019)).

1.3.3. Clinical features of MB

1.3.3.1. Symptomatology and diagnostics

MB is well-known for its rapid growth rate, with patients often displaying symptoms within weeks to months. Since MBs are usually located in the cerebellum, patients often exhibit difficulties with balance control and coordination, as well as increased intracranial pressure. The most common manifestations are vomiting, morning headaches, psychomotor regression, and lethargy (Brasme et al., 2012; Millard and De Braganca, 2016).

In clinic, radiographic differential diagnosis is a vital step to differentiate MB in PF lesion with ependymoma, ATRT and pilocytic astrocytoma, and metastasis (Eran et al., 2010; Millard and De Braganca, 2016). MBs display unique imaging features on both computed tomography (CT) and magnetic resonance imaging (MRI) (Millard and De Braganca, 2016). On CT, MBs frequently appear as hyperdense masses with distinct contrast enhancement. The images often show accompanying cysts or necrosis, and calcification can be observed in 10-20% of MB cases. On MRI, MBs appear hypointense compared to gray matter on T1-weighted imaging. Additionally, 90% of patients exhibit increased heterogeneity with gadolinium enhancement (Millard and De Braganca, 2016).

1.3.3.2. Therapeutic approach, side effects, and ongoing trials

After initial staging with MRI of the brain and spine, cerebrospinal fluid analysis, and classification, the standard therapy for resectable MB includes maximal safe surgical resection, followed by the Packer chemotherapy regimen (vincristine, lomustine

(Chlorethyl-Cyclohexyl-Nitroso-Urea, CCNU), and cisplatin) and craniospinal irradiation (CSI) for patients older than 3 years (Franceschi et al., 2019; Kocakaya et al., 2016; Ning et al., 2015; Rutkowski et al., 2010; Young et al., 2023). Conventionally, surgery tumor excise is still the first step. However, excess remaining tumor tissue has been shown significantly with the worse outcomes (Michalski et al., 2021; Young et al., 2023). Therefore, neurosurgeons excise feasibly as much of tumor (nearly gross total resection) without causing new neurological impairments. Adult patients should receive systemic chemotherapy besides resection and radio therapy. However, the chemo-regimen still remains being adjusted since is mainly based on pediatric trails. It also needs to consider the time of diagnosis and the status of patients (Franceschi et al., 2019; Juraschka and Taylor, 2019; Kocakaya et al., 2016; Rajagopal et al., 2017).

Since MB tumors can attach to some critical CNS tissues like brainstem, aggressive resection may still cause irreversible neurological complications (Kocakaya et al., 2016; Thompson et al., 2016). The patients usually exhibit cerebellar mutism syndrome with speech deficits, labile emotion, and ataxia, sometimes accompanying brainstem dysfunction like dysphagia and facial or abducent nerve impairments (Juraschka and Taylor, 2019; Robertson et al., 2006; Thompson et al., 2016). Moreover, after CSI and multiagent chemotherapy, younger children often develop neurocognitive impairment, hearing loss, pituitary hormone deficiency, and cerebrovascular disease (Franceschi et al., 2019; Juraschka and Taylor, 2019). For adolescents and adults, delayed hematological toxicity and neurotoxicity is a key issue should be followed up (Franceschi et al., 2019). Furthermore, in a nearly thirty-year cohort of the Childhood Cancer Survivor Study, despite an extended lifespan, MB survivors face a diminished quality of life due to disabling chronic health conditions (such as cognitive sequelae and subsequent neoplasms) and mental health issues (Salloum et al., 2019). Particularly among adult

survivors, nearly 45% require psychosocial intervention to monitor and address anxiety and depression (Franceschi et al., 2019).

With the aim of improving the quality of life for MB patients, more effective and less invasive alternative therapies are being investigated. The molecular classification of MB has promoted the development of personalized medicine, which is tailored to specific markers or molecular pathways. For WNT-activated MBs, the goal is to avoid overtreatment, potentially even without radiotherapy, while maintaining good survival outcomes. In a trial (NCT01857453), de-escalated treatment for intermediate-risk patients involves dose-reduced radiotherapy combined with chemotherapy. Additionally, tomotherapy and proton therapy are being considered as alternatives to radiotherapy (Franceschi et al., 2019). Concerning SHH-MBs, antagonists of the smoothened (SMO) receptor, such as vismodegib (GDC-0449) and sonidegib, have increased patients' progression-free survival (Bautista et al., 2017; Juraschka and Taylor, 2019; LoRusso et al., 2011). Moreover, the CK2 inhibitor CX-4945 is currently being evaluated for its potential benefits in treating recurrent SHH MBs (NCT03904862) (Purzner et al., 2018). Regarding non-WNT/non-SHH MBs, which have the worst clinical outcomes, various preclinical trials are developed to aim at mutant markers. For instance, a combination of the inhibitors of PI3K pathway inhibitors (Buparlisib) and histone deacetylase (Panobinostat) or BET-bromodomain (JQ1), is used to target MYC expression. Additionally, the downregulation of GFI1/GFI1B overexpression can be achieved through the use of LSD1 inhibitors (GSK-LSD1 and OBV-1001) (Bandopadhayay et al., 2014; Juraschka and Taylor, 2019; Lee et al., 2019; Pei et al., 2016). Altogether, these trials drive the treatment of MBs toward more effective, precise, and safer approaches.

Nevertheless, the immunotherapeutic approach has several limitations. For instance, it relies on the patient's immune system to recognize and destroy tumor cells (Guido et al.,

2022). These restrictions emphasize an urgent clinical demand for being implemented in prospective clinical studies. Furthermore, the ability to cross the B.B.B. remains a significant challenge.

1.3.4. Prognosis factors in MB

The prognosis dependents on MB patient's age, group type, tumor infiltration stage, mutation of genes, postoperative residual tumor size, pathological morphology, and extent of metastasis (Franceschi et al., 2019). Depending on these factors, patients can be stratified into low, intermediate, and high-risk groups (**Table 3**). It is noteworthy that the outcomes differ from adults, infants, and children, even within the same category. Overall, for intermediated risk group older than 3 years old, the long-term survival rate can reach 70-80% (Aref and Croul, 2013). Lower life expectancy between 6 months and less 10% of 2-year survival is observed in high-risk group. This includes patients younger than 3 years old, those with a residual tumor larger than 1.5 cm^2, and/or those with metastasis (Franceschi et al., 2019). Generally, adults with the histological diagnosis of large cell/anaplastic are consider as a high-risk population (Brown et al., 2000; Franceschi et al., 2019). Non-WNT/non-SHH MBs in adult patients have worse outcomes than children. SHH-activated MBs with *TP53* mutant serve an unfavorable outcome compared to those with *TP53* wildtype (Franceschi et al., 2019). To date, prognostic evaluations are based on pediatric trails and are not firmly unconfirmed in adults. Prospective validation for adult patients will be essential in future trials.

Even if MB patients can survive after aggressive treatments, it is vital to not only to address long-lasting complications but also the high risk of relapse (Slika et al., 2024). Furthermore, multiple studies have noticed that recurrent tumors have significantly diverse cellular genetic profiles compared to the original tumors, even without switching subgroups (Chen

et al., 2023; Morrissy et al., 2016; Slika et al., 2024). Although the reason for relapse has not yet been determined, it is assumed that recurrent tumors undergo clonal selection after conventional therapeutic approaches. As a consequence, the original genomics therapy loses their target and become less effective. Additionally, chemoresistance may arise from the interaction between tumors and the TME through intertumoral communication of tumor network (Osswald et al., 2015; van Bree and Wilhelm, 2022; White et al., 2024).

<table>
<tr><th>Risk Category</th><th>Low Risk</th><th>Standard Risk</th><th>High Risk</th><th>Very High Risk</th></tr>
<tr><td>Survival (%)</td><td>>90</td><td>75-90</td><td>50-75</td><td><50</td></tr>
<tr><td rowspan="3">Subgroup, clinical and molecular characteristics</td><td rowspan="2">Non-metastatic</td><td>Non-metastatic, TP53 WT and no MYCN amplification</td><td rowspan="2">One or both:
• Metastatic
• MYCN amplification</td><td rowspan="2">TP53 Mutation</td></tr>
<tr><td rowspan="2">Non-metastatic and no MYC amplification</td></tr>
<tr><td>Non-metastatic and Chromosome 11 loss</td><td>Non-metastatic and no chromosome 11 loss</td><td>Metastatic</td><td>Metastatic</td></tr>
</table>

Table 3. Suggested risk classification for non-infant MB. This proposed risk stratification is based on clinical and molecular criteria. The classification system groups MB into subtypes: WNT (blue), SHH (red), group 3 (yellow), and group 4 (green). Each subgroup's characteristics, including clinical features and molecular markers, are reflected in the boxes (modified from (Juraschka and Taylor, 2019; Ramaswamy et al., 2016)).

1.3.5. Tumor networks in MB

Even if MB patients can survive after aggressive treatments, it is vital to not only to address long-lasting complications but also the high risk of relapse (Slika et al., 2024). Although the mechanisms underlying relapse remain unclear, it is thought that recurrent tumors undergo clonal selection after conventional therapies, causing genomic therapies to lose their targets and become less effective. Additionally, chemoresistance may develop through interactions between tumors and the TME, facilitated by intertumoral

communication within tumor networks (Osswald et al., 2015; van Bree and Wilhelm, 2022; White et al., 2024).

Tumor networks have been extensively studied in various cancer types, but research on MB, particularly those involving Cx43-based GJs, remains limited. Cx43 GJs have been recognized for their ability to enhance therapeutic effects in MBs by transmitting cytotoxic compounds from transduced cells to adjacent non-transduced cells, a process known as the bystander effect (BE) (Li et al., 2011). Sun et al. demonstrated that increasing Cx43 expression in Daoy MB cells enhanced cytotoxicity through the BE in the herpes simplex virus thymidine kinase/ganciclovir (HSVtk/GCV) system (Sun et al., 2012). Supporting this, Li et al. observed significant tumoricidal effects both in vitro and in vivo after upregulating Cx43 expression in Daoy MB cells (Li et al., 2011). These findings confirmed a positive correlation between Cx43 levels and the BE while highlighting the potential for Cx43-targeted therapies in MB. However, the HSVtk/GCV suicide system failed to show a significant impact on tumor progression or survival in a clinical trial, likely due to limited vector dissemination in phase III (Rainov, 2000). Collectively, these studies underscore the therapeutic promise of GJs, positioning Cx43 as a compelling target for MB treatment strategies.

1.4. Aim

This study investigates whether MB cells, particularly those from the non-WNT/non-SHH group, are organized into a cellular network and explores the potential role of Cx43-based GJs in maintaining this connectivity. To achieve this, we will first pharmacologically target intercellular GJs and assess their impact on the morphological connectivity of tumor cells, as well as key cellular processes such as proliferation and cell death. MFA and TO were selected for their proven GJ-inhibiting properties. Additionally, MFA is an FDA-approved

drug, and TO has the ability to cross the B.B.B., making them suitable candidates for this study. In the next phase, we will evaluate whether this potential cell-isolating effect could enhance the efficacy of chemotherapeutic agents commonly used in clinical settings. Through 3'-mRNA sequencing, we aim to identify critical cell signaling pathways associated with this pharmacological approach. Finally, we will employ a Cx43-knockout (KO) model to validate whether the effects observed with pharmacological GJ inhibition are specifically attributable to the inhibition of Cx43.

A key focus of this project is to determine whether MB cells form tumor networks and to understand the role of Cx43-based GJs within these networks. Additionally, the study evaluates whether disrupting these connections through pharmacological inhibition or genetic KO can weaken tumor interactions and enhance the efficacy of chemotherapeutic agents. This approach holds the potential to pave the way for innovative therapeutic strategies against MB.

2. Materials and Methods

2.1. Materials

2.1.1. MB primary human cell lines

MEB-MED8A (Med8A) and D283Med (D283) cell lines were kindly provided by Prof. Dr. Torsten Pietsch (Department of Neuropathology, University of Bonn Medical Center, Bonn, Germany). The Cx43 KO clone of Med8A was generously generated in PD Dr. Mike-Andrew Westhoff's lab (Department of Pediatrics and Adolescent Medicine, Ulm University Medical Center, Ulm, Germany), as previously described (Tews et al., 2019). All cells used in this study were adherent.

2.1.2. Chemicals and reagents

2.1.2.1. Culture medium for MB cells

Table 4. List of culture medium components for MB cells

MB culture medium		
Product	**Manufacture**	**Concentration**
Dulbecco's Modified Eagle Medium	Gibco™ (11965092)	
Fetal bovine serum (FBS)	Gibco™ (10270106)	10%
L-glutamine	Gibco™ (A2916801)	4 mM
Penicillin/streptomycin	Gibco™ (15140122)	1%
Puromycin (only for maintenance of Cx43 KO clone)	Gibco™ (A11138-03)	1 µg/mL
Sodium pyruvate	Gibco™ (11360070)	1 mM

2.1.2.2. Pharmaceutical compounds

Table 5. List of pharmaceutical compounds and dissolution

Drug			
Product	**Manufacture**	**Stock Concentration**	**Solvent**
Lomustine (CCNU)	Merk (L5918)	100 mM	Ethanol
MFA	Sigma (M4531-5G)	100 mM	Ampuwa water
TO	Sigma (SML1354-5mg)	50 mM	Dimethyl sulfoxide (DMSO)

2.1.2.3. Laboratory consumables

Table 6. List of laboratory consumables

Laboratory consumables	
Product	**Manufacture**
10 mL serological pipette	Sarstedt (861254001)
1000 µL tip	Sarstedt (70.3050)
15 mL falcon	Thermo Fisher Scientific (339650)
200 µL tip	Sarstedt (70.3030)
24-well standard culture plate	Sarstedt (833922)
25 mL serological pipette	Sarstedt (861685001)
5 mL serological pipette	Sarstedt (861253001)
50 mL falcon	Thermo Fisher Scientific (339652)
6-well standard culture plate	Sarstedt (833920)
75 cm^2 cell culture flask (T75)	Sarstedt (833911002)
96-well standard culture plate	Sarstedt (833924005)

Absolute ethanol	AppliChem GmbH (11234904)
Ampuwa® water	Apotheke (30200555)
Combi tips advanced 5mL	Eppendorf (30089456)
DMSO	AppliChem GmbH (67-68-5)
Dulbecco's Balanced Salt Solution (DPBS)	Gibco™ (14190169)
Eppendorf® Combitips Advanced® 5 mL	Eppendorf (30089456)
Eppendorf® Microtube 1.5 mL	MerK (EP0030125150)
Eppendorf® Safe-Lock micro test tubes 2 mL	MerK (EP0030123344)
Filter 10 µL tip	Starlab (S1121-3810)
Filter 1000 µL tip	Sarstedt (703050275)
Peha-soft nitrile gloves, powder-free (S)	Hartmann
TrypLE	Gibco™ (12604013)

2.1.3. Equipments

Table 7. List of instruments and devices

Equipments	
Product	**Manufacture**
µQuant microplate spectrophotometer	Biotek Instruments
Cell counter chamber	Glaswarenfabrik Karl Hecht GmbH & Co KG
Cell culture CO^2 incubator	Heraeus
Centrifuge 5415 R	Eppendorf
Centrifuge 5810 R	Eppendorf
Grant Y22 Thermostatic water bath	Grant

Lionheart FX Automated Microscope	Agilent
Magnetic stirrer	Heidolph ((MR 3001))
Odyssey® DLx	LI-COR Biosciences
S20 SevenEasy™ pH meter	METTLER TOLEDO
Safety Cabinet	Heraeus
VisiScope CSU-W1 with VS-Homogenizer Spinning Disk	Nikon (VisiScope CSU-W1)
Vortex mixer	IKA-Werke

2.1.4. Softwares

Table 8. List of softwares

Software	
Product	**Manufacture**
Microsoft Excel	Microsoft
Image J	National Institutes of Health, Bethesda, USA
FlowJo V10.4	FlowJo LLC, Oregon, USA
GraphPad PRISM V9.5.1	GraphPad Software, San Diego, USA
Adobe Illustrator 2023 V27.7	Adobe, San Jose, USA
R V4.3.0	
Gen5 software	Agilend
CLx Infrared Imaging System version 6.0	LI-COR

2.1.5. Specific reagents and consumables for experiments

2.1.5.1. Immunofluorescence (IF) staining

Table 9. List of chemicals, antibodies, and materials for IF staining

IF staining		
Product	**Manufacture**	**Concentration**
Round glass coverslips (12mm)	Carl Roth (P231.1)	
16% paraformaldehyde	Polysciences, Inc. (18976)	1:4 in culture medium to have 4% dilution
Triton X-100	Sigma (T8787)	10 µL in 10mL DPBS to have 0.1% dilution
Bovine serum albumin (BSA)	Carl Roth (80762)	2 g in 100mL DPBS to have 2% solution
Rabbit polyclonal anti-connexin-43	Sigma (C6219-25UL)	1:500 in 2% BSA solution
Goat anti-rabbit Alexa Fluor 647	Sigma (AF555)	1:500 in 2% BSA solution
Phalloidin-iFluor 488	Abcam (AB176753)	1:1000 in 2% BSA solution
Hoechst 33342 (10mg/mL)	Thermo Fisher Scientific (H3570)	1:10000 in DPBS dilution (1µg/mL)
ProLong™ Diamond Antifade Mountant	Thermo Fisher Scientific (P10144)	
Glass microscope slides	Thermo Fisher Scientific (160005)	
VisiScope CSU-W1 with VS-Homogenizer Spinning Disk	Nikon (VisiScope CSU-W1)	

2.1.5.2. Cell viability assay (MTT assay)

Table 10. The kit for MTT

MTT assay	
Product	**Manufacture**
CellTiter 96® AQueous One Solution Cell Proliferation Assay (MTT assay)	Promega (G3581)

2.1.5.3. Cell proliferation assay (ELISA Bromodeoxyuridine (BrdU))

Table 11. The kit for BrdU

ELISA BrdU	
Product	**Manufacture**
Cell Proliferation ELISA, BrdU (colorimetric)	Roche Applied Science (11647229001)

2.1.5.4. Western blot (WB) analysis

Table 12. The kit, buffers, chemicals, and antibodies for WB

WB		
Product	**Manufacture**	**Concentration**
Bicinchoninic Acid (BCA) Protein assay	Thermo Fisher Scientific (23225)	3 µl per well
Protein ladder	Thermo Fisher Scientific (26616)	
Any kD™ Mini-PROTEAN® TGX™ precast protein gels	BioRad (4569034)	
0.45 µm Nitrocellulose membrane	Amersham (88018)	
Vertical gel electrophoresis system with electrophoresis power supply	Bio-Rad (1645052)	

Blocker™ Casein	Thermo Fisher (37582)	
Rabbit polyclonal anti-Cx43	Sigma (C6219-25UL)	1:2000
Mouse monoclonal anti-ß-actin antibodies	Sigma (A1978)	1:10000
Donkey anti-mouse IgG	LI-COR Biosciences, IRDye® 680RD (926-68072)	1:10000
Donkey anti-rabbit IgG	LI-COR Biosciences, IRDye® 800CW (926-32213)	1:10000
1 M Tris-HCl buffer		
Product	**Manufacture**	**Concentration**
Tris base	Carl Roth (4855.1)	6.05 g
ddH_2O		Up to 50 mL
Adjust to the desired pH 6.8 using 37 % HCl solution		
1x RIPA lysis buffer		
1M Tris-HCl		pH 8.0; 2.5 mL
1M NaCl	Carl Roth (3957.1)	1M; 7.5 mL
1M $MgCl_2$	Carl Roth (2189.1)	1M; 1.25 mL
20% Triton-X 100	Thermo Fisher Scientific (2315025)	0.5 mL
ddH_2O		Up to 50 mL
Halt Protease Inhibitor-Cocktail	Thermo Fisher Scientific (78429)	10 µL/mL
Benzonase	Merck (71206-3)	0.5 µL/mL

4X Laemmli buffer		
1M Tris-HCl		pH 6.8, 10mL
20% SDS	Carl Roth (2326.1)	20 mL
β-Mercaptoethanol	Thermo Fisher Scientific (M6250)	3 mL
Glycerol	Carl Roth (3783.1)	17 mL
Bromophenol blue	Thermo Fisher Scientific (B0126)	0.1 g
PBST wash buffer		
PBS		200 mL
0.05% Tween20	Carl Roth (9127.1)	100 µL
10X T buffer		
Tris base	Carl Roth (4855.1)	30.3 g
Glycine	Carl Roth (0079.1)	143 g
ddH_2O		Up to 1000 ml
Electrophoresis running buffer		
10X T buffer		200 mL
20 % SDS	Carl Roth (2326.1)	10 mL
Blotting buffer		
10X T buffer		200 mL
Methanol	Carl Roth (1A9L.1)	400

2.1.5.5. Flow cytometric measurement

Table 13. The buffers, chemicals, consumables, and device for flow cytometric measurement

Flow cytometry		
Product	**Manufacture**	
FACS tubes	SARSTEDT (551579)	
FACS-Canto II	Becton Dickinson	
FlowJo Software	Ashland (Version 10.4)	
Propidiumiodide (PI) staining buffer		
Product	**Manufacture**	**Concentration**
0.1 % trisodium citrate dihydrate solution	Merck (1.37042.1000)	95 mL
PI stock (1 mg/mL)	SIGMA (P4170)	5 mL, final 50 µg/mL
Triton X-100	SIGMA (T8787)	100 L

2.1.5.6. Transduction of ZsGreen (ZsG) in Med8A

Table 14. The reagents and chemicals of ZsG transduction

ZsG transduction of Med8A cell line	
Product	**Manufacture**
rLV.EF1.Zsgreen1-9	Clontech (0010VCT)
Polybrene®	Santa Cruz Biotechnology (TR-1003)
Puromycin	Gibco (A11138-03)

2.1.5.7. Generation of Cx43- KO clone via Clustered Regularly Interspaced Short Palindromic Repeats/ Nuclease 9 (CRISPR/Cas9) gene editing

Table 15. The kit, chemicals, device, and single guide RNA (sgRNA) sequence of Cx43 KO clone generation

Generation of Cx43 KO clone			
Product			**Manufacture**
Multiple Lentiviral Expression (MuLE) Kit			Addgene (#1000000060)
Quick Ligase			New England Biolabs
LR Clonase II Plus			Thermo Fisher Scientific
Sleeping Beauty Transposase pCMV(CAT)T7-SB100			Addgene (#34879)
Neon Transfection System			Thermo Fisher Scientific
sgRNA	**Target Gene**	**Strand of sgRNA**	**sgRNA sequence**
Cx43/3	*GJA1*	-	TGAGCCAGGTACAAGAGTGT
Non-targeting			GGTCACCGATCGAGAGCTAG

2.1.5.8. Preparation of 3’ RNA sequencing

Table 16. The kit, chemicals, and device of RNA extraction and library preparation and 3' RNA-sequencing

RNA extraction and library preparation and 3' RNA-sequencing	
Product	**Manufacture**
RNeasy mini kit	Qiagen (74004)
Nuclease-free water	NEB (B1500S)
Nanodrop One	Thermo Fisher Scientific
TapeStation System	Agilent

QuantSeq FWD 3'-mRNA-Seq Kit	Lexogen
NovaSeq 6000	Illumina

2.2. Methods

2.2.1. MB cell culture and growth condition

The human primary MB cell lines were cultured in the medium described in **Table 4**, in a humidified incubator at 37°C with 5% CO_2. The Cx43 KO clone was maintained under the same conditions as the wild-type cells, with the addition of puromycin in the culture medium. The Cx43 KO clone was maintained under the same conditions as the wild-type cells, with puromycin included in the culture medium. However, puromycin was not added during the experiments performed in this study. Cell confluency was maintained at 80%, and cells were passaged at a 1:4 to 1:5 ratio to avoid overgrowth. After aspirating the old medium, cells were treated with warm TrypLE to detach them. Following a 3 mins incubation in the incubator, fresh medium was added to stop TrypLE reaction. The cell suspension was then transferred to a new tissue-treated flask containing fresh medium according to the dilution ratio.

2.2.2. Drug dissolution

CCNU, MFA, and TO were dissolved in corresponding dissolvent, ethanol, Ampuwa® water, and DMSO, respectively (**Table 5**). After obtaining 100 mM of CCNU and MFA and a 50 mM stock of TO, all stocks were aliquoted and stored at -20°C. For all experiments, concentrations of 10 µM CCNU, 50 µM MFA and 50 µM TO were used, unless indicated otherwise.

2.2.3. IF staining, imaging, and quantification

2.2.3.1. Staining procedure and image acquisition

For IF staining, Med8A cells were seeded in a cell culture 6 well-plate at a density of 240 × 10^6 cells/well and 200 × 10^6 cells/well of D283 cells on glass coverslips. The adherent cells were fixed after three days seeding with 4% PFA at room temperature (RT) for 15 min followed by permeabilization with 0.1% Triton X-100 and washing three times with DPBS. To prevent non-specific antibody binding, blocking was performed with a 2% BSA solution. The primary antibody, rabbit polyclonal anti-Cx-43 (1:500) was added 50 µl to each coverslip and incubated overnight, and protected from light at 4°C. The next day, the coverslips were washed three times with DPBS, followed by incubation with 50 µL of the solution containing the secondary antibody, goat anti-rabbit Alexa Fluor 647 (1:500), and control strain Phalloidin-iFluor 488 (1:1000), for 45 minutes at RT, protected from light. Subsequently, the coverslips were washed three times with DPBS, and the nuclei were stained with Hoechst 33342 for 5 minutes at RT, protected from light.

After washing twice in DPBS and once in H_2O, the coverslips were finally mounted on glass slides with Prolong Gold.

Confocal images were acquired on the spinning disc microscope, with the 10x, 20x and 40x objective. Z-stack images were acquired to capture the growth of MBs as overlapping clusters. The acquired fluorescence channels were 405, 488 and 640 for Hoechst, Alexa-488 and Alexa 647 fluorophores, respectively. The exposure time and laser strength settings for the acquisition of wild-type MB cells at 40x magnification were as follows: channel 405 at 500 ms, laser strength 25; channel 488 at 200 ms, laser strength 8; and channel 640 at 250 ms, laser strength 10. For the acquisition at 40x magnification, the settings for comparing the #KO2 and #C2 clones were as follows: the exposure time was maintained at 250 ms across all channels, with laser strengths set to 40 for channel 640,

45 for channel 405, and 8 for channel 488. The binning was consistently set to 1. Each parameter settings were kept constant for the acquisition for the same experiment. Three regions of interest (ROI) were randomly selected from per coverslip, which were further used for quantification for both MB cell lines.

2.2.3.2. ImageJ quantification

The intensity of the Cx43 was evaluated semi-quantification from 40x images by ImageJ. Firstly, the image of Alexa-647 single channel was adjusted via Otsu threshold to separate pixels into two classes, foreground and background, following “Particle Analysis”. Open again the original image of Alexa-647 single channel to process “Multiple Measurements” via ROI manager. Afterwards, transformed the data of “Multiple Measurements” to .excel through the plugin “Read And Write Excel”. In Excel, summed up the “Value of Mean” of each particle and withdrew the background noise. The cell nuclei were counted manually to represent the total number of cell number in the image. Finally, the average intensity of Cx43 was the sum of Value of Mean divided with the total nuclei number of the analyzed image.

2.2.4. Cell viability assay (MTT assay)

Cell viability was monitored by CellTiter 96® AQueous One Solution Cell Proliferation Assay, measuring the reduction of a tetrazolium salt (3-(4,5-dimethylthiazol-2-yl)-5-(3-carboxymethoxyphenyl)-2-(4-sulfophenyl)-2H-tetrazolium, inner salt; MTT) to formazan as described previously (Willems et al., 2011). Primary cells were seeded in flat bottom 96-well standard plates at a density of 1.5×10^3 cells/well. After overnight cultivation, the medium was replaced with the medium containing the drug with proposed concentrations of CCNU (0, 0.1, 0.5, 1, 5, 10, 20, 50, and 100 μM), MFA (0, 0.1, 0.5, 1, 5, 10, 20, 50, and

100 μM) or TO (0, 0.1, 0.5, 1, 5, 10, 20, 50, and 100 μM) for 72 hours (hrs) and 144 hrs. Ethanol, ampuwa water, and DMSO were used to be vehicle control to check the toxicity of the solvent for MB cells. On the day reaching 72 hrs and 144 hrs, the viability of cells was measured by aspiring old medium and adding 100 μL of mixture of 1 portion CellTiter 96® reagent to 4 portions of MB culture medium. After an incubation for a 3-hr incubation at 37°C, whole plate was covered with aluminum foil before measurement. Viability was determined by measuring the optical density (OD) at 490 nm, with a reference wavelength of 630 nm for background measurement, using a μQuant microplate spectrophotometer. All values were corrected for background noise and normalized to the mean OD of the control (culture medium only). Each experiment was conducted in biological and technical triplicates. The IC50 values were calculated using the drm function in R, which fits a dose-response curve using non-linear regression.

2.2.5. Cell proliferation assay (ELISA BrdU assay)

Cell proliferation of MBs was evaluated by quantitation of DNA synthesis with Cell Proliferation Elisa, BrdU Kit, as described previously (Bundscherer et al., 2017). Primary MB cells were seeded at a density of 1.5×10^3 cells per well on a 96-well standard plate. After overnight cultivation, the cells were treated with proposed concentrations of CCNU (10 μM), MFA (50 μM) or TO (50 μM) and culture medium as control, following every 48 hrs additional new culture medium or drug-containing medium treatment. At the day reaching 72 hrs and 144 hrs treatment, old medium was removed and 10 μL BrdU Labeling Solution (100 μM) was added to the wells and incubated for 3 hrs at 37°C. Then, the culture medium was aspired and cells of each well were fixed by adding 200 μL FixDenat solution for 30 min at RT. Subsequently, the solution of anti-BrdU antibody coupled with horseradish peroxidase was added 100 μL to each well for 90 min at RT to

bind to BrdU labeling. Colorimetric reaction was produced by adding 100 µL tetramethylbenzidine substrate per well. BrdU incorporation was quantitated colorimetrically at 370 nm and a reference wavelength of 490 nm via the µQuant microplate spectrophotometer. All values were normalized with the mean value of control. Each experiment was performed biological and technical triplicate.

2.2.6. Protein extraction, quantification and WB analysis of Cx43 protein

2.2.6.1. Protein extraction

Total protein extract from cultured cell pallet was prepared in 1x RIPA lysis buffer with the supplements 10 µL/mL Halt Protease Inhibitor-Cocktail and 0.5 µL/mL Benzonase on ice 30 min. The cell lysate was at 13200 rpm, 4 °C for 10 min, and the supernatant was transferred to a new 1.5 mL epi for subsequent BCA analysis.

2.2.6.2. BCA assay

The protein concentrations were determined by BCA Protein Assay as instruction. The BSA standard dilution with different concentrations were plated in triplicates, the protein extractions from **2.2.6.1.** were also placed in duplicates with a water dilution at a ratio of 1:10 in a 96-well tissue culture plate. Afterwards, 200 µL BCA working solution was added to each well and incubated at 37 °C for 30 min. The intensity of the color in each well was measured by a SPECTROstar Nano Absorbance Reader, and protein concentration was calculated by SPECTROstar Nano-Data Analysis software.

2.2.6.3. WB

For electrophoresis, with an appropriate volume of 4X Laemmli buffer was added to the protein samples in a new 1.5 ml epi. A final concentration of 1X Laemmli buffer and 40 µg protein were prepared in 25 µL. Each sample was heat denatured at 95°C for 5 min and

with a protein ladder were loaded on the Any kD™ Mini-PROTEAN® TGX™ Precast Protein Gels for electrophoretic separation. The electrophoresis was performed at 120 V for 60 mins until the ladder and samples had proper separation. Subsequently, the gel was transferred to 0.45 µm nitrocellulose membranes for 45 min at 110 V. The membrane was incubated with Blocker™ Casein in PBS dilution for 1 hr at RT on the tube roller mixer and then incubated with rabbit polyclonal anti-Cx43 and mouse monoclonal anti-ß-actin antibodies in the blocking buffer overnight at 4°C on the tube roller mixer. Subsequently, the membranes were washed three times with PBST for 15 min, and incubated with a mixture of secondary donkey anti-mouse IgG and donkey anti-rabbit IgG at room temperature for 1 hr at RT in the dark on the tube roller mixer. After three times washes with PBST for 15 min, the images of membranes were captured by Odyssey® DLx. Densitometric quantification was performed using CLx Infrared Imaging System and was normalized to the corresponding ß-actin levels.

2.2.7. Flow cytometric measurement

Expanding on the concept introduced by Nicoletti et al. (Nicoletti et al., 1991; Ning et al., 2013) and applied in this thesis, apoptotic cells experience partial DNA degradation. The permeabilization facilitated by triton X-100 results in the extraction of low-molecular-weight DNA, while the undegraded DNA remains within the cell nucleus. These cells manifest as hypodiploid cells, identifiable through the sub-G1 peak in flow cytometry, as readout for cell death.

Cells were seeded at 20 x 10^3 cells/well in 24 well-plates. After overnight cultivation, the cells were treated with respective concentrations of CCNU (10 µM), MFA (50 µM) or TO (50 µM) or a combination (CCNU+MFA or CCNU+TO). Every 48 hrs added another 0.5 mL complete medium or drug-contained medium until 72 hrs or 144 hrs after the first

treatment. On the measured day, old medium was collected in the FACS tubes on ice waiting for further process.

Adhered cells were directly dissociated by warm 200 µL trypLE and incubated 37 °C for 3 mins. Then 400 µL DPBS was added to smoothen reaction and the whole cell suspension was gently pipetting and transferred into the corresponding labeled FACS tubes which contained old medium on ice. Subsequently, all the tubes were centrifuged by 1300 rpm, 5 mins at 4°C and poured the supernatant down gently then resuspending in 100 µL PI staining buffer. After 30 min - 1 h incubation in the dark on ice, all samples were acquired via FACS Canto II. The acquisition settings were kept constant for all samples in this study: FCS threshold at 1000; FSC, SSC, and PI voltages set at 76, 232, and 250, respectively. Each experiment was performed biological and technical triplicate. The percentage of DNA-fragmentation of PI-stained nuclei was gated by FlowJo Software Version 10.4 and was used for specific DNA fragmentation rate calculation with the equation: 100 × (experimental DNA fragmentation (%) - spontaneous DNA fragmentation (%))/(100% - spontaneous DNA fragmentation (%))(Potthoff et al., 2019; Westhoff et al., 2008) In the end, each specific DNA fragmentation rate was normalized by the value of corresponding control.

2.2.8. Neighborhood analysis in ZsG Med8A cell line

2.2.8.1. ZsG transduction of Med8A cell line

To obtain optimal imaging data, the Med8A cell line was transduced with lentiviral particles rLV.EF1.ZsGreen1-9, as previously described (Potthoff et al., 2019). Briefly, Med8A cells were seeded at a density of 30,000 cells per well in a standard 6-well culture plate and prepared for the transduction process in the S2 lab, which was generously provided by Prof. Dr. Michael Hölzel. After 4 hrs of incubation at 37°C with 5% CO_2, the medium in each well was aspirated, and the wells were washed with DPBS. Then, 1 mL of FBS-free medium containing 10 µg/mL of Polybrene® and 0.27 µL of rLV.EF1.ZsG 1-9 (a total of 2.7 x 10^5 functional lentiviral particles) was added to each well. The plate was incubated at 37°C with 5% CO_2 for two days, after which the efficiency of transduction was assessed under a fluorescence microscope.

Following transduction, the medium containing the lentiviral particles was carefully discarded and handled according to S2 laboratory regulations. Fresh growth medium containing 1 µg/mL of puromycin was then added to select for ZsG-transduced Med8A (ZsG Med8A) cells. The plate remained in the incubator in the S2 lab until the cells had been passaged twice. After reaching this stage, the cells were transferred to the S1 lab for subsequent experiments.

2.2.8.2. Live-imaging of neighborhood observation

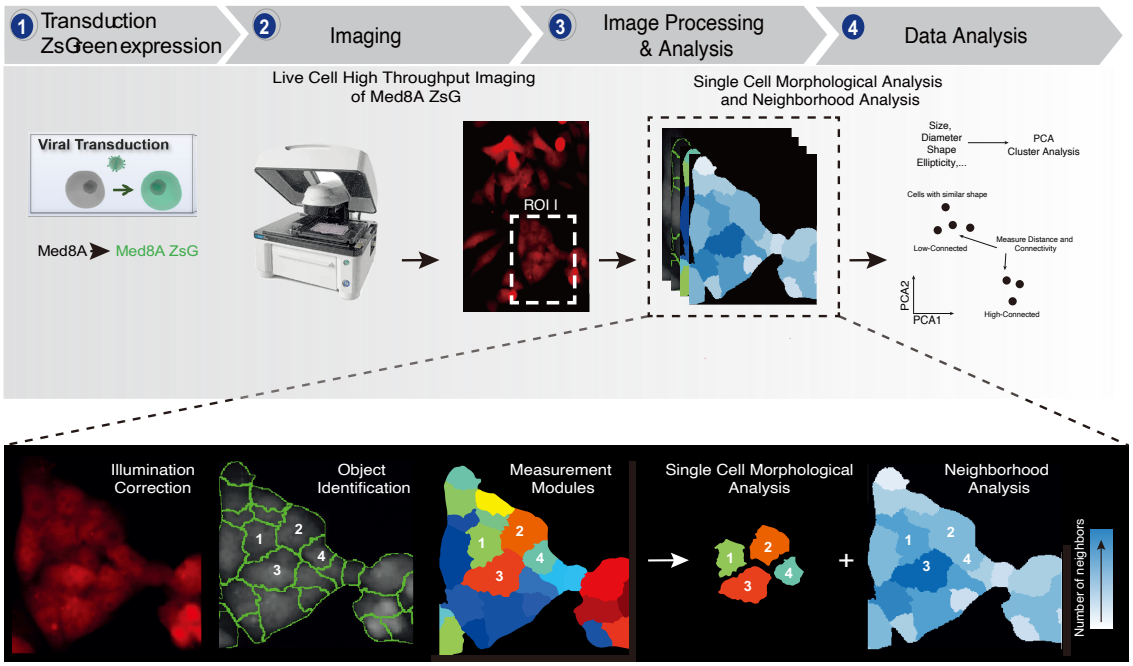

Figure 7. Schematic illustration of the workflow used to explore single-cell morphological connectivity within ZsG Med8A clusters. First, live ZsG Med8A cells were imaged manually using the GFP channel of Lionheart FX Automated Microscope for high-throughput imaging at 72 and 144 hrs, with monotreatment including MFA, TO, or no treatment. Second, the acquired images were processed and analyzed using a custom CellProfiler pipeline, which included several steps for performing neighborhood analysis, as detailed in the black box above. Third, the resulting data were exported as a spreadsheet and subsequently analyzed and graphed using Microsoft Excel and Prism software.

6000 ZsG-tagged Med8A cells were used to acquire live imaging with the Lionheart FX Automated Microscope. After 24 hrs cell seeding in a 24 well-plate, the medium was replaced with 2 mL of fresh medium containing MFA or TO monotreatment and cultured in the incubation of Lionheart FX Automated Microscope at 37°C with 5% CO_2. Multiple ROIs were defined via Gen5 software to avoid the selection bias. Manual acquirement of images of each ROI was taken with 10x magnification from GFP channel of Lionheart FX Automated Microscope followed after 72 hrs and 144 hrs of treatment.

CellProfiler was utilized to process images through several steps, including illumination correction, object identification, measurement modules, single-cell morphological analysis, and neighborhood analysis, to identify individual cells within the clusters. The neighborhood information for each individual cell was provided as spreadsheets. Images containing multiple cellular layers within the clusters were excluded to prevent false recognition by the CellProfiler algorithm. The remaining images (n=19 for each condition, from two independent experiments) were successfully recognized and analyzed for downstream applications.

After obtaining the data from CellProfiler, which identified the number of objective and neighborhood cells for each condition, Microsoft Excel was used to calculate the distribution of cellular neighborhood numbers and the average number of adjacent cells per cell in each image. Since some cells shared the same number of neighboring cells within the same image, the data were grouped, converted into percentages, and normalized to 100% for comparison across images within the same condition. Consequently, Prism produced a heatmap identifying the largest population within 19 ROIs for the control group and those treated with MFA or TO.

2.2.9. Generation of Cx43 KO clones

For the Cx43 CRISPR-Cas9 construct, the MuLE system was employed as previously described (Tews et al., 2019). All vectors were generously provided by Prof. Dr. rer. nat. Pamela Fischer-Posovszky, and the KO constructs were generated by Hannah Strobel. The sgRNA sequences targeting *GJA1*/Cx43, along with a non-targeting control, were designed using CRISPick (Broad Institute, https://portals.broadinstitute.org/gppx/crispick/public) and ordered from Biomers, Ulm. All essential sequences are listed in section 2.1.11. The sgRNA duplexes were cloned into the pMuLE ENTR U6 stuffer sgRNA scaffold L1-

R5 plasmid (kindly provided by Ian Frew (Albers et al., 2015)) via ligation using Quick Ligase and the LR Gateway® cloning strategy (Albers et al., 2015), following the protocol previously described by (Tews et al., 2019). The correct insertion of the sgRNA duplexes was confirmed by Sanger sequencing. The pMuLE ENTR U6-sgRNA and pMuLE ENTR CMV-hCas9 L5-L2 plasmids were then recombined with a Sleeping Beauty transposon plasmid, 'pMuSE eGFP-P2A-PuroR DEST' (previously generated by the Fischer-Posovszky laboratory as described in (Tews et al., 2019)), using LR Clonase II Plus. Med8A cells were co-transfected with the resulting pMuSE U6-sgRNA+CMV-hCas9+RPBSA-eGFP-P2A-PuroR plasmids and the Sleeping Beauty Transposase-expressing pCMV(CAT)T7-SB100 plasmid (kindly provided by Zsuzsanna Izsvak (Mates et al., 2009); http://n2t.net/addgene:34879) in a 19:1 mass ratio using the Neon Transfection System with three 10 ms pulses of 1400 V. Stable bulk cultures were selected following puromycin (1 µg/mL; Sigma, St. Louis, USA) treatment, and single clones were expanded to achieve complete KO confirmation by WB.

2.2.10. Library preparation and 3' RNA-Sequencing

For sequencing, Med8A cells were seeded at a density of 6×10^5 in a 75 cm² cell culture flask. Total RNA was isolated 48 hrs after treatment using the RNeasy Mini Kit according to the manufacturer's instructions. The quantity of RNA was assessed with a Nanodrop, and RNA quality was verified using a TapeStation System, indicated by an RNA Integrity Number greater than 7. Each sample, containing 50–100 ng/µl of total RNA, was diluted with nuclease-free water in a final volume of 14 µL. Library construction was performed and enriched using the QuantSeq FWD 3'-mRNA-Seq Kit, following the manufacturer's instructions, with the procedure executed by the NGS core facility at the University Hospital Bonn. An oligo-dT primer containing an Illumina-compatible sequence at its 5'

end was hybridized to the RNA, followed by reverse transcription. After the degradation of the RNA template, second-strand synthesis was initiated using a random primer that also included an Illumina-compatible linker sequence at its 5' end. The double-stranded library was purified using magnetic beads to remove all reaction components. The library was then amplified to incorporate the complete adapter sequences required for cluster generation, and the final library was purified from polymerase chain reaction components. High-throughput sequencing was conducted as single-end 100 bp sequencing using the NovaSeq 6000, yielding an average of 10 million raw sequencing reads for each sample processed.

2.2.11. Data analysis (RNA sequencing)

For RNA sequencing analysis and visualization, the R/Bioconductor computing platform was used. Initial raw read counts, in a FASTQ file format, were aligned to the Hg38 human reference genome using the 'RSubread' package (Liao et al., 2019). As suggested by Lexogen, the Rsubread align function was executed without trimming but allowing for mismatches in the initial cycles. For the final analysis only those reads, spanning a maximum length of 45 bases were included. The gene level summary was generated with unique mapping using the 'featureCounts' function. The aligned sequencing reads were then assigned to genomic features specified by an ENTREZ Gene ID (NCBI Gene database) (Maglott et al., 2011). Quality control steps such as variance stabilizing transformation and principal component analysis (PCA) have been applied. The differential gene expression analysis for drug responses (CCNU + MFA) was performed using the 'DESeq2' package (Anders and Huber, 2010). The results were filtered for a p-value<0.05 and a log2FC>0.5 and then displayed in a Volcano Plot ('EnhancedVolcano' function). In the Volcano Plot only genes with a p adjusted value < 0.05 and an absolute

log2FC > 0.5 are highlighted in color. The color coding distinguishes between downregulated and upregulated genes, where blue indicates downregulated genes and red indicates upregulated genes, relative to the untreated control. In order to highlight the genes of certain interest, we generated boxplots using the ‘Limma’ package. Subsequently, we performed pairwise t-tests to test for significant differences in mRNA expression levels between the different groups. In addition, Gene Set Enrichment Analysis (GSEA) was performed to identify classes of genes that are over- or under-represented in the large set of genes to retrieve a functional profile in order to better understand the underlying processes after treatment with CCNU + MFA. GSEA was performed using the ‘ClusterProfiler’ package. GSEA plots were generated using the ‘gseaplot2’ function within the ‘enrichplot’ package in R.

2.2.12. Statistics and Visualization

The statistical analysis was done using GraphPad PRISM (Version 9.5.1) and R (version R-4.3.0). Furthermore, the final figures were created using Adobe Illustrator (2023 Version 27.7). One-way ANOVA, as well as Dunnett’s test with correction for multiple testing while Two-way ANOVA followed by Tukey post-hoc test was performed for statistical analysis, as indicated in the corresponding figure legends. Mann-Whitney U-test was performed if only two treatment conditions were compared and data was not normally distributed. Results with adjusted p-value (adj. p-value) <0.05 were considered as statistically significant. *, **, *** and **** denote $p<0.05$, $p<0.01$, $p<0.001$ and $p<0.0001$.

3. Results

3.1. Verification of intercellular Cx43 expression in human MB cells

Two human MB cell lines, Med8A and D283, were utilized in the following experiments. WB analysis confirmed the expression of Cx43 protein in both MB cell lines (**Figure 8A**), with distinct differences observed between them. Densitometric quantification revealed that the Med8A cell line exhibited approximately 4-fold higher Cx43 levels compared to D283 cells (**Figure 8B;** adj. p-value = 0.0039). IF staining was performed to confirm the WB results and to provide information on the localization of Cx43 in MB cells. Both cell lines exhibited Cx43 expression, consistent with the WB results, with more prominent expression observed in Med8A cells (**Figure 8C**). Semi-quantitative analysis indicated that the Med8A cell line expressed a higher level of Cx43 compared to the D283 cell line (**Figure 8D**). Notably, in **Figure 8C**, Cx43 was widely distributed but predominantly localized at cell-cell junctions (indicated by white arrows). The predominant expression of Cx43 protein along cell membrane connections suggests that Cx43 may play a significant role in facilitating intercellular connectivity in MB cells.

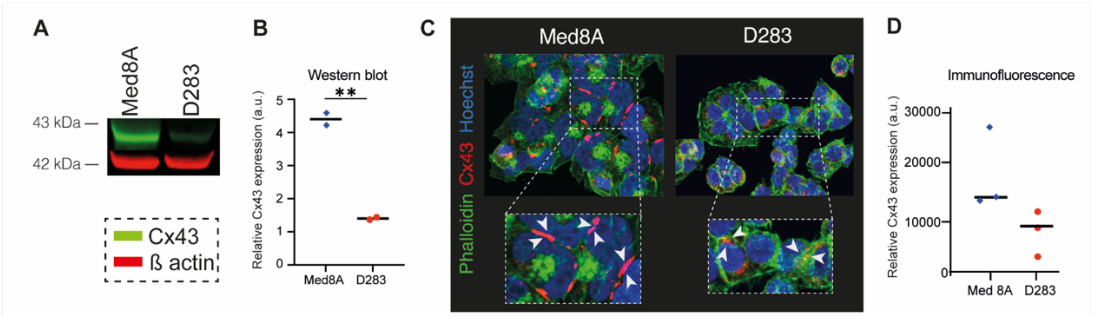

Figure 8. Verification of Cx43 expression in human MB cell lines Med8A and D283. **(A)** Representative WB image verifying Cx43 protein expression in both cell lines (Cx43 indicated by green band). **(B)** Dot plot showing the relative expression levels of Cx43 as determined by WB (n=2; statistical analyses were performed using an unpaired t-test). **(C)** Representative IF images showing Cx43 expression at points of direct intercellular contact

(white arrowheads). **(D)** Dot plot depicting the relative expression levels of Cx43 in IF images for both MB cell lines (n=3). (A.u., arbitrary units).

3.2. Determining optimal concentrations of the pharmacological agents MFA and TO and the chemotherapeutic agent CCNU using cell viability assessment

To analyze whether intercellular Cx43 plays a role in cell-cell connectivity in MB, we decided to pharmacologically inhibit Cx43-mediated GJs. Since Cx43 was confirmed in both Med8A and D283 cells, as described in **Section 3.1**, it was essential to first determine the optimal concentrations of the therapeutic compounds (MFA and TO) and the chemotherapeutic agent (CCNU) to ensure reliable conditions for further experiments. MTT assays were conducted to assess cell viability across various concentrations after 72-hour and 144-hour mono-treatments in both MB cell lines. The primary goal was to identify a concentration range for pharmacological compounds that did not affect cell viability and remained physiologically relevant.

Firstly, a concentration of 100 µM MFA reduced cellular viability to less than 50% in both MB cell lines at both time points (**Figures 9A** and **9B**). Secondly, TO at 100 µM showed no significant reduction in cell viability at 72 hrs for either MB cell line. However, by 144 hrs, it caused a 30% decrease in D283 cell viability compared to the control, reducing it from 1.0 to 0.73 (**Figures 9C** and **9D**). Half-maximal inhibitory concentrations (IC50) were calculated from the MTT results. After 72 hrs, the IC50 values for Med8A cells were MFA: 110.3 µM and TO: 91 µM, while for D283 cells, the values were MFA: 83 µM and TO: 49 µM. At 144 hrs, the IC50 values for Med8A were MFA: 73 µM and TO: 550 µM, and for D283 cells, MFA: 50 µM and TO: 86 µM.

Previous studies have shown that MFA concentration below 50 µM effectively inhibited GJs in human retinal pigment epithelial cells (Ning et al., 2013) and acted as a GJ inhibitor

at 50 μM in a rat seizure model (Nilsen et al., 2006). Similarly, TO at 50 μM was reported to inhibit GJ activity in human brain microvascular endothelial cells, relevant to migraine and epilepsy treatments (Kim et al., 2017). Here, MTT assay demonstrated that 50 μM concentrations of both TO and MFA did not significantly impact cell viability in MB cell lines and were below the IC50 values. Consequently, 50 μM was selected as the concentration for MFA and TO, aligning with physiological relevance and comparable studies.

For CCNU, our goal was to identify the lowest concentration that effectively reduces cell survival in MB cells within a range of physiologically relevant drug concentrations. Previous research has reported an IC50 of 15 μM CCNU in human glioblastoma U373 cells (Baer et al., 1993) and a concentration of 10 μM in leukemic lymphocytes (Bakalova et al., 2020). To determine the appropriate concentration for MB cells, flow cytometry was conducted to measure CCNU-induced cytotoxicity at 10 μM and 20 μM concentrations (**Figure 9G**). At 72 hrs, 10 μM CCNU significantly caused cell death by 13% in Med8A and 23% in D283 cells (adj. p-value <0.0001 and = 0.0097, respectively). A concentration of 20 μM CCNU resulted in a greater than 40% cell death in both cell lines at 72 hrs, however markedly exceeding published drug concentrations mentioned above.

In addition to flow cytometry, a MTT assay was conducted to further evaluate the impact of CCNU on cell viability. The IC50 values for CCNU were found to be 84.2 μM in Med8A and 9.2 μM in D283 cells at 72 hrs, and 16 μM for Med8A and 6 μM for D283 at 144 hrs (**Figures 9E** and **9F**). Combining the results from both flow cytometry and the MTT assay, and considering our objective to achieve physiologically relevant reductions in cell viability, a concentration of 10 μM was selected for subsequent experiments.

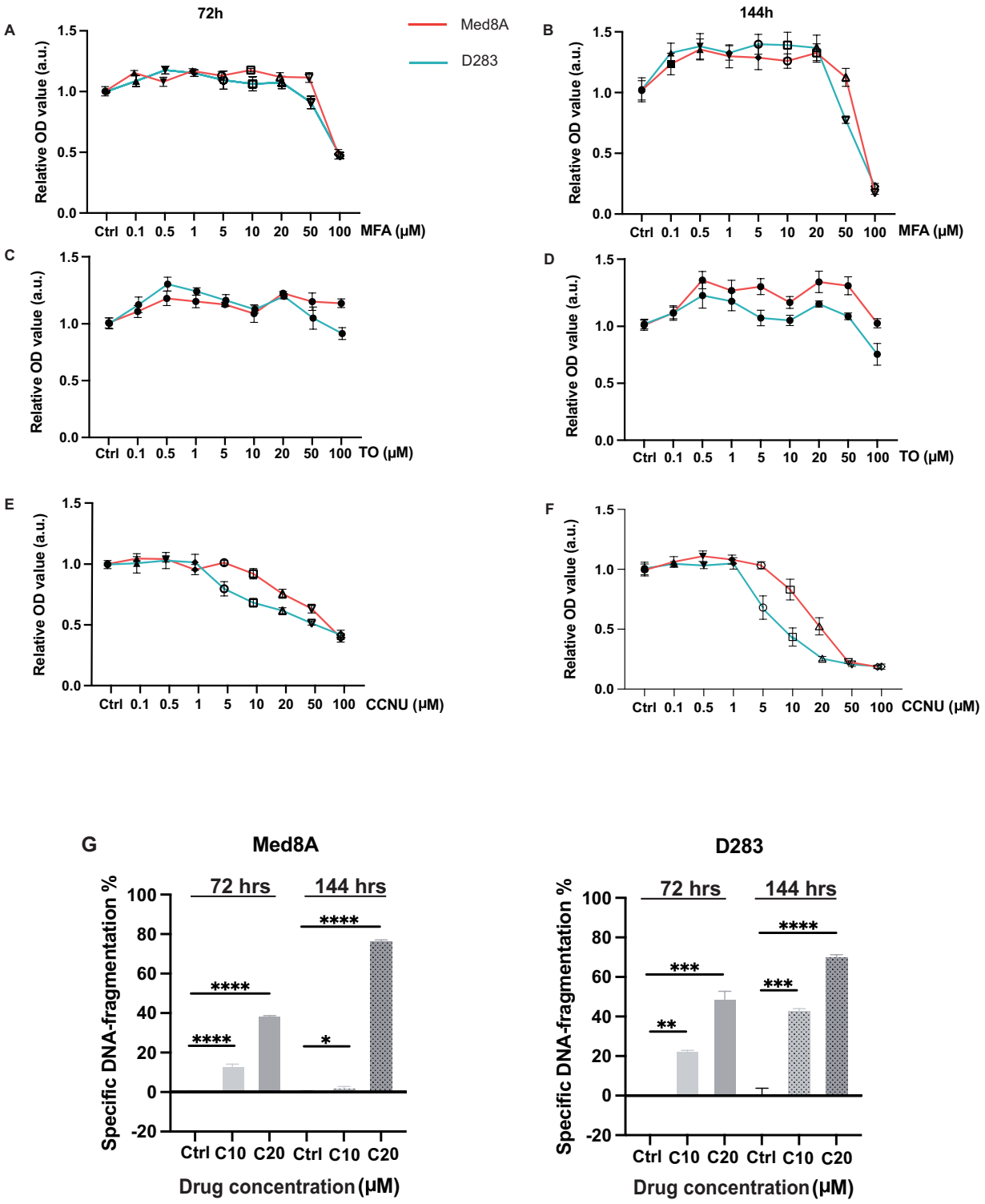

Figure 9. Relative cell viability after treatment with pharmacological compounds MFA and TO, and the chemotherapeutic agent CCNU, assessed at 72 and 144 hrs using MTT assay and flow cytometric analysis. Cell viability was measured via the MTT assay following incubation with MTS at both time points. The X-axis represents the

treatment concentration, ranging from 0.1 to 100 μM, while the Y-axis shows the normalized optical density (OD) values. The curve graph illustrates cell viability for treatments: **(A)(B)** MFA, **(C)(D)** TO, and **(E)(F)** CCNU. Additionally, **(G)** flow cytometric evaluation of CCNU concentration at 72 and 144 hrs in both cell lines (n=2). Statistical analyses between groups were performed using Two-Way ANOVA, followed by Tukey post-hoc test.

3.3. MFA and TO-mediated effects on cellular proliferation in MB cell lines

To determine whether the inhibition of Cx43-mediated intercellular connectivity might affect MB cell proliferation, the pharmacological compounds MFA and TO were utilized. Their impact on the proliferative capacity of Med8A and D283 cells after 72 and 144 hrs of treatment was assessed using a spectrophotometric BrdU assay. This assay leveraged the properties of BrdU, a substance that integrates into actively replicating DNA during the S phase of the cell cycle, allowing for the quantification of proliferating cells. As shown in the results, 10 μM of CCNU had a significant anti-proliferative effect on D283 cells but not on the Med8A population at 72 hrs. However, after 144 hrs, CCNU significantly inhibited the growth capacity in both cell lines (**Figure 10**). Additionally, at 72 hrs, monotreatment with MFA or TO did not result in growth arrest in either MB cell line. In contrast, after 144 hrs, TO exhibited significant proliferative inhibition in both Med8A and D283 cells compared to their respective controls (0.6, with adj. p-value = 0.012, and 0.8, with adj. p-value = 0.026, respectively). The results indicate that MFA did not induce anti-proliferative activity in MB cells, whereas TO required a longer duration to inhibit growth capacity.

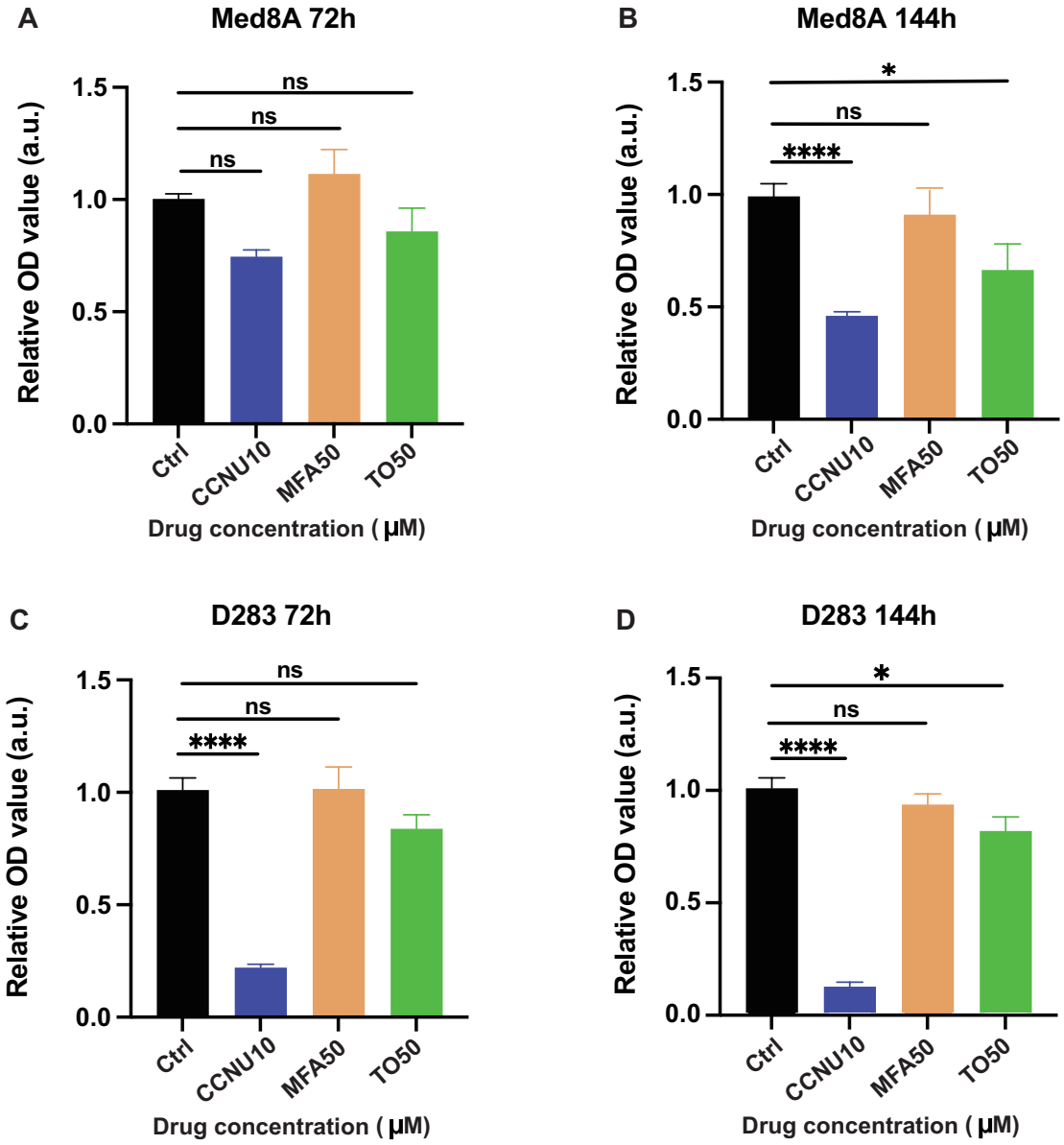

Figure 10. Cell proliferation assessment of Med8A and D283 cells via BrdU assay following 72 and 144 hrs of MFA, TO, and CCNU treatments. (A) In Med8A cells, treatment with 50 μM of MFA and 50 μM of TO did not affect proliferation at 72 hrs. **(B)** Reproductive inhibition was observed with prolonged treatment of 50 μM of TO. **(C)** At 72 hrs, MFA or TO did not affect the growth of D283 cells. **(D)** When it was up to 144 hrs post-treatment, 50 μM of TO resulted in the blockage of cellular growth, mirroring the findings in Med8A cells. All experiments were performed as a biological and technical triplicate. Statistical analyses between groups were performed using One-Way ANOVA followed by Dunnett's multiple comparison test.

3.4. MFA and TO decrease morphological connectivity in MB cells

The role of intercellular communication is becoming increasingly important in CNS tumors, along with the idea of pharmacologically disrupting cell-to-cell networks as a therapeutic strategy. Since MB cells grow in clusters, the number of neighboring cells for each individual tumor cell serves as a surrogate parameter for morphological connectivity between tumor cells. To determine whether treatment with MFA or TO is accompanied by a loss of cell-to-cell tethering in Med8A cells, we conducted neighborhood analysis using live cell imaging. For optimal imaging data processing, accurate cell tracking is essential. Therefore, ZsG Med8A cells were used to acquire live imaging data with the Lionheart FX Automated Microscope. The workflow for neighborhood analysis is described in more detail in the **Section 2.2.8.2**. Firstly, the neighborhood cell number of the largest proportion in each treatment was compared. MFA and TO monotherapies both led to a slight decrease in the number of neighboring cells. At 72 hrs, 27.2% of the population treated with MFA and 33.7% of the population treated with TO had only two neighbors, compared to 22.5% in the control group, which had three neighbors (**Figure 11A**). The same trend was observed at 144 hrs, with the number of adjacent cells in the control group declining from 5 to 4 after MFA treatment and from 5 to 3 after TO treatment (**Figure 11B)**. Secondly, the average number of neighboring cells was compared among the control, MFA, and TO monotreatments. A significant decrease in the average number of neighboring cells was observed. The control group had an average of 2.9 neighbors, which decreased to 2.29 neighbors (adj. p-value = 0.002) after 72 hrs of MFA treatment and further decreased to 1.78 neighbors (adj. p-value < 0.0001) after 72 hrs of TO treatment (**Figure 11C**). At 144 hrs, a more pronounced effect was observed within different conditions. The average number of adjacent cells in the control group decreased

from 4.8 to 3.6 after MFA treatment (adj. p-value <0.0001). The TO group exhibited even lower cellular connectivity, with an average of only 3 adjacent cells (adj. p-value <0.0001) (**Figure 11C**).

This section highlighted the effects of MFA and TO on the morphological connectivity of Med8A cells. The results showed that both treatments reduced the number of neighboring cells in the representative population over time. Statistical analysis confirmed a significant decrease in the average number of neighboring cells for both treatments at 72 and 144 hrs, indicating reduced cell-to-cell tethering as a result of GJ inhibition. Notably, TO had a more pronounced effect than MFA.

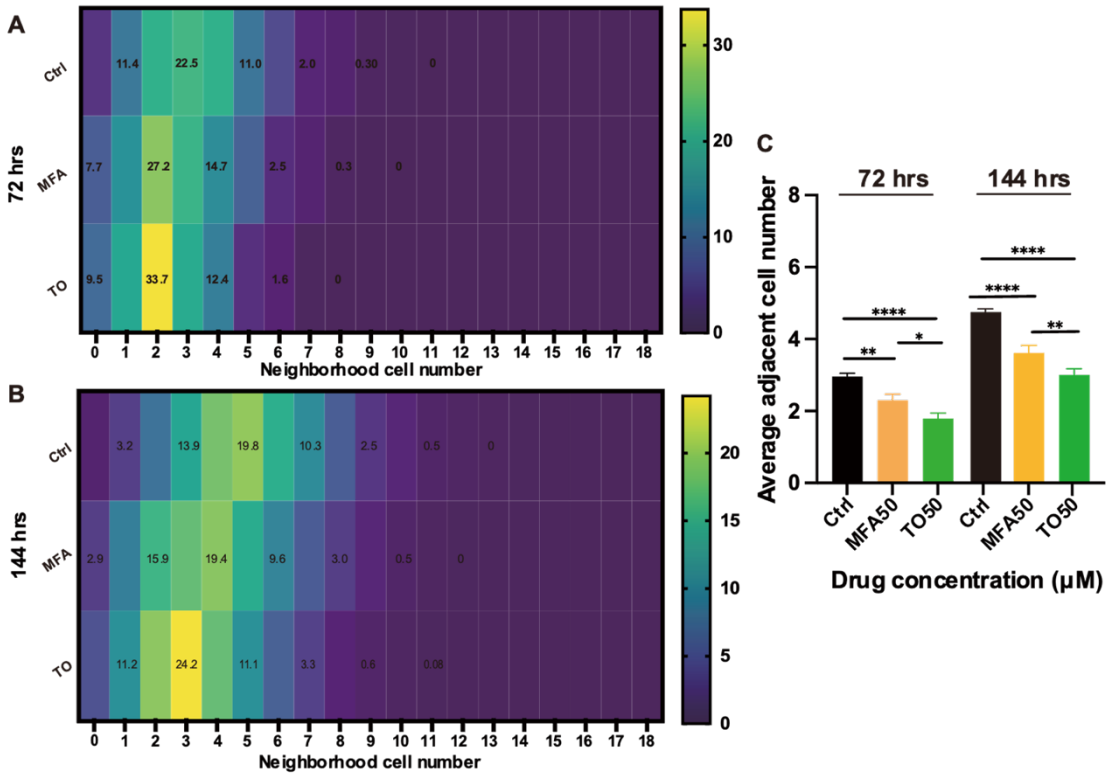

Figure 11. The pharmacological agents MFA and TO weakened intercellular network architectures. (A) The comparison of neighboring cell numbers in the majority population, which constituted 22.5%, 27.2%, and 33.7% of neighboring cells in the control, MFA, and TO conditions, respectively, was conducted at 72 hrs. It showed that the mono-administration of MFA and TO led to a slight decline compared to the control, reducing the number of cells from 3 to 2. **(B)** The comparison of neighboring cell numbers in the majority

population, which constituted 19.8%, 19.4%, and 24.2% of neighboring cells in the control, MFA, and TO conditions, respectively, was conducted at 144 hrs. There was a decrease from 5 cells in the control condition to 4 cells in the MFA condition, and further to 3 cells in the TO condition **(C)** MFA and TO have reduced the average number of adjacent cells per objective since the 72-hour treatment (n = 19). Statistical analyses between groups were performed using Two-Way ANOVA, followed by Tukey post-hoc test.

3.5. MFA and TO enhance the sensitivity of MB cells to CCNU-mediated cell death

There is growing evidence that intercellular communication within syncytial tumor networks is associated with tumor proliferative capacity and resistance to cytotoxic therapies (Chen et al., 2016; Osswald et al., 2015; Schneider et al., 2024; Venkataramani et al., 2022). As shown in **Section 3.4**, MFA and TO exhibited inhibitory effects on the morphological connectivity of MB cells. However, the impact of a morphologically weakened tumor network on the response of MB cells to chemotherapy remains unclear. To investigate whether reduced cellular connectivity may impact the sensitivity of MB cells to chemotherapy, cell death rates were measured via flow cytometry for several treatment conditions using MFA, TO and CCNU, one of the most common chemotherapeutic agents used in MB therapy. To this end, both MB cell lines were treated for 72 and 144 hrs with no treatment (control), monotreatments (MFA, TO, and CCNU), and combinations of CCNU with MFA or CCNU with TO (**Figure 12A**). Flow cytometric measurements were used to evaluate the sub-G1 peak in propidium iodide (PI)-stained nuclei of hypodiploid cells, serving as a surrogate marker for cell death (**Figure 12B**, representative plot from Med8A at 144 hrs). After normalizing to the control values of the corresponding cell line, the specific DNA fragmentation rate, used as a surrogate readout for cell death, was obtained. Monotreatment with MFA and TO did not result in increased cytotoxicity compared to the control in either cell line. For instance, after 144 hrs of exposure, Med8A

cells exhibited a specific DNA fragmentation rate of 0.27% following MFA treatment (adj. p-value = 0.9983) and 0.94% following TO treatment (adj. p-value > 0.9999), as shown in **Figure 12D**. This also suggests that the reduction in morphological connectivity observed under MFA and TO in **Section 3.4** was not due to elevated cell death rates but attributable to their inhibitory effects on morphological cell-cell connectivity. With 10 μM of CCNU, the observed CCNU-mediated death rates in Med8A cells were 12.6% at 72 hrs and 8.9% at 144 hrs (**Figure 12C** and **12D**). In D283 cells, cell death of 8.8% was observed after 72 hrs of 10 μM CCNU treatment, increasing to 16.7% after 144 hrs (**Figure 12E** and **12F**). Furthermore, the results showed that MFA and TO increased the susceptibility of MB cells to CCNU-induced cell death. Firstly, the combination of CCNU and MFA showed a sensitizing effect on both cell lines at 72 hrs and 144 hrs (**Figure 12C-F**). Specifically, the Med8A cell line demonstrated greater sensitivity to the MFA+CCNU combination, nearly doubling the CCNU-induced cytotoxicity at both time points—from 12.7% to 25% at 72 hrs (adj. p-value <0.0001; **Figure 12C**) and from 8.9% to 16.9% at 144 hrs (adj. p-value <0.0001; **Figure 12D**). Moreover, MFA also sensitized D283 cells to CCNU treatment, enhancing cytotoxicity from 8.8% to nearly 16% at 72 hrs (adj. p-value <0.0001; **Figure 12E**) and from 16.7% to 25% at 144 hrs (adj. p-value <0.0001; **Figure 12F**). Secondly, the combination of TO and CCNU also enhanced the cytotoxicity of CCNU, from 8.9% to 13.4% in the Med8A population (adj. p-value = 0.0048; **Figure 12D**) and from 16.7% to 23.4% in D283 cells at 144 hrs (adj. p-value = 0.005; **Figure 12F**). Compared to MFA, TO required a longer duration to sensitize MB cells to CCNU. As shown in the results, MFA enhanced CCNU-mediated cell death in both cell lines starting at 72 hrs, while TO exhibited sensitizing effects only at 144 hrs. Collectively, these findings show that MFA and TO significantly increased CCNU-induced cell death in MB cells, respectively.

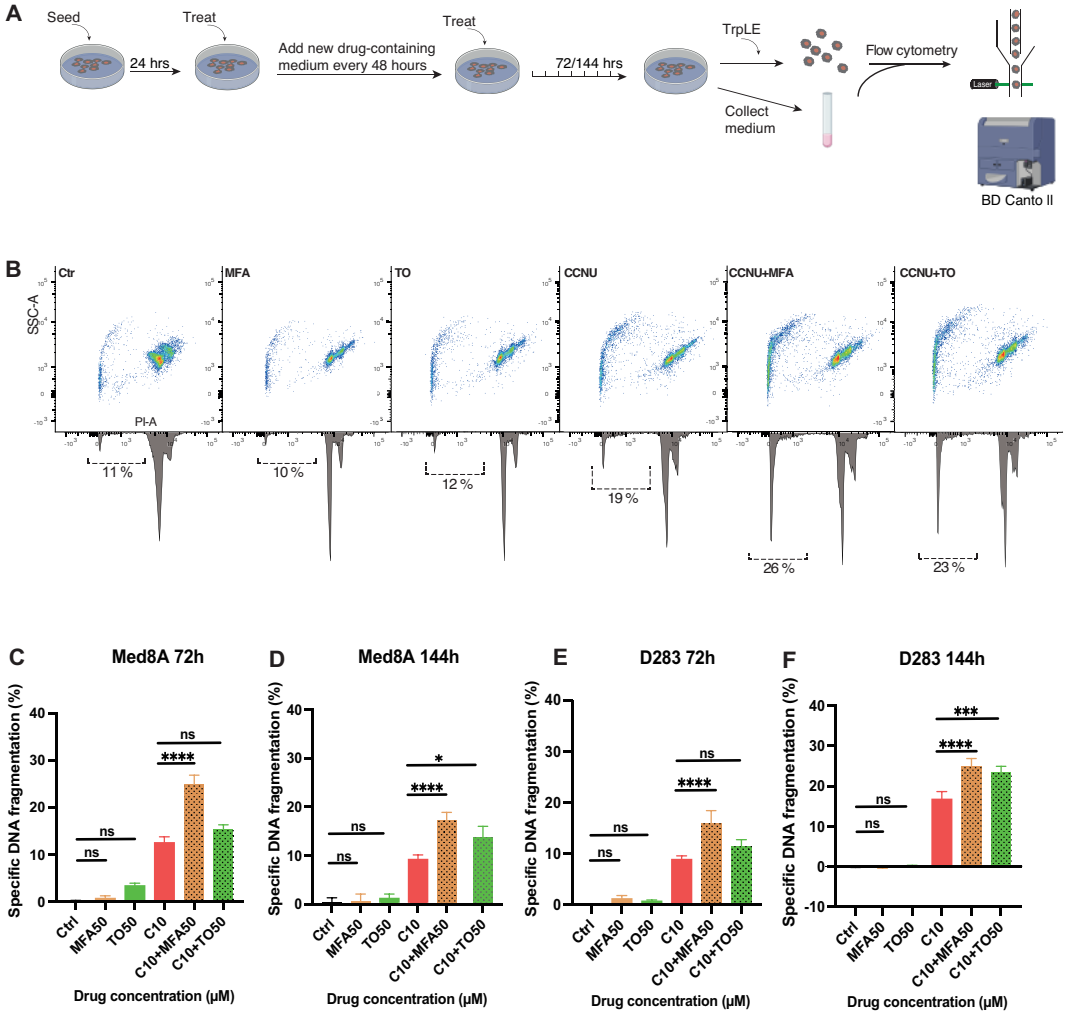

Figure 12. MFA and TO enhance MB cells sensitivity to CCNU-induced cell death. (**A**) Workflow illustration of flow cytometric measurement of cell death: Cells were treated with MFA, TO, CCNU, CCNU+MFA, and CCNU+TO for 72 hrs and 144 hrs, with subsequent repeated treatments every two days. For staining with PI, cells were dissociated using TrypLE and combined with collected medium to assess the DNA fragmentation of PI-stained nuclei via flow cytometry. (**B**) Representative plots from flow cytometric analysis. Sub-G_1 was measured as a readout for cell death and was accentuated within the histograms. **(C)** At 72 hrs, the specific DNA fragmentation rates on the Med8A population showed a synergistic effect from MFA+CCNU **(D)**, while at 144 hrs, the influence of TO+CCNU began to emerge. **(E)** MFA in combination with CCNU sensitized D283 cells both at 72 hrs and at 144 hrs of treatment. **(F)** Similar to Med8A, TO + CCNU required a longer period to render D283 cells more vulnerable to CCNU. Statistical analyses between groups were performed using Two-Way ANOVA, followed by Tukey post-hoc test, with n=15 for Med8A cells and n=12 for D283 cells.

3.6. MFA-mediated sensitizing effects are accompanied by wound-healing related transcriptional alteration in Med8A cells

Regarding the findings that GJ inhibition significantly increased tumor cells' susceptibility to CCNU therapy, we next analyzed gene expression changes under this therapeutic approach. To investigate these changes, 3'-mRNA sequencing was employed to compare transcriptional alterations between the combined treatment of CCNU with MFA and the tated control condition (**Figure 13A**). To avoid observing predominant cell death, as shown in **Figure 12C**, an earlier time point of 48 hrs was chosen. This time frame was assumed to enable the study of compensatory signaling pathways, potentially revealing the mechanisms by which cells respond to early stress induced by connectivity interruption and subsequent chemotherapy.

After 48 hrs of combination treatment, numerous differentially expressed genes (DEGs) (Log2 fold change ≥ 0.5) were identified between the two groups, as illustrated in **Figure 13B**. Notably, genes related to cellular proliferation (*ITGA10*, *CYTB*, *CYB561*) and ECM formation (*COL27A1*) were among the most distinctly upregulated. In contrast, some genes associated with apoptosis (*TUBA1B*, *PFN1*) and proliferation (*AQP1*, *HNRNPD*) were significantly downregulated following MFA-CCNU combination treatment. To gain deeper insight into the underlying pathways affected by the combination treatment compared to the untreated group, Gene Set Enrichment Analysis (GSEA) was performed on all DEGs. Additionally, Gene Ontology (GO) functional enrichment analysis was carried out to assess the biological roles of the identified gene sets. **Figure 13C** displays the top 15 significantly upregulated and downregulated GO Biological Processes (BPs). Remarkably, the most prominent activated functional terms — syncytium formation, ECM organization, external encapsulating structure organization, regulation of locomotion,

response to wound healing, and blood vessel development — were closely associated with wound healing mechanisms. In contrast, the most significantly downregulated BPs, including rRNA processing, mitochondrial translation, rRNA metabolic process, ribonucleoprotein complex assembly, and ribonucleoprotein complex biogenesis, were linked to apoptotic responses. GSEA further validated these findings (**Figure 13D**), showing that positively correlated pathways strongly promoted the proliferation and remodeling phases of wound repair. Key pathways included response to growth factor, ERK1/2 cascade activation, and regulation of angiogenesis. Moreover, DEGs such as *MAPK8IP3*, *PLCB2*, and *Rab26* exhibited significantly higher expression in the combined treatment group compared to the control (**Figure 13E**). These genes are closely related to tumor invasion, progression, and apoptosis.

The selection of an early measurement time point was deliberate, enabling the investigation of compensatory responses prior to the dominance of apoptosis signaling. Sequencing data from this early stage revealed that Med8A cells upregulated wound healing pathways as a compensatory mechanism, while apoptosis signaling remained relatively low. The combination treatment of MFA and CCNU modulated gene expression to influence proliferation, apoptosis, and wound healing processes. These findings highlight the interplay of multiple pathways in tumor progression, providing insights into the cellular responses elicited by disrupted connectivity and chemotherapy.

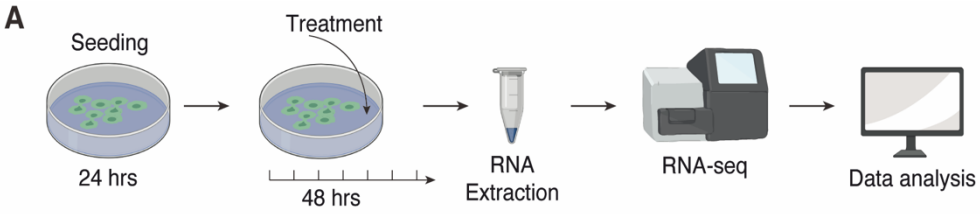
A
Seeding
24 hrs
Treatment
48 hrs
RNA
Extraction
RNA-seq
Data analysis

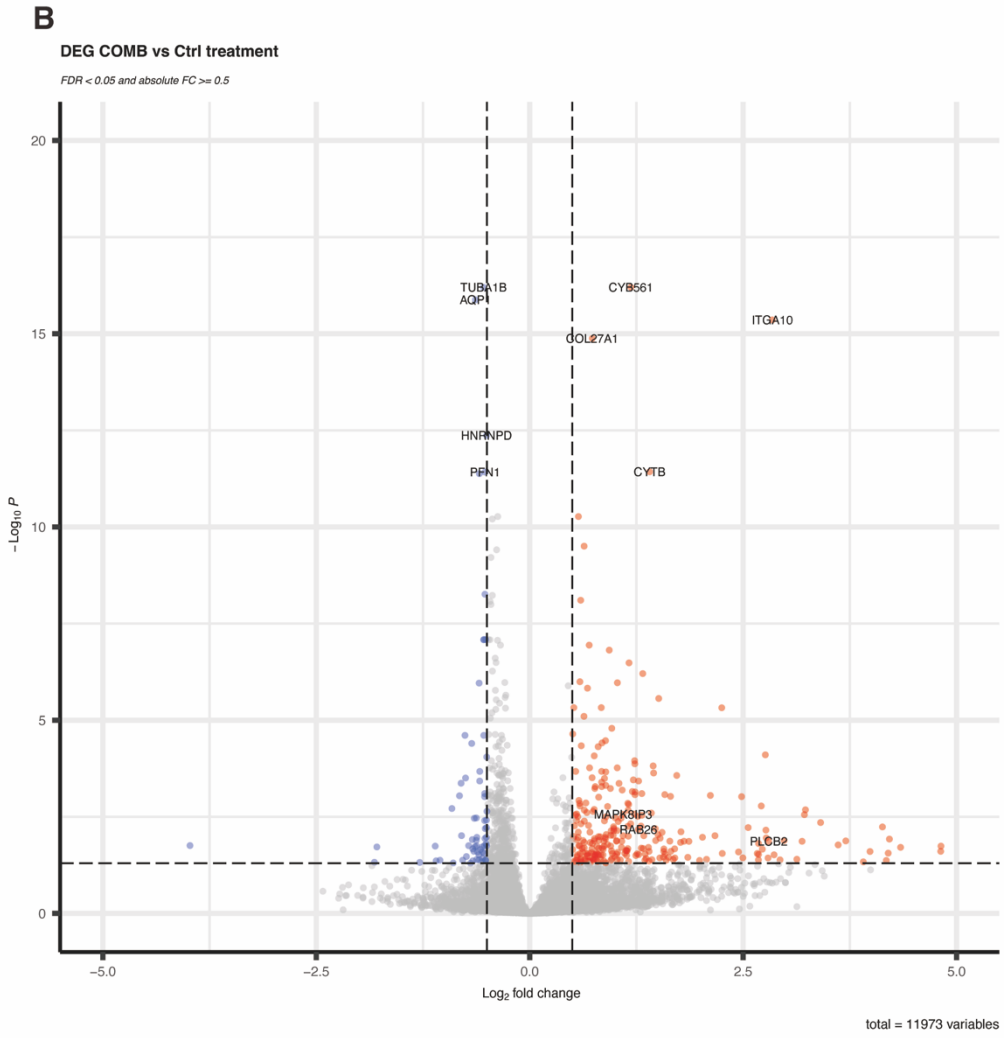
B
DEG COMB vs Ctrl treatment
FDR < 0.05 and absolute FC >= 0.5
TUBA1B
AQP1
CYB561
ITGA10
COL27A1
HNRNPD
PFN1
CYTB
MAPK8IP3
RAB26
PLCB2
−Log10 P
Log2 fold change
total = 11973 variables

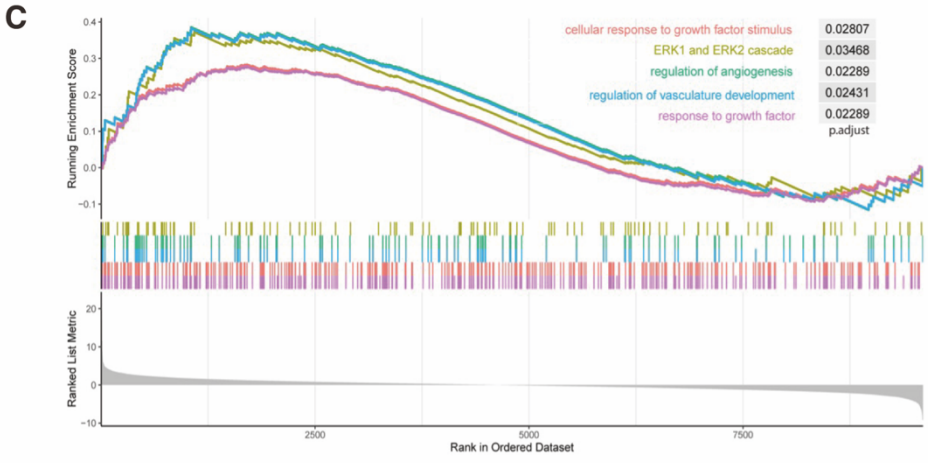
C
cellular response to growth factor stimulus 0.02807
ERK1 and ERK2 cascade 0.03468
regulation of angiogenesis 0.02289
regulation of vasculature development 0.02431
response to growth factor 0.02289
p.adjust
Running Enrichment Score
Ranked List Metric
Rank in Ordered Dataset

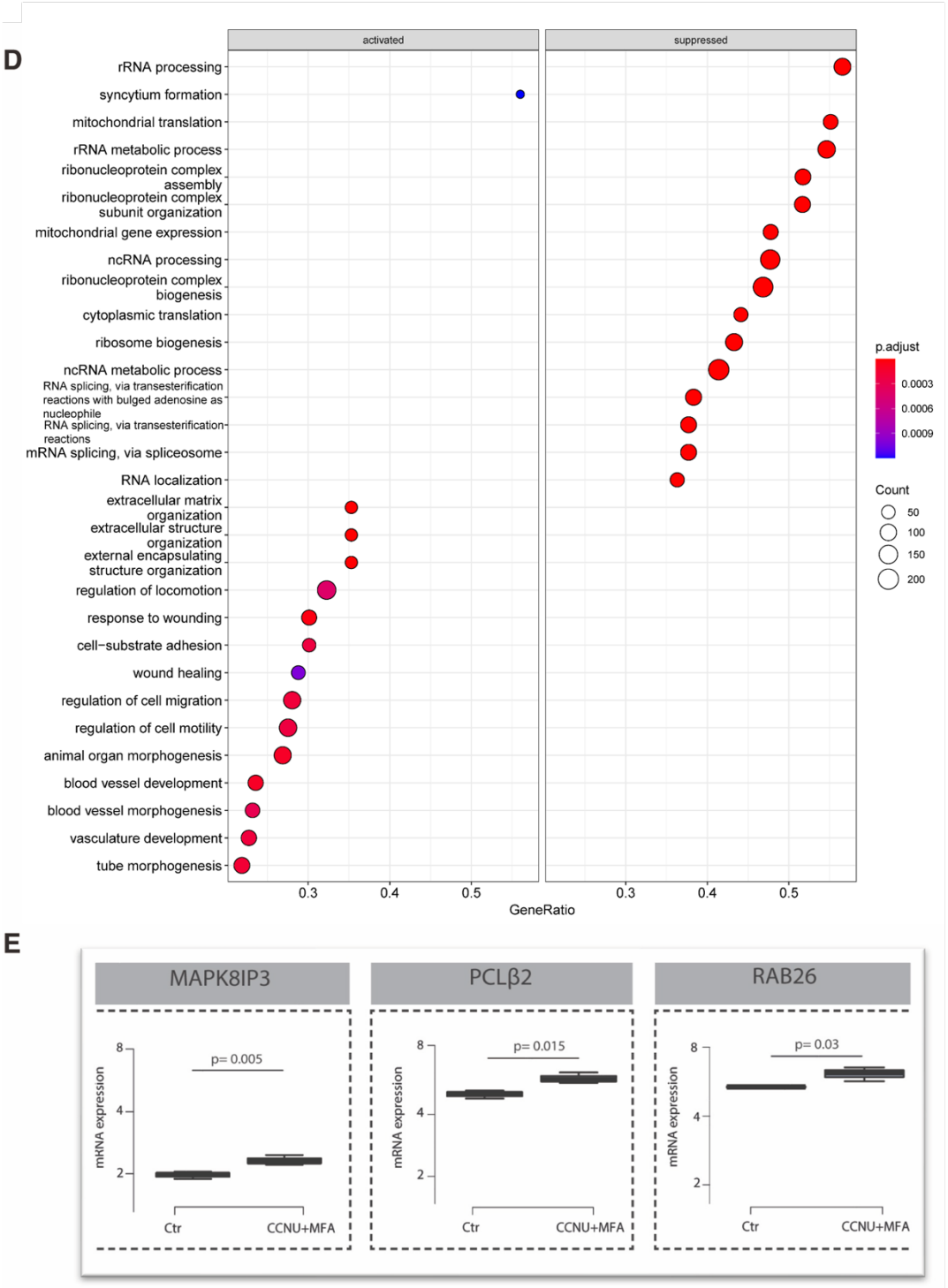

Figure 13. The DEGs and BPs of MFA promoted CCNU-mediated cytotoxicity were associated to wound-healing process and apoptosis response. (A) Graphical procedure for 3'-mRNA sequencing. **(B)** Volcano plot presenting the DEGs for MFA with CCNU treatment compared to untreated control. *ITGA10*, *CYTB*, *CYB561*, and *COL27A1*, four most significantly upregulated genes, were linked to wound healing process or cellular proliferation. While *TUBA1B*, *AQP1*, *HNRNPD*, and *PFN1* were the four significantly

downregulated genes which were related to apoptotic response. **(C)** The dot plot of GO analysis of enriched terms elucidating top 15 activated and suppressed BPs which facilitate repair mechanism and apoptosis. **(D)** The plot of GSEA presenting top upregulated GO terms was associated to cellular proliferation and remodeling phases of wound healing. **(E)** Boxplots depicting that *MAPK8IP3*, *PLCB2*, and *Rab26* were demonstrated profoundly higher expression in the combined treatment group compared to the control. These genes were tightly associated to tumor progression and apoptosis.

3.7. Generation of a Cx43 KO in Med8A cell line

The findings from **Section 3.4** and **3.5** indicate that MFA and TO reduced cellular connectivity and increased the susceptibility of Med8A and D238 cells to CCNU-induced toxicity. To cross-verify whether these effects were at least in parts reduced to Cx43 inhibition, we designed a Cx43 KO clone to specifically eliminate Cx43 expression. Since **Section 3.1** and **3.5** revealed that the Med8A cell line had markedly higher Cx43 levels than the D283 cells as well as exhibited a greater sensitization effect to the combination treatments, Med8A cell line was selected for the following KO procedure to facilitate a better comparison. A KO of Cx43 protein was achieved by using CRISPR/Cas9 vector that expresses Cas9 nuclease and gRNA targeting exon 2 of the Cx43 gene *GJA1*. This resulted in the generation of the Cx43 KO clone, named #KO2 (**Figure 14A**). The corresponding control clone, #C2, was transduced with an empty vector that lacked gRNA insertion. The following experiments with #KO2 used the #C2 clone as a control. Stable bulk cultures were established through puromycin selection, and Cx43 depletion was confirmed by WB and IF staining. First, WB analysis verified Cx43 KO, as shown by densitometric quantification (**Figure 14C** and **14D**), indicating a lack of Cx43 expression. Second, IF images showed no Cx43 in #KO2 cells (**Figure 14B**), while in the #C2 clone, Cx43 was predominantly localized at cell-to-cell junctions, similar to its distribution in the Med8A line (**Figure 8C**). These findings confirmed the successful generation of the Cx43

KO cell clone #KO2.

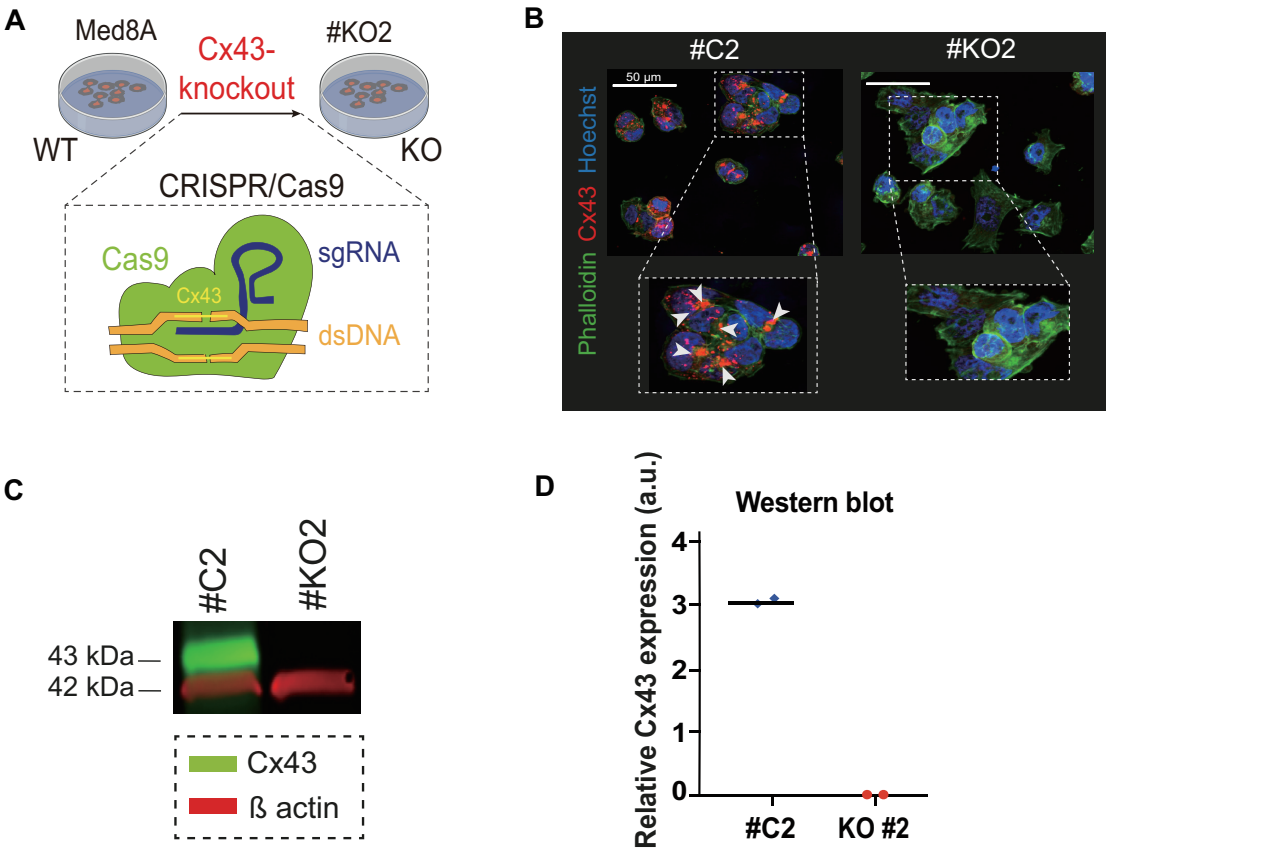

Figure 14. Generation and validation of Cx43 KO clone using CRISPR-Cas9 technique. (A) Workflow illustration of CRISPR/Cas9-based frameshift to knock out the Cx43 protein, utilizing the primary Med8A cell line to create the #KO2 clone. **(B)** Representative IF image depicting Cx43 staining for #KO2 and the corresponding wildtype control population #C2. White arrows indicate Cx43 expression in #C2, particularly highlighting intercellular localization. However, no visual evidence of Cx43 expression was observed in #KO2. **(C)** Cx43 protein expression was assessed via western blot analysis to verify the significant reduction in Cx43 protein expression in the #KO2 clone (green band). **(D)** Densitometric quantification from the western blot result was carried out via Image Studio Software (n=2).

3.8. Cx43 KO leads to reduced morphological connectivity in Med8A cells

To explore the role of Cx43 for morphological connectivity of MB, a neighborhood analysis was conducted to compare ZsG-labeled Med8A cells (ZsG Med8A, as control) and #KO2 clone in untreated conditions. After 72 hrs of observation, there was only a slight decrease

in the number of neighboring cells in the largest population, from 3 to 2 for ZsG Med8A (22.5%) and #KO2 cells (28.7%), respectively (**Figure 15A**). In contrast, a noticeable reduction was observed at 144 hrs (**Figure 15B**). At this time, the largest proportion of ZsG Med8A cells (19.8%) had 5 neighboring cells, while the #KO2 cell population (19.6%) had 3 neighboring cells. Moreover, a similar significant decreasing trend was observed in the overall average number of neighboring cells per cell at 144 hrs, with ZsG Med8A cells having 4.8 neighboring cells compared to 3.9 in #KO2 cells (**Figure 15C**; adj. p-value = 0.0003). In conclusion, deprivation of Cx43 resulted in a significant decrease in a number of cellular neighborhoods at 144 hrs, as well as a reduction in the average number of neighboring cells per cell. Taken together, Cx43 plays a significant role in maintaining morphological intercellular connectivity within Med8A cell networks. The elimination of Cx43 appears to disrupt this connectivity, leading to a higher degree of morphologically isolated tumor cells.

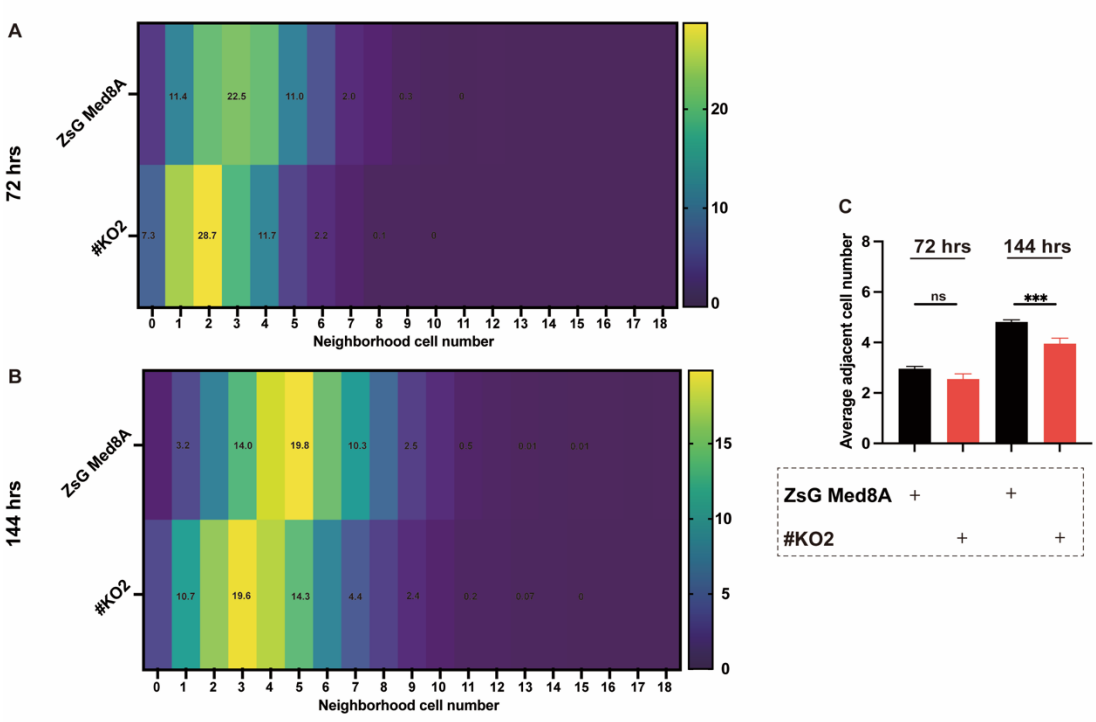

Figure 15. Morphological network disconnection occurs as a result of Cx43 KO. (A)

The neighborhood cells of the largest KO #2 population (28.7%) showed a subtle decrease compared to the largest population of ZsG Med8A (22.5%) at 72 hrs, decreasing from 3 cells to 2 cells **(B)** At 144 hrs, the number of neighboring cells in KO #2 (19.6%) decreased compared to ZsG Med8A (19.8%), from 5 cells to 3 cells. **(C)** From the view of average adjacent cells per cell in each cell clone, there was no variation at 72 hrs but 144 hrs. #KO2 clone had noticeably less cellular connection than ZsG Med8A cells. n=19, statistical analyses between groups were performed using Two-Way ANOVA, followed by Tukey post-hoc test.

3.9. KO of Cx43 heightened the sensitivity to CCNU in Med8A cells

The next question was whether Cx43 deprivation also increased sensitivity to CCNU-mediated cell death, as observed with MFA and TO treatment in **Section 3.5**. To address this, flow cytometry was employed to evaluate DNA fragmentation in PI-stained nuclei (Nicoletti et al., 1991) as mentioned previously. The specific DNA fragmentation rate was used as a surrogate marker for cell death in the #KO2 and #C2 clones. The goal was to determine whether the #KO2 clone treated with CCNU alone would exhibit results similar to those of #C2 cells treated with CCNU in combination with MFA or TO.

Flow cytometric measurements at 144 hrs revealed that the #KO2 clone exhibited a higher cell death rate compared to the #C2 clone, even in the absence of drug treatment (**Figure 16A**). Furthermore, as shown in **Figure 16C**, monotherapy with MFA or TO did not increase cell death rates in #C2 cells compared to control populations (without treatment, adj. p-value < 0.9999), consistent with observations in the Med8A cell line described in **Section 3.5**. Similarly, no significant decrease in viability was observed in the #KO2 cell line with MFA or TO monotherapy, even under conditions of Cx43 deprivation (adj. p-value < 0.9999).

Next, **Figure 16B** shows that the cell death rate in #KO2 cells treated with CCNU alone (36%) was significantly higher than in #C2 cells treated with CCNU in combination with

MFA (22%, adj. p-value = 0.0003) or CCNU with TO (21%, adj. p-value < 0.0001), as shown in **Figure 16C**. A corresponding sensitizing effect on CCNU-mediated cytotoxicity was observed when #C2 cells were treated with CCNU in combination with either TO or MFA.

These findings suggest that the loss of Cx43 protein is associated with increased spontaneous cell death in culture and enhanced susceptibility to the tumor-killing effects of CCNU. Notably, the sensitizing effect in the #KO2 cells was even more pronounced than in #C2 cells. Furthermore, these results confirmed that the effects described in **Sections 3.4–3.6** were, at least in part, mediated by Cx43 GJ inhibition induced by MFA and TO.

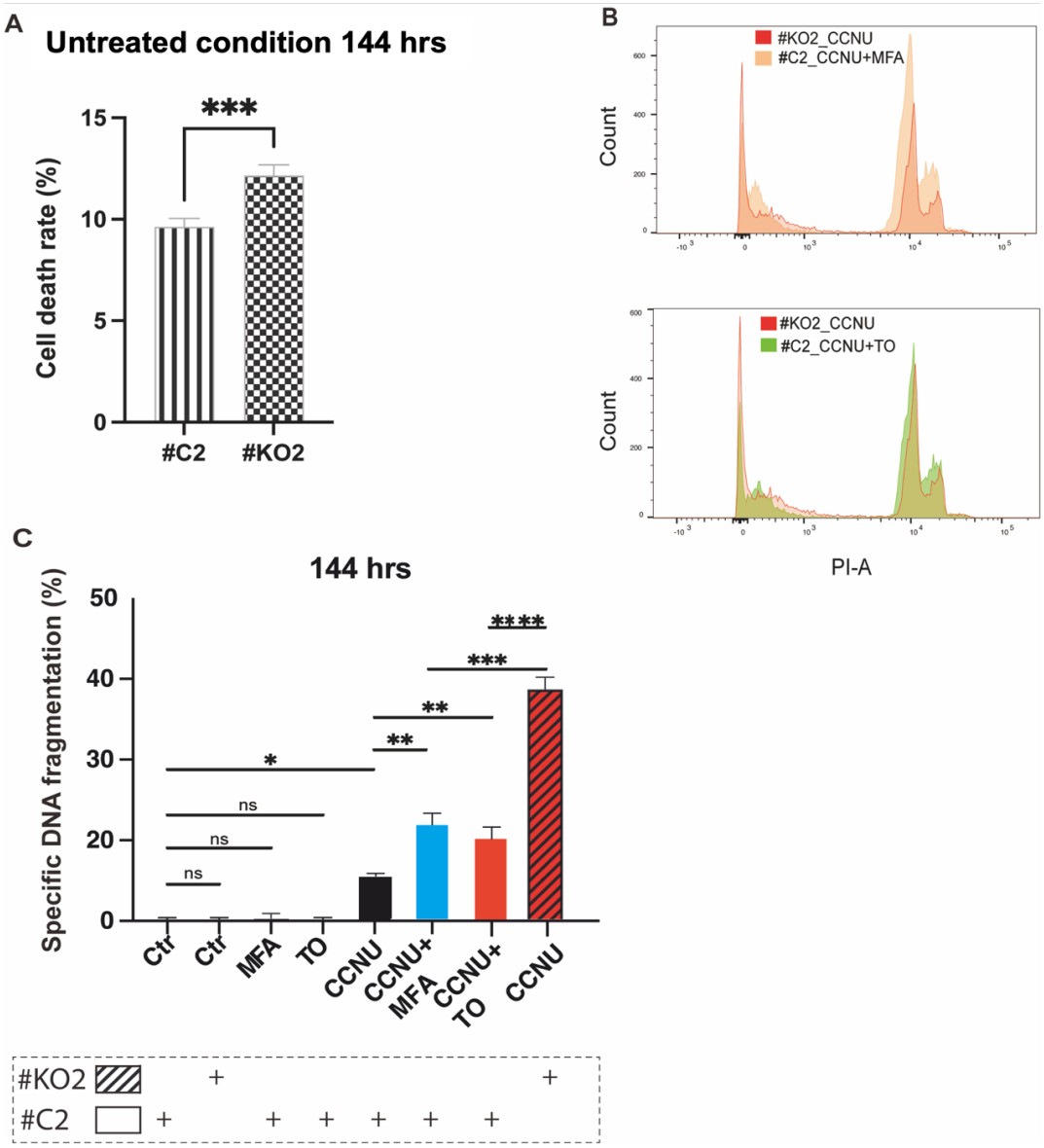

Figure 16. Cx43 KO increased the sensitivity to CCNU in Med8A cell line at 144 hrs. **(A)** The comparison of cell death rate between #C2 and #KO2 without treatment. #KO2 exhibited a lower viability compared to the control clone. n=12, a Mann-Whitney test was performed. **(B)** Representative histogram plots are shown the sub-G_1 comparison of #KO2 with only CCNU application (red) and #C2 treated with CCNU+MFA (orange) and CCNU+TO (green). **(C)** MFA and TO monotherapy had no effect on viability in the #C2 and #KO2 cell lines. In contrast, the combination treatments of MFA with CCNU and TO with CCNU exhibited a sensitizing effect in #C2 cells. Notably, CCNU administration significantly elevated DNA fragmentation levels in #KO2 cells, surpassing even the combination therapies (CCNU + MFA and CCNU + TO) in #C2, as revealed by flow cytometric analysis. n=12, statistical analyses between groups were performed using Two-Way ANOVA, followed by Tukey post-hoc test.

4. Discussion

This study aimed to define the role of Cx43-based GJs in supporting malignant connectivity in MBs. To explore this, non-WNT/non-SHH MB cell lines Med8A and D283—representing high metastatic risk groups that comprise over two-thirds of MB cases (formerly categorized as groups 3 and 4) (Ivanov et al., 2016; Louis et al., 2021; Mynarek et al., 2023; Schoen et al., 2022), —were used. Pharmacological GJ inhibitors, MFA and TO, were applied to provide clinically relevant insights into the role of Cx43-based GJs in MB. These findings were further validated using a Cx43 KO model to directly assess how disrupting Cx43 connections impacted cell morphology and sensitivity to chemotherapy. Together, these approaches enabled a comprehensive investigation into Cx43's contribution to malignant connectivity in MB cells.

First, Cx43 expression was confirmed via WB and IF staining in MB. MFA and TO, as pharmacological GJ inhibitors, affected the clustering morphology of ZsG Med8A cells through live-imaging observation, resulting in fewer adjacent connections. Furthermore, MB cells with inhibited network connectivity exhibited significantly increased sensitivity to CCNU-mediated toxicity. The CRISPR/Cas9 Cx43 KO model confirmed that the effects observed with pharmacological treatments were indeed due to drug-mediated Cx43 inhibition. This validation further elucidated the role of Cx43 in MB cells, particularly through neighborhood analysis and flow cytometric measurements. Transcriptomic profiling revealed that additional Cx43 inhibition, induced by MFA combined with CCNU, not only activated apoptosis pathways but also upregulated wound-healing-associated pathways in Med8A cells. This suggested that, following the disruption of tumor networks, MB cells engaged compensatory mechanisms that enhanced their survival and repair processes despite the initial induction of apoptosis. These findings highlighted the adaptive responses of MB cells to targeted therapies and the potential for therapeutic

resistance through compensatory mechanisms. They also underscored the importance of Cx43-based GJs in MB progression, suggesting that GJ inhibitors could offer a promising therapeutic strategy.

4.1. Cx43 expression levels differ in Med8A and D283 cells

To examine the hypothesis of this study, Med8A and D283 cells were used to represent the non-WNT/non-SHH MB group. We found that both MB cell lines expressed the Cx43 protein, as evidenced by IF and WB results. Cx43 is known to form GJs, contributing to intercellular communication, cell-to-cell adhesion, and signal transmission. As expected, we observed that Cx43 proteins localized in a punctate or large-plaque-like pattern at the cell-cell boundary in the IF staining.

Cx43 observed along the plasma membrane indicates the presence of close cell-cell contacts, suggesting its involvement in facilitating intercellular communication. Specifically, Cxs in GJ channels directly connect adjacent cells, enabling the exchange of small signaling molecules such as cAMP and Ca^{2+} to synchronize cellular activities. Additionally, Cx43, when functioning as HCs, supports the transport of small ions, metabolites, and ATP between cells and the extracellular space (Pollmann et al., 2005; Tarzemany et al., 2017). This role aligns with our observation of Cx43 localization at cell-cell junctions in IF images, reinforcing its association with intercellular trafficking and adjacent cell interactions. Such close contact between cellular plasma membranes, formed by Cx43-based GJs, further highlights their potential contribution to facilitating intercellular communication and adjacent cell coordination.

It is interesting to note that a distinct difference in Cx43 expression existed in these two high-grade MB cell lines. Few studies have examined the expression of Cx43 in the D283 cell line compared to other MB cell lines. Findings from other studies supported the

observation in this study, showing relatively lower expression of Cx43 protein in D283 cells compared to other MB cell lines and glioma cell lines (Rosolen et al., 1998; Sun et al., 2012).

While the effects of this variance in Cx43 expression on MB cell behavior have not been extensively explored in the literature, insights from Rosolen et al. are informative (Sun et al., 2012). They demonstrated that treatment with dibutyryl cyclic adenosine monophosphate increased Cx43 expression in Daoy cells, thereby enhancing GJ function. Daoy cells with higher Cx43 expression required fewer transfected cells to induce significant cytotoxicity compared to the control group. This aligns with our earlier discussion in **Section 1.3.5**, which showed that Cx43-GJ channels promote the BE and increase therapeutic efficiency. These findings highlight the higher Cx43 expression observed in Med8A cells compared to D283 cells, which may explain why Med8A exhibited a quicker response to CCNU and the combination treatments described in **Section 3.5**. Notably, the relationship between Cx43 expression levels and MB patient survival remains unclear, as Cx43-GJ communication is a complex mechanism influenced by various stages of tumor differentiation (Grek et al., 2016; Krigers et al., 2023; Sin et al., 2012).

4.2. The controversy of Cx43 GJs in oncological regulation

The relationship between Cx43 and tumor cells has drawn growing attention for over a decade; however, a definitive conclusion on how Cx43 affects the proliferation, apoptosis, migration, and resistance of cancer cells has not yet been reached. The role of Cx43 in tumorigenicity or anti-tumorigenicity remains a topic of debate. Although limited research has investigated this field in MB, multiple studies have examined Cx43 in various malignant tumors.

The concept that Cx43 serves as a tumor suppressor—where higher Cx43 expression contributes to reduced tumor growth—has been suggested in several tumor types, such as breast cancer, glioma, and giant cell tumor of bone (Balla et al., 2015; Chasampalioti et al., 2019; Grek et al., 2018; Raza et al., 2017; Wu et al., 2021). However, evidence also supports the tumorigenic characteristics of Cx43, indicating that higher levels of Cx43 can promote tumor survival and migration. In our previous study, primary glioblastoma cells showed sensitization to TMZ following pharmacological inhibition of Cx43-based GJs (Potthoff et al., 2019; Schneider et al., 2021b). These findings align with studies by Murphy et al. and Munoz et al., which demonstrated that Cx43 inhibition enhanced the cytotoxicity of TMZ-resistant glioblastoma cell lines (Munoz et al., 2014; Murphy et al., 2016). Similarly, Weil et al. suggested that a Cx43-targeting strategy could reduce glioblastoma resistance to TMZ and prevent recurrence (Weil et al., 2017). Furthermore, Cx43 inhibition has been associated with the metastatic potential of breast cancer cells to healthy brain tissue (Stoletov et al., 2013).

Despite these observations, the role of Cx43 in tumorigenicity or anti-tumorigenicity remains inconclusive, with potential mechanisms proposed to explain these contradictions. For instance, Cx43 has been implicated in both positive and negative regulation of apoptosis (Sin et al., 2012). On the one hand, Cx43 expression may interfere with the activity of *Bcl-2*, an anti-apoptotic gene, where Cx43 depletion hinders cell death (Huang et al., 2001). Moreover, Cx43-based GJs can mediate the transfer of cytotoxic messengers, such as Ca^{2+}, IP3, or cAMP/cGMP, leading to cytotoxic effects. On the other hand, Cx43 has been shown to inhibit caspase-3 activation, preventing glioma cells from undergoing apoptosis (Giardina et al., 2007). Additionally, substances beneficial for survival, such as glucose and ATP, may be transported via Cx43 channels, buffering deleterious agents and alleviating cellular damage.

Beyond tumorigenicity, Cx43's involvement in metastasis has been extensively studied. Regarding cancer cell invasiveness, evidence increasingly points to a strong correlation between Cx43 expression and migration. However, it remains unclear whether Cx43-based GJs are established between the same cell types (homocellular GJs) or different cell types (heterocellular GJs) (Sin et al., 2012). One study reported that pharmacological inhibition of heterocellular GJs between astrocytes and human glioblastoma cells (GL15) impaired tumor cell motility (Oliveira et al., 2005). Other studies have supported this finding, suggesting that malignant cells rely on heterologous GJs, such as those formed with endothelial cells or astrocytes, to facilitate dissemination (Ito et al., 2000; Lin et al., 2002; McCutcheon and Spray, 2022).

Taken together, although evidence regarding Cx43's role in oncology is conflicting, it is clear that Cx43-composed GJs play a critical role in regulating cell growth, apoptosis, migration, and homeostasis. The function of Cx43 likely depends on the tumor cell's status and its interaction with surrounding benign cells.

4.3. Optimal concentration of GJ inhibitors and the effect of anti-proliferation

At beginning of this study, the optimal concentration of CCNU, MFA and TO was decided by MTT for IC50 values and BrdU assay. For CCNU, a dose- and time-dependent reduction in relative cell viability was observed in the MTT assay, with 10 μM resulting in significant cytotoxicity in flow cytometric measurements and anti-proliferative effects in the BrdU assay, as detailed in **Section 3.2, 3.3, and 3.5**. Compared to CCNU, the effect of GJ inhibitor on cellular viability and proliferation in MB cells still remains a vital issue to be addressed. In regards to MFA, 50 μM did not decrease viability except for D283 cell line at 144 hrs in MTT assay while there was no evidence could be observed to against proliferation via BrdU assay. Also, (Schneider et al., 2021a) has reported that MFA 50μM

did not notably influence cellular viability in glioblastoma cells. Previously, 50 μM of MFA has chosen and shown a demolishment of morphological and functional network architectures human glioblastoma cells. This led to a significant response to TMZ-mediated toxicity (Schneider et al., 2021a; Schneider et al., 2021b). Additionally, a study has revealed that 100 μM of MFA promoted the genes expression of stress response and antioxidant metabolism in rat H9c2 cardiac cells (Ghosh et al., 2016) also the other publication suggested that an efficient concentration of MFA was between 25 to 100 μM (Manjarrez-Marmolejo and Franco-Perez, 2016). Collectively, 50 μM of MFA was optimal concentration for this study.

In relation to TO, it was noticed that the IC50 value of Med8A at 144 hrs was out of range comparing to other conditions. This could be because TO did not exhibit a typical sigmoidal curve in the MTT assay. This atypical dose-response pattern can lead to poor fitting calculations and unreliable IC50 estimates, as shown in this case was over 500 μM. The concentration of TO was chosen not only based on the MTT results but also in conjunction with our unpublished work on human glioblastoma cell lines (data not shown, under revision). 50 μM of TO disrupted TM-based network connectivity and triggered glioblastoma cells more susceptible to cytotoxic effects of TMZ. Moreover, the results were also in line with this study, showing that 50 μM of TO inhibited the proliferation of G35 and G71 cells but did not exhibit cytotoxicity at 144 hrs. Another publication also demonstrated that TO-mediated GJ uncoupling in human cerebral microvascular endothelial cells (hCMVEC) was concentration-dependent at concentrations ≥ 50 μM but also depended on the treatment duration (Kim et al., 2017).

Regarding the anti-proliferative effect, except for 144 hrs TO treatment, MFA did not show anti-proliferative effect on MB cell lines. While (Chen et al., 2016) showed that MFA and

TO, as single treatment, could significantly reduce the proliferation of brain metastasis cells derived from breast and lung carcinomas in mouse models. In contrast, Valerie De Meulenaere et al. (2019) demonstrated that TO combined with TMZ and radiotherapy resulted in a distinct decrease in glioblastoma cell growth, but not as a single treatment (De Meulenaere et al., 2019). Opposite to this study, Venkatesch et al. presented that single MFA administration could slow down the proliferative rate of pediatric glioma xenograft (Venkatesh et al., 2019). Although multiple studies mentioned above have not always consistent findings with this study, a possible explanation may be attributed to the various tumor cell types and the dynamic of the tumor microenvironment.

4.4. Disrupting tumor cell connectivity and enhancing chemotherapy sensitivity in MB through GJ inhibitors

Current findings in oncology emphasize the role of GJ-mediated intercellular communication in tumor resistance and metastasis (Kilmister et al., 2022; Weiss et al., 2022). This study presented the first observation of MB cell lines exhibiting sensitivity to GJ inhibitors in combination with CCNU, as demonstrated by morphological alterations. Both MFA and TO significantly reduced the number of neighboring cells in Med8A populations, disrupting their spatial connectivity as evidenced by pronounced effects at 72 and 144 hrs (**Section 3.4**). Furthermore, by severing these morphological connections, the inhibitors sensitized MB cells to CCNU treatment, resulting in greater cytotoxicity than CCNU alone (**Section 3.5**). Additionally, this study demonstrates that GJs are present in MB cells, even in the absence of TM structures. These GJs were effectively disrupted by GJ blockers, highlighting their potential as therapeutic targets in MB.

While the mechanism behind the sensitizing effects of GJ inhibitors in MB cells remains to be fully elucidated, it was hypothesized that these inhibitors disrupted MB cellular

networks. Reduced cell-to-cell contact impaired intercellular communication and the transport of essential molecules (e.g., glutamate, glutathione, glucose, ATP, cAMP, IP3, and ions such as Ca^{2+}, Na^{+}, and K^{+}). This disruption potentially increased intracellular drug concentrations, leading to elevated cytotoxic effects.

GJ inhibitors may also enhance the effects of chemotherapeutic drugs by breaking the network integration of non-malignant cells, such as astrocytes, which could otherwise dilute drug concentrations. For example, Le et al. demonstrated that Cx43-mediated GJ communication in astrocytes was crucial for resistance to oxidative stress, suggesting that GJ communication buffers cytotoxicity through intercellular signaling. This buffering mechanism helped prevent cell death under oxidative stress conditions, underscoring how blocking GJs could amplify cytotoxic effects in certain therapies (Le et al., 2014). Additionally, the KO of Cx43 in primary rat brain astrocytes was reported to increase cell death induced by oxidative stress (Giardina et al., 2007). The protective role of Cx43 in cellular stress responses has also been demonstrated in osteocytes, highlighting the broader relevance of Cx43-mediated intercellular communication in mitigating cytotoxic effects across different cell types (Kar et al., 2013). Moreover, previous studies demonstrated that GJ inhibitors, including MFA and TO, effectively dismantled tumor cell networks. For example, MFA was shown to block Cx43-based GJs, significantly enhancing CCNU-mediated cytotoxicity in glioblastoma cells (Schneider et al., 2021a). Additionally, MFA disrupted the TM network supported by Cx43, reducing TM length and the number of cell connections, which sensitized glioblastoma cells to TMZ-induced cell death (Murphy et al., 2016). Similarly, TO was widely studied for its ability to inhibit Cx43 GJs. This property was explored as a promising therapeutic strategy for conditions such as migraines and epilepsy (Bialer et al., 2013; Hauge et al., 2009). Furthermore, TO disrupted GJ coupling between neurons and glial cells, highlighting its role in modulating

intercellular communication (Damodaram et al., 2009; Goadsby et al., 2009; Hauge et al., 2009).

Building on these findings, this study showed that Cx43 GJ inhibitors, such as MFA and TO, disrupted tumor networks and sensitized MB cells to chemotherapy. These inhibitors hold promise as novel therapeutic agents to enhance chemotherapy efficacy in MB patients, warranting further investigation. By severing intercellular connections, GJ inhibitors may increase intracellular drug concentrations and amplify cytotoxicity. This dual action—targeting both malignant and non-malignant cell networks—suggests that GJs could improve treatment outcomes, though further studies are needed to fully elucidate the mechanisms. The next section will explore transcriptional changes linked to this combination treatment and the molecular pathways that may underlie its enhanced therapeutic effect.

4.5. Combinatorial therapy induces transcriptional profiles of wound healing and apoptosis

Following the disruption of GJ connectivity and the increased cell death observed in the previous section, the underlying RNA-level changes after the combination treatment of CCNU and MFA in Med8A cells were explored. Given the pronounced apoptotic effects seen at 72 hrs in **Section 3.5**, we assessed the effects at 48 hrs to capture potential compensatory mechanisms induced by the combination treatment while minimizing excessive apoptosis that could obscure other molecular responses. CCNU is identified as an alkylating agent targeting the O6 position of guanine in DNA, causing mismatched repair and ultimately inducing apoptosis (Penketh et al., 2008). Compared to drugs targeting the mitotic spindle, CCNU requires extended treatment periods to achieve its full

therapeutic effect. Therefore, a 48-hour treatment period was deemed appropriate for this study.

The identified DEGs analysis (**Figure 13B** and **13E**) highlighted molecular changes in response to the combined treatment, identifying genes involved in wound healing (*ITGA10, CYTB, AQP1, COL27A1*), apoptosis (*TUBA1B, PFN1*), and tumor progression (*Rab26, MAPK8IP3*). Further investigation using GO analysis and GSEA revealed the activation of pathways predominantly linked to wound healing, with additional involvement in apoptosis. These findings suggested that the combined treatment with MFA and CCNU disrupted intercellular connections and cellular coordination, potentially triggering an acute inflammatory response resembling mechanisms involved in wound repair.

Recent studies provided insights into wound-healing-like response mechanisms in various cancers, including glioblastoma (Schneider et al., 2024; Weil et al., 2017), head and neck squamous cell carcinoma (Ekblad et al., 2013), and breast cancer (Mannino and Yarnold, 2009). Notably, one study demonstrated that after resection, glioblastoma cells extended and migrated their TMs to the injured site to rebuild the tumor network . Collectively, the findings of this thesis aligned with this study (Weil et al., 2017).

From the DEGs analysis, several genes were identified as regulators of tumor proliferation across various tumor types. For instance, *ITGA10* is highly expressed in high-grade gliomas and malignant melanoma cells, where it supported cell migration and viability (Masoumi et al., 2021; Munksgaard Thoren et al., 2019). Inhibition of *ITGA10* was shown to impair proliferation and migration of patient-derived glioblastoma cells and restrict tumor growth in a xenograft animal model (Masoumi et al., 2021). The present study suggested that after tumor network breakdown caused by the combined treatment, Med8A cells entered the proliferation phase of the wound-healing process. This was supported by the enhanced expression of *CYTB*, *CYB561*, and *PLC-β2*. The upregulation of *CYTB* and

PLC-β2 was associated with the promotion of proliferation in HER2-positive breast cancer cells (Zhao et al., 2024) and primary breast tumor cells (Bertagnolo et al., 2007; Bertagnolo et al., 2006). Additionally, the overexpression of *CYB561* was linked to increased growth and progression in bladder cancer cells (Dasgupta et al., 2008, 2009). Another activated gene, *COL27A1*, encodes type XXVII collagen, a key component of the ECM (Hu et al., 2022). Given the ECM's fundamental role in tissue remodeling, the induction of *COL27A1* aligns with the processes expected during wound healing (Diller and Tabor, 2022).

The downregulation of *TUBA1B* and *PFN1* were associated with the initiation of apoptosis, as demonstrated in studies of other tumor types. For instance, the deletion of *TUBA1B* increased breast cancer cell death *in vitro* (Wang et al., 2024). Similarly, *PFN1* depletion accelerated DNA damage-induced apoptosis in an immortalized human keratinocyte cell line (Lee et al., 2021). These findings were consistent with flow cytometric results showing cellular damage following MFA and CCNU-mediated cytotoxicity.

Interestingly, this study observed that Med8A cells exhibited lower toxicity to combination chemotherapy at 144 hrs compared to 72 hrs, as shown in **Section 3.5**. In this context, molecular profiling further revealed that this reduced toxicity was associated with an inflammatory response to chemotherapy-induced damage, which promoted cellular proliferation and repair. Consequently, this mechanism may have enhanced Med8A cells' resilience against chemotherapy-induced cell death at 144 hrs.

Further functional exploration through GSEA and GO analysis supported that wound-healing and apoptotic processes were induced after CCNU with MFA treatment (**Figure 13C and 13D**). Wound healing comprises four phases: hemostasis, inflammation, regeneration, and remodeling (Deyell et al., 2021). During the intermediate stage, cells exhibite behaviors such as proliferation, migration, and invasion to the injury site to replace

missing cells (White et al., 2023). This was strongly associated with key biological processes (BPs) identified in GO analysis, including syncytium formation, ECM structure organization, regulation of response to wounding, and blood vessel development, all crucial for facilitating wound closure (White et al., 2023; Xue and Jackson, 2015). Regulation of cell motility and migration, along with blood vessel development, are also involved in the remodeling phase (Li et al., 2013; Pettet et al., 1996). Notably, the most suppressed BP, rRNA processing, was shown to induce apoptosis or cell cycle arrest in response to stress (Hayashi et al., 2014; Turi et al., 2019). Similarly, downregulation of mitochondrial translation and the assembly of ribonucleoprotein complexes could trigger apoptotic responses (Jeon et al., 2022; Takeuchi and Ueda, 2003). Additionally, the upregulated pathways identified through GSEA were strongly linked to the wound healing process. Cellular response to growth factor stimuli and angiogenesis were involved in proliferation, while activation of the ERK1 and ERK2 cascades was pivotal for cellular migration and proliferation during the wound-recovery phase (Fernandez-Guarino et al., 2023; Lee et al., 2018; Molina and Adjei, 2006).

This study was the first to provide evidence of the transcriptional profiling of Med8A cells following treatment with MFA and CCNU. The findings revealed that after Cx43-based GJs were inhibited by MFA, but before massive cell death was induced by the combined treatment, wound healing mechanisms were predominantly activated in Med8A cells as a compensatory response. This observation suggests that tumor cells-initiated repair processes to rebuild tumor networks, as described by Weil et al. in their study (Weil et al., 2017). These findings highlighted the complex interplay between wound healing, apoptosis, and tumor progression pathways in response to the combined treatment, emphasizing the dynamic nature of cellular responses and their potential implications for treatment outcomes in MBs.

4.6. Cx43 deprivation confirms the effect of GJ inhibitors and the role of Cx43 in MB cells

Although multiple studies have suggested that Cx43 plays a vital role in cellular communication, this study also demonstrated that a Cx43 GJ-targeted therapeutic approach could enhance CCNU-induced antitumoral effects in both MB cell lines. It remained to be confirmed whether Cx43 was the primary target, apart from other connexin members, and whether the pharmacological GJ inhibitors (MFA and TO) primarily exerted their function through connexin inhibition. Therefore, a #KO2 as the Cx43 KO clone was established from Med8A via CRISPR/Cas9 transfection to investigate this question. The findings of this study first validated total deprivation of Cx43 in #KO2 via IF staining and WB. Subsequently, the Med8A #KO2 clone exhibited a noticeable reduction in cellular neighborhoods for the majority of the population compared to ZsG Med8A cells at 72 hrs. Furthermore, at 144 hrs, it showed a significantly lower average number of adjacent cells, as discussed in **Section 3.8**. The loss of cell-to-cell connection led to higher spontaneous cell death and increased CCNU cytotoxicity compared to the #C2 population when pharmacological inhibition was applied. The aforementioned data confirmed that the results for Med8A cells, as presented in **Sections 3.4 and 3.5**, were Cx43-dependent. Additionally, it was microscopically observed that the #KO2 clone had more isolated clusters than the #C2 clone, ZsG Med8A, and wild-type Med8A during in vitro culture. This phenomenon was accompanied by a slower growth rate and higher spontaneous cell death, as reflected in the flow cytometry results. This evidence supports the theory that Cx43-composed GJs facilitate the transport of beneficial substances and signaling exchanges between cells. The depletion of Cx43 impeded Med8A cell growth and rendered the cells more vulnerable, leading to an increase in spontaneous cell death. This

vulnerability likely explains the more pronounced increase in cell death rates observed in #KO2 cells after CCNU administration compared to #C2 cells. Moreover, the greater effect in #KO2 cells could be attributed to the complete loss of Cx43 due to the KO. In contrast, MFA and TO treatments likely do not achieve complete inhibition of Cx43-based GJs, which may account for the less pronounced effects observed with these pharmacological inhibitors. A similar result was observed in a Cx43 KO clone derived from the G35 cell line in our group, and a study by Bobbie et al. reported a greater apoptotic rate of retinal vascular cells in Cx43-reduced mice compared to control mice (Bobbie et al., 2010). In contrast, Vinken et al. showed that silencing Cx43 in primary rat hepatocytes led to decreased spontaneous apoptosis in culture (Vinken et al., 2012). This is also supported by a demonstration of renoprotection with Cx43 depletion in renal tubular epithelial cells (Xu et al., 2022). Diminishment of Cx43 protein has been noted to interrupt cellular adhesion, motility, and polarity (Matsuuchi and Naus, 2013). Therefore, it is possible that #KO2 had difficulty adhering, resulting in fewer cells and greater vulnerability, despite the same seeding number and incubation time compared to #C2.

Besides, Cx43 deprivation may have also led to dynamic changes in cell morphology and rearrangement of cytoskeletons. In this study, depletion of Cx43 not only caused morphological changes in Med8A but also in other types of tumors. Our previous work revealed that glioblastoma cells with Cx43 KO showed a significant reduction in TM length and interfered with the transfer of intercellular calcein dye. Moreover, one report indicated that Cx43 KO breast cancer cells exhibited a distinct decrease in the number and length of tunneling nanotubes (Tishchenko et al., 2020). Apart from morphological disruption, these cellular alterations also involved the orientation of locomotion for seeking cell-to-cell contacts. Therefore, a lack of Cx43 could impede cell polarity and intercellular signaling communication. Weil et al. demonstrated that poorly TM-connected gliomas had a better

therapeutic effect of TMZ (Weil et al., 2017). Consequently, this caused #KO2 cells to form more isolated clusters and have fewer neighboring cells than the ZsG Med8A population, without any treatment. Moreover, the lack of cell-to-cell transport of second messengers and survival molecules via Cx43 GJs led to #KO2 exhibiting greater CCNU-induced cell death compared to #C2, as expected.

5. Summary

The discovery of communicative cellular networks has reshaped our understanding of brain tumor biology. Despite the growing knowledge of Cx43-based GJ as key drivers of malignant intercellular connectivity in several malignant brain tumors, the significance of GJ in MB remains largely unknown. This thesis investigates whether MB harbors tumor networks mediated by Cx43-based GJs and explores their functional role.

Using IF and WB, Cx43-based GJ expression was confirmed in non-WNT/non-SHH MB cell lines (Med8A and D283). MFA and TO were used as clinically-feasible pharmacological GJ-blockers. MFA and TO demonstrated reduced intercellular connectivity pharmacologically thus enhanced sensitivity to CCNU-mediated cytotoxicity, as shown through real-time imaging and flow cytometry. RNA sequencing revealed that the combination of MFA and CCNU disrupted cellular homeostasis by activating wound-healing mechanisms in Med8A cells.

A Cx43 KO model, generated using CRISPR/Cas9, confirmed the pivotal role of Cx43 in maintaining intercellular connectivity and the pharmacological inhibition from MFA and TO. The absence of Cx43 resulted in fewer neighboring connections in Med8A cells, making them more vulnerable to CCNU treatment.

These findings suggest that Cx43-based GJs contribute to MB tumor networks and may play a key role in mediating resistance to chemotherapy. Targeting these networks pharmacologically offers a potential strategy to enhance the efficacy of chemotherapeutic agents like CCNU in MBs.

6. List of figures

7. List of tables

8. References

Albers, J., Danzer, C., Rechsteiner, M., Lehmann, H., Brandt, L.P., Hejhal, T., Catalano, A., Busenhart, P., Goncalves, A.F., Brandt, S., Bode, P.K., Bode-Lesniewska, B., Wild, P.J., and Frew, I.J. A versatile modular vector system for rapid combinatorial mammalian genetics. J Clin Invest, 2015. *125*, 1603-1619.

An, L., Yu, R., Han, Y., and Zhou, Z. Decoding the intercellular communication network during tumorigenesis. Cancer Biol Med, 2021. *19*, 265-272.

Anders, S., and Huber, W. Differential expression analysis for sequence count data. Genome Biol, 2010. *11*, R106.

Aref, D., and Croul, S. Medulloblastoma: recurrence and metastasis. CNS Oncol, 2013. *2*, 377-385.

Baer, J.C., Freeman, A.A., Newlands, E.S., Watson, A.J., Rafferty, J.A., and Margison, G.P. Depletion of O6-alkylguanine-DNA alkyltransferase correlates with potentiation of temozolomide and CCNU toxicity in human tumour cells. Br J Cancer, 1993. *67*, 1299-1302.

Bakalova, R., Semkova, S., Ivanova, D., Zhelev, Z., Miller, T., Takeshima, T., Shibata, S., Lazarova, D., Aoki, I., and Higashi, T. Selective Targeting of Cancerous Mitochondria and Suppression of Tumor Growth Using Redox-Active Treatment Adjuvant. Oxid Med Cell Longev, 2020. *2020*, 6212935.

Balla, P., Maros, M.E., Barna, G., Antal, I., Papp, G., Sapi, Z., Athanasou, N.A., Benassi, M.S., Picci, P., and Krenacs, T. Prognostic impact of reduced connexin43 expression and gap junction coupling of neoplastic stromal cells in giant cell tumor of bone. PLoS One, 2015. *10*, e0125316.

Bandopadhayay, P., Bergthold, G., Nguyen, B., Schubert, S., Gholamin, S., Tang, Y., Bolin, S., Schumacher, S.E., Zeid, R., Masoud, S., Yu, F., Vue, N., Gibson, W.J., Paolella, B.R., Mitra, S.S., Cheshier, S.H., Qi, J., Liu, K.W., Wechsler-Reya, R., Weiss, W.A., Swartling, F.J., Kieran, M.W., Bradner, J.E., Beroukhim, R., and Cho, Y.J. BET bromodomain inhibition of MYC-amplified medulloblastoma. Clin Cancer Res, 2014. *20*, 912-925.

Bannwarth, B., Netter, P., Pourel, J., Royer, R.J., and Gaucher, A. Clinical pharmacokinetics of nonsteroidal anti-inflammatory drugs in the cerebrospinal fluid. Biomed Pharmacother, 1989. *43*, 121-126.

Baryawno, N., Rahbar, A., Wolmer-Solberg, N., Taher, C., Odeberg, J., Darabi, A., Khan, Z., Sveinbjornsson, B., FuskevAg, O.M., Segerstrom, L., Nordenskjold, M., Siesjo, P., Kogner, P., Johnsen, J.I., and Soderberg-Naucler, C. Detection of human

cytomegalovirus in medulloblastomas reveals a potential therapeutic target. J Clin Invest, 2011. *121*, 4043-4055.
Bautista, F., Fioravantti, V., de Rojas, T., Carceller, F., Madero, L., Lassaletta, A., and Moreno, L. Medulloblastoma in children and adolescents: a systematic review of contemporary phase I and II clinical trials and biology update. Cancer Med, 2017. *6*, 2606-2624.
Bertagnolo, V., Benedusi, M., Brugnoli, F., Lanuti, P., Marchisio, M., Querzoli, P., and Capitani, S. Phospholipase C-beta 2 promotes mitosis and migration of human breast cancer-derived cells. Carcinogenesis, 2007. *28*, 1638-1645.
Bertagnolo, V., Benedusi, M., Querzoli, P., Pedriali, M., Magri, E., Brugnoli, F., and Capitani, S. PLC-beta2 is highly expressed in breast cancer and is associated with a poor outcome: a study on tissue microarrays. Int J Oncol, 2006. *28*, 863-872.
Beyer, E.C., and Berthoud, V.M. Gap junction gene and protein families: Connexins, innexins, and pannexins. Biochim Biophys Acta Biomembr, 2018. *1860*, 5-8.
Beyer, E.C., Paul, D.L., and Goodenough, D.A. Connexin43: a protein from rat heart homologous to a gap junction protein from liver. J Cell Biol, 1987. *105*, 2621-2629.
Bialer, M., Johannessen, S.I., Levy, R.H., Perucca, E., Tomson, T., and White, H.S. Progress report on new antiepileptic drugs: a summary of the Eleventh Eilat Conference (EILAT XI). Epilepsy Res, 2013. *103*, 2-30.
Bobbie, M.W., Roy, S., Trudeau, K., Munger, S.J., Simon, A.M., and Roy, S. Reduced connexin 43 expression and its effect on the development of vascular lesions in retinas of diabetic mice. Invest Ophthalmol Vis Sci, 2010. *51*, 3758-3763.
Bonifazi, P., Goldin, M., Picardo, M.A., Jorquera, I., Cattani, A., Bianconi, G., Represa, A., Ben-Ari, Y., and Cossart, R. GABAergic hub neurons orchestrate synchrony in developing hippocampal networks. Science, 2009. *326*, 1419-1424.
Brasme, J.F., Chalumeau, M., Doz, F., Lacour, B., Valteau-Couanet, D., Gaillard, S., Delalande, O., Aghakhani, N., Sainte-Rose, C., Puget, S., and Grill, J. Interval between onset of symptoms and diagnosis of medulloblastoma in children: distribution and determinants in a population-based study. Eur J Pediatr, 2012. *171*, 25-32.
Brown, H.G., Kepner, J.L., Perlman, E.J., Friedman, H.S., Strother, D.R., Duffner, P.K., Kun, L.E., Goldthwaite, P.T., and Burger, P.C. "Large cell/anaplastic" medulloblastomas: a Pediatric Oncology Group Study. J Neuropathol Exp Neurol, 2000. *59*, 857-865.
Bundscherer, A.C., Malsy, M., Bitzinger, D.I., Wiese, C.H., Gruber, M.A., and Graf, B.M. Effects of Lidocaine on HT-29 and SW480 Colon Cancer Cells In Vitro. Anticancer Res, 2017. *37*, 1941-1945.
Bunin, G.R., Kushi, L.H., Gallagher, P.R., Rorke-Adams, L.B., McBride, M.L., and Cnaan, A. Maternal diet during pregnancy and its association with medulloblastoma in

children: a children's oncology group study (United States). Cancer Causes Control, 2005. *16*, 877-891.
Cavalli, F.M.G., Remke, M., Rampasek, L., Peacock, J., Shih, D.J.H., Luu, B., Garzia, L., Torchia, J., Nor, C., Morrissy, A.S., Agnihotri, S., Thompson, Y.Y., Kuzan-Fischer, C.M., Farooq, H., Isaev, K., Daniels, C., Cho, B.K., Kim, S.K., Wang, K.C., Lee, J.Y., Grajkowska, W.A., Perek-Polnik, M., Vasiljevic, A., Faure-Conter, C., Jouvet, A., Giannini, C., Nageswara Rao, A.A., Li, K.K.W., Ng, H.K., Eberhart, C.G., Pollack, I.F., Hamilton, R.L., Gillespie, G.Y., Olson, J.M., Leary, S., Weiss, W.A., Lach, B., Chambless, L.B., Thompson, R.C., Cooper, M.K., Vibhakar, R., Hauser, P., van Veelen, M.C., Kros, J.M., French, P.J., Ra, Y.S., Kumabe, T., Lopez-Aguilar, E., Zitterbart, K., Sterba, J.*, et al.* Intertumoral Heterogeneity within Medulloblastoma Subgroups. Cancer Cell, 2017. *31*, 737-754 e736.
Chasampalioti, M., Green, A.R., Ellis, I.O., Rakha, E.A., Jackson, A.M., Spendlove, I., and Ramage, J.M. Connexin 43 is an independent predictor of patient outcome in breast cancer patients. Breast Cancer Res Treat, 2019. *174*, 93-102.
Chen, Q., Boire, A., Jin, X., Valiente, M., Er, E.E., Lopez-Soto, A., Jacob, L., Patwa, R., Shah, H., Xu, K., Cross, J.R., and Massague, J. Carcinoma-astrocyte gap junctions promote brain metastasis by cGAMP transfer. Nature, 2016. *533*, 493-498.
Chen, X., Chen, L., Kurten, C.H.L., Jabbari, F., Vujanovic, L., Ding, Y., Lu, B., Lu, K., Kulkarni, A., Tabib, T., Lafyatis, R., Cooper, G.F., Ferris, R., and Lu, X. An individualized causal framework for learning intercellular communication networks that define microenvironments of individual tumors. PLoS Comput Biol, 2022. *18*, e1010761.
Chen, Z., Yang, H., Wang, J., Long, G., Xi, Q., Chen, T., He, Y., Zhang, B., and Wan, F. Molecular characterization of sub-frontal recurrent medulloblastomas reveals potential clinical relevance. Front Neurol, 2023. *14*, 1148848.
Choi, J.Y. Medulloblastoma: Current Perspectives and Recent Advances. Brain Tumor Res Treat, 2023. *11*, 28-38.
Clifford, S.C., Lusher, M.E., Lindsey, J.C., Langdon, J.A., Gilbertson, R.J., Straughton, D., and Ellison, D.W. Wnt/Wingless pathway activation and chromosome 6 loss characterize a distinct molecular sub-group of medulloblastomas associated with a favorable prognosis. Cell Cycle, 2006. *5*, 2666-2670.
Contreras, J.E., Sanchez, H.A., Veliz, L.P., Bukauskas, F.F., Bennett, M.V., and Saez, J.C. Role of connexin-based gap junction channels and hemichannels in ischemia-induced cell death in nervous tissue. Brain Res Brain Res Rev, 2004. *47*, 290-303.
Cotter, J.A., and Hawkins, C. Medulloblastoma: WHO 2021 and Beyond. Pediatr Dev Pathol, 2022. *25*, 23-33.

Damodaram, S., Thalakoti, S., Freeman, S.E., Garrett, F.G., and Durham, P.L. Tonabersat inhibits trigeminal ganglion neuronal-satellite glial cell signaling. Headache, 2009. *49*, 5-20.
Dasgupta, S., Hoque, M.O., Upadhyay, S., and Sidransky, D. Mitochondrial cytochrome B gene mutation promotes tumor growth in bladder cancer. Cancer Res, 2008. *68*, 700-706.
Dasgupta, S., Hoque, M.O., Upadhyay, S., and Sidransky, D. Forced cytochrome B gene mutation expression induces mitochondrial proliferation and prevents apoptosis in human uroepithelial SV-HUC-1 cells. Int J Cancer, 2009. *125*, 2829-2835.
Davidson, J.S., Baumgarten, I.M., and Harley, E.H. Reversible inhibition of intercellular junctional communication by glycyrrhetinic acid. Biochem Biophys Res Commun, 1986. *134*, 29-36.
De Meulenaere, V., Bonte, E., Verhoeven, J., Kalala Okito, J.P., Pieters, L., Vral, A., De Wever, O., Leybaert, L., Goethals, I., Vanhove, C., Descamps, B., and Deblaere, K. Adjuvant therapeutic potential of tonabersat in the standard treatment of glioblastoma: A preclinical F98 glioblastoma rat model study. PLoS One, 2019. *14*, e0224130.
Delmar, M., Laird, D.W., Naus, C.C., Nielsen, M.S., Verselis, V.K., and White, T.W. Connexins and Disease. Cold Spring Harb Perspect Biol, 2018. *10*.
Desir, S., Wong, P., Turbyville, T., Chen, D., Shetty, M., Clark, C., Zhai, E., Romin, Y., Manova-Todorova, K., Starr, T.K., Nissley, D.V., Steer, C.J., Subramanian, S., and Lou, E. Intercellular Transfer of Oncogenic KRAS via Tunneling Nanotubes Introduces Intracellular Mutational Heterogeneity in Colon Cancer Cells. Cancers, 2019. *11*.
Deyell, M., Garris, C.S., and Laughney, A.M. Cancer metastasis as a non-healing wound. Br J Cancer, 2021. *124*, 1491-1502.
Diller, R.B., and Tabor, A.J. The Role of the Extracellular Matrix (ECM) in Wound Healing: A Review. Biomimetics (Basel), 2022. *7*.
Dominiak, A., Chelstowska, B., Olejarz, W., and Nowicka, G. Communication in the Cancer Microenvironment as a Target for Therapeutic Interventions. Cancers (Basel), 2020. *12*.
Douw, L., Schoonheim, M.M., Landi, D., van der Meer, M.L., Geurts, J.J., Reijneveld, J.C., Klein, M., and Stam, C.J. Cognition is related to resting-state small-world network topology: an magnetoencephalographic study. Neuroscience, 2011. *175*, 169-177.
Durham, P.L., and Garrett, F.G. Neurological mechanisms of migraine: potential of the gap-junction modulator tonabersat in prevention of migraine. Cephalalgia, 2009. *29 Suppl 2*, 1-6.

Ekblad, L., Lindgren, G., Persson, E., Kjellen, E., and Wennerberg, J. Cell-line-specific stimulation of tumor cell aggressiveness by wound healing factors - a central role for STAT3. BMC Cancer, 2013. *13*, 33.
Elzarrad, M.K., Haroon, A., Willecke, K., Dobrowolski, R., Gillespie, M.N., and Al-Mehdi, A.B. Connexin-43 upregulation in micrometastases and tumor vasculature and its role in tumor cell attachment to pulmonary endothelium. BMC Med, 2008. *6*, 20.
Eran, A., Ozturk, A., Aygun, N., and Izbudak, I. Medulloblastoma: atypical CT and MRI findings in children. Pediatr Radiol, 2010. *40*, 1254-1262.
Fang, F.Y., Rosenblum, J.S., Ho, W.S., and Heiss, J.D. New Developments in the Pathogenesis, Therapeutic Targeting, and Treatment of Pediatric Medulloblastoma. Cancers (Basel), 2022. *14*.
Fernandez-Guarino, M., Hernandez-Bule, M.L., and Bacci, S. Cellular and Molecular Processes in Wound Healing. Biomedicines, 2023. *11*.
Franceschi, E., Hofer, S., Brandes, A.A., Frappaz, D., Kortmann, R.D., Bromberg, J., Dangouloff-Ros, V., Boddaert, N., Hattingen, E., Wiestler, B., Clifford, S.C., Figarella-Branger, D., Giangaspero, F., Haberler, C., Pietsch, T., Pajtler, K.W., Pfister, S.M., Guzman, R., Stummer, W., Combs, S.E., Seidel, C., Beier, D., McCabe, M.G., Grotzer, M., Laigle-Donadey, F., Stucklin, A.S.G., Idbaih, A., Preusser, M., van den Bent, M., Weller, M., and Hau, P. EANO-EURACAN clinical practice guideline for diagnosis, treatment, and follow-up of post-pubertal and adult patients with medulloblastoma. Lancet Oncol, 2019. *20*, e715-e728.
Funakoshi, Y., Sugihara, Y., Uneda, A., Nakashima, T., and Suzuki, H. Recent advances in the molecular understanding of medulloblastoma. Cancer Sci, 2023. *114*, 741-749.
Geris, J.M., and Spector, L.G. Race, ethnicity, and socioeconomic differences in incidence of pediatric embryonal tumors in the United States. Pediatr Blood Cancer, 2020. *67*, e28582.
Ghasemi, D.R., Fleischhack, G., Milde, T., and Pajtler, K.W. The Current Landscape of Targeted Clinical Trials in Non-WNT/Non-SHH Medulloblastoma. Cancers (Basel), 2022. *14*.
Ghosh, R., Hwang, S.M., Cui, Z., Gilda, J.E., and Gomes, A.V. Different effects of the nonsteroidal anti-inflammatory drugs meclofenamate sodium and naproxen sodium on proteasome activity in cardiac cells. J Mol Cell Cardiol, 2016. *94*, 131-144.
Giardina, S.F., Mikami, M., Goubaeva, F., and Yang, J. Connexin 43 confers resistance to hydrogen peroxide-mediated apoptosis. Biochem Biophys Res Commun, 2007. *362*, 747-752.

Goadsby, P.J., Ferrari, M.D., Csanyi, A., Olesen, J., Mills, J.G., and Tonabersat, T.O.N.S.G. Randomized, double-blind, placebo-controlled, proof-of-concept study of the cortical spreading depression inhibiting agent tonabersat in migraine prophylaxis. Cephalalgia, 2009. *29*, 742-750.
Goodenough, D.A. Bulk isolation of mouse hepatocyte gap junctions. Characterization of the principal protein, connexin. J Cell Biol, 1974. *61*, 557-563.
Goodenough, D.A., and Stoeckenius, W. The isolation of mouse hepatocyte gap junctions. Preliminary chemical characterization and x-ray diffraction. J Cell Biol, 1972. *54*, 646-656.
Goschzik, T., Schwalbe, E.C., Hicks, D., Smith, A., Zur Muehlen, A., Figarella-Branger, D., Doz, F., Rutkowski, S., Lannering, B., Pietsch, T., and Clifford, S.C. Prognostic effect of whole chromosomal aberration signatures in standard-risk, non-WNT/non-SHH medulloblastoma: a retrospective, molecular analysis of the HIT-SIOP PNET 4 trial. Lancet Oncol, 2018. *19*, 1602-1616.
Grek, C.L., Rhett, J.M., Bruce, J.S., Ghatnekar, G.S., and Yeh, E.S. Connexin 43, breast cancer tumor suppressor: Missed connections? Cancer Lett, 2016. *374*, 117-126.
Grek, C.L., Sheng, Z., Naus, C.C., Sin, W.C., Gourdie, R.G., and Ghatnekar, G.G. Novel approach to temozolomide resistance in malignant glioma: connexin43-directed therapeutics. Curr Opin Pharmacol, 2018. *41*, 79-88.
Guido, C., Baldari, C., Maiorano, G., Mastronuzzi, A., Carai, A., Quintarelli, C., De Angelis, B., Cortese, B., Gigli, G., and Palama, I.E. Nanoparticles for Diagnosis and Target Therapy in Pediatric Brain Cancers. Diagnostics (Basel), 2022. *12*.
Hauge, A.W., Asghar, M.S., Schytz, H.W., Christensen, K., and Olesen, J. Effects of tonabersat on migraine with aura: a randomised, double-blind, placebo-controlled crossover study. Lancet Neurol, 2009. *8*, 718-723.
Hayashi, Y., Kuroda, T., Kishimoto, H., Wang, C., Iwama, A., and Kimura, K. Downregulation of rRNA transcription triggers cell differentiation. PLoS One, 2014. *9*, e98586.
Hong, X., Sin, W.C., Harris, A.L., and Naus, C.C. Gap junctions modulate glioma invasion by direct transfer of microRNA. Oncotarget, 2015. *6*, 15566-15577.
Hu, Y., Chen, I.P., de Almeida, S., Tiziani, V., Do Amaral, C.M., Gowrishankar, K., Passos-Bueno, M.R., and Reichenberger, E.J. A novel autosomal recessive GJA1 missense mutation linked to Craniometaphyseal dysplasia. PLoS One, 2013. *8*, e73576.
Hu, Z., Xu, Y., Li, J., Zhu, Z., Qiu, Y., and Liu, Z. Bioinformatics Analysis and Experimental Verification Identify Downregulation of COL27A1 in Poor Segmental Congenital Scoliosis. Comput Math Methods Med, 2022. *2022*, 2616827.

Huang, R., Liu, Y.G., Lin, Y., Fan, Y., Boynton, A., Yang, D., and Huang, R.P. Enhanced apoptosis under low serum conditions in human glioblastoma cells by connexin 43 (Cx43). Mol Carcinog, 2001. *32*, 128-138.
Ito, A., Katoh, F., Kataoka, T.R., Okada, M., Tsubota, N., Asada, H., Yoshikawa, K., Maeda, S., Kitamura, Y., Yamasaki, H., and Nojima, H. A role for heterologous gap junctions between melanoma and endothelial cells in metastasis. J Clin Invest, 2000. *105*, 1189-1197.
Ivanov, D.P., Coyle, B., Walker, D.A., and Grabowska, A.M. In vitro models of medulloblastoma: Choosing the right tool for the job. J Biotechnol, 2016. *236*, 10-25.
Jeon, P., Ham, H.J., Park, S., and Lee, J.A. Regulation of Cellular Ribonucleoprotein Granules: From Assembly to Degradation via Post-translational Modification. Cells, 2022. *11*.
Juraschka, K., and Taylor, M.D. Medulloblastoma in the age of molecular subgroups: a review. J Neurosurg Pediatr, 2019. *24*, 353-363.
Kanaporis, G., Brink, P.R., and Valiunas, V. Gap junction permeability: selectivity for anionic and cationic probes. Am J Physiol Cell Physiol, 2011. *300*, C600-609.
Kandouz, M., and Batist, G. Gap junctions and connexins as therapeutic targets in cancer. Expert Opin Ther Targets, 2010. *14*, 681-692.
Kar, R., Riquelme, M.A., Werner, S., and Jiang, J.X. Connexin 43 channels protect osteocytes against oxidative stress-induced cell death. J Bone Miner Res, 2013. *28*, 1611-1621.
Khanna, V., Achey, R.L., Ostrom, Q.T., Block-Beach, H., Kruchko, C., Barnholtz-Sloan, J.S., and de Blank, P.M. Incidence and survival trends for medulloblastomas in the United States from 2001 to 2013. J Neurooncol, 2017. *135*, 433-441.
Kilmister, E.J., Koh, S.P., Weth, F.R., Gray, C., and Tan, S.T. Cancer Metastasis and Treatment Resistance: Mechanistic Insights and Therapeutic Targeting of Cancer Stem Cells and the Tumor Microenvironment. Biomedicines, 2022. *10*.
Kim, Y., Griffin, J.M., Nor, M.N.M., Zhang, J., Freestone, P.S., Danesh-Meyer, H.V., Rupenthal, I.D., Acosta, M., Nicholson, L.F.B., O'Carroll, S.J., and Green, C.R. Tonabersat Prevents Inflammatory Damage in the Central Nervous System by Blocking Connexin43 Hemichannels. Neurotherapeutics, 2017. *14*, 1148-1165.
Kocakaya, S., Beier, C.P., and Beier, D. Chemotherapy increases long-term survival in patients with adult medulloblastoma--a literature-based meta-analysis. Neuro Oncol, 2016. *18*, 408-416.
Kool, M., Korshunov, A., Remke, M., Jones, D.T., Schlanstein, M., Northcott, P.A., Cho, Y.J., Koster, J., Schouten-van Meeteren, A., van Vuurden, D., Clifford, S.C., Pietsch, T., von Bueren, A.O., Rutkowski, S., McCabe, M., Collins, V.P., Backlund, M.L., Haberler,

C., Bourdeaut, F., Delattre, O., Doz, F., Ellison, D.W., Gilbertson, R.J., Pomeroy, S.L., Taylor, M.D., Lichter, P., and Pfister, S.M. Molecular subgroups of medulloblastoma: an international meta-analysis of transcriptome, genetic aberrations, and clinical data of WNT, SHH, Group 3, and Group 4 medulloblastomas. Acta Neuropathol, 2012. *123*, 473-484.

Krigers, A., Demetz, M., Moser, P., Kerschbaumer, J., Brawanski, K.R., Fritsch, H., Thome, C., and Freyschlag, C.F. Impact of GAP-43, Cx43 and actin expression on the outcome and overall survival in diffuse and anaplastic gliomas. Sci Rep, 2023. *13*, 2024.

Krynska, B., Del Valle, L., Croul, S., Gordon, J., Katsetos, C.D., Carbone, M., Giordano, A., and Khalili, K. Detection of human neurotropic JC virus DNA sequence and expression of the viral oncogenic protein in pediatric medulloblastomas. Proc Natl Acad Sci U S A, 1999. *96*, 11519-11524.

Kumar, R., Liu, A.P.Y., and Northcott, P.A. Medulloblastoma genomics in the modern molecular era. Brain Pathol, 2020. *30*, 679-690.

Kurdi, M., Mulla, N., Malibary, H., Bamaga, A.K., Fadul, M.M., Faizo, E., Hakamy, S., and Baeesa, S. Immune microenvironment of medulloblastoma: The association between its molecular subgroups and potential targeted immunotherapeutic receptors. World J Clin Oncol, 2023. *14*, 117-130.

Laird, D.W., and Lampe, P.D. Therapeutic strategies targeting connexins. Nat Rev Drug Discov, 2018. *17*, 905-921.

Latario, C.J., Schoenfeld, L.W., Howarth, C.L., Pickrell, L.E., Begum, F., Fischer, D.A., Grbovic-Huezo, O., Leach, S.D., Sanchez, Y., Smith, K.D., and Higgs, H.N. Tumor microtubes connect pancreatic cancer cells in an Arp2/3 complex-dependent manner. Mol Biol Cell, 2020. *31*, 1259-1272.

Le, H.T., Sin, W.C., Lozinsky, S., Bechberger, J., Vega, J.L., Guo, X.Q., Saez, J.C., and Naus, C.C. Gap junction intercellular communication mediated by connexin43 in astrocytes is essential for their resistance to oxidative stress. J Biol Chem, 2014. *289*, 1345-1354.

Lee, C., Rudneva, V.A., Erkek, S., Zapatka, M., Chau, L.Q., Tacheva-Grigorova, S.K., Garancher, A., Rusert, J.M., Aksoy, O., Lea, R., Mohammad, H.P., Wang, J., Weiss, W.A., Grimes, H.L., Pfister, S.M., Northcott, P.A., and Wechsler-Reya, R.J. Lsd1 as a therapeutic target in Gfi1-activated medulloblastoma. Nat Commun, 2019. *10*, 332.

Lee, C.J., Yoon, M.J., Kim, D.H., Kim, T.U., and Kang, Y.J. Profilin-1; a novel regulator of DNA damage response and repair machinery in keratinocytes. Mol Biol Rep, 2021. *48*, 1439-1452.

Lee, S., Kim, M.S., Jung, S.J., Kim, D., Park, H.J., and Cho, D. ERK activating peptide, AES16-2M promotes wound healing through accelerating migration of keratinocytes. Sci Rep, 2018. *8*, 14398.
Leithe, E., Mesnil, M., and Aasen, T. The connexin 43 C-terminus: A tail of many tales. Biochim Biophys Acta Biomembr, 2018. *1860*, 48-64.
Leshchenko, Y., Likhodii, S., Yue, W., Burnham, W.M., and Perez Velazquez, J.L. Carbenoxolone does not cross the blood brain barrier: an HPLC study. BMC Neurosci, 2006. *7*, 3.
Leybaert, L., Lampe, P.D., Dhein, S., Kwak, B.R., Ferdinandy, P., Beyer, E.C., Laird, D.W., Naus, C.C., Green, C.R., and Schulz, R. Connexins in Cardiovascular and Neurovascular Health and Disease: Pharmacological Implications. Pharmacol Rev, 2017. *69*, 396-478.
Li, L., He, Y., Zhao, M., and Jiang, J. Collective cell migration: Implications for wound healing and cancer invasion. Burns Trauma, 2013. *1*, 21-26.
Li, S., Gao, Y., Pu, K., Ma, L., Song, X., and Liu, Y. All-trans retinoic acid enhances bystander effect of suicide-gene therapy against medulloblastomas. Neurosci Lett, 2011. *503*, 115-119.
Liang, Z., Wang, X., Hao, Y., Qiu, L., Lou, Y., Zhang, Y., Ma, D., and Feng, J. The Multifaceted Role of Astrocyte Connexin 43 in Ischemic Stroke Through Forming Hemichannels and Gap Junctions. Front Neurol, 2020. *11*, 703.
Liao, Y., Smyth, G.K., and Shi, W. The R package Rsubread is easier, faster, cheaper and better for alignment and quantification of RNA sequencing reads. Nucleic Acids Res, 2019. *47*, e47.
Lin, J.H., Takano, T., Cotrina, M.L., Arcuino, G., Kang, J., Liu, S., Gao, Q., Jiang, L., Li, F., Lichtenberg-Frate, H., Haubrich, S., Willecke, K., Goldman, S.A., and Nedergaard, M. Connexin 43 enhances the adhesivity and mediates the invasion of malignant glioma cells. J Neurosci, 2002. *22*, 4302-4311.
Linkous, A., Balamatsias, D., Snuderl, M., Edwards, L., Miyaguchi, K., Milner, T., Reich, B., Cohen-Gould, L., Storaska, A., Nakayama, Y., Schenkein, E., Singhania, R., Cirigliano, S., Magdeldin, T., Lin, Y., Nanjangud, G., Chadalavada, K., Pisapia, D., Liston, C., and Fine, H.A. Modeling Patient-Derived Glioblastoma with Cerebral Organoids. Cell reports, 2019. *26*, 3203-3211 e3205.
LoRusso, P.M., Rudin, C.M., Reddy, J.C., Tibes, R., Weiss, G.J., Borad, M.J., Hann, C.L., Brahmer, J.R., Chang, I., Darbonne, W.C., Graham, R.A., Zerivitz, K.L., Low, J.A., and Von Hoff, D.D. Phase I trial of hedgehog pathway inhibitor vismodegib (GDC-0449) in patients with refractory, locally advanced or metastatic solid tumors. Clin Cancer Res, 2011. *17*, 2502-2511.

Louis, D.N., Perry, A., Wesseling, P., Brat, D.J., Cree, I.A., Figarella-Branger, D., Hawkins, C., Ng, H.K., Pfister, S.M., Reifenberger, G., Soffietti, R., von Deimling, A., and Ellison, D.W. The 2021 WHO Classification of Tumors of the Central Nervous System: a summary. Neuro Oncol, 2021. *23*, 1231-1251.
Maas, D.A., and Douw, L. Multiscale network neuroscience in neuro-oncology: How tumors, brain networks, and behavior connect across scales. Neurooncol Pract, 2023. *10*, 506-517.
Maglott, D., Ostell, J., Pruitt, K.D., and Tatusova, T. Entrez Gene: gene-centered information at NCBI. Nucleic Acids Res, 2011. *39*, D52-57.
Manjarrez-Marmolejo, J., and Franco-Perez, J. Gap Junction Blockers: An Overview of their Effects on Induced Seizures in Animal Models. Curr Neuropharmacol, 2016. *14*, 759-771.
Mannino, M., and Yarnold, J. Effect of breast-duct anatomy and wound-healing responses on local tumour recurrence after primary surgery for early breast cancer. Lancet Oncol, 2009. *10*, 425-429.
Marquardt, V., Theruvath, J., Pauck, D., Picard, D., Qin, N., Blumel, L., Maue, M., Bartl, J., Ahmadov, U., Langini, M., Meyer, F.D., Cole, A., Cruz-Cruz, J., Graef, C.M., Wolfl, M., Milde, T., Witt, O., Erdreich-Epstein, A., Leprivier, G., Kahlert, U., Stefanski, A., Stuhler, K., Keir, S.T., Bigner, D.D., Hauer, J., Beez, T., Knobbe-Thomsen, C.B., Fischer, U., Felsberg, J., Hansen, F.K., Vibhakar, R., Venkatraman, S., Cheshier, S.H., Reifenberger, G., Borkhardt, A., Kurz, T., Remke, M., and Mitra, S. Tacedinaline (CI-994), a class I HDAC inhibitor, targets intrinsic tumor growth and leptomeningeal dissemination in MYC-driven medulloblastoma while making them susceptible to anti-CD47-induced macrophage phagocytosis via NF-kB-TGM2 driven tumor inflammation. J Immunother Cancer, 2023. *11*.
Masoumi, K.C., Huang, X., Sime, W., Mirkov, A., Munksgaard Thoren, M., Massoumi, R., and Lundgren-Akerlund, E. Integrin alpha10-Antibodies Reduce Glioblastoma Tumor Growth and Cell Migration. Cancers (Basel), 2021. *13*.
Mates, L., Chuah, M.K., Belay, E., Jerchow, B., Manoj, N., Acosta-Sanchez, A., Grzela, D.P., Schmitt, A., Becker, K., Matrai, J., Ma, L., Samara-Kuko, E., Gysemans, C., Pryputniewicz, D., Miskey, C., Fletcher, B., VandenDriessche, T., Ivics, Z., and Izsvak, Z. Molecular evolution of a novel hyperactive Sleeping Beauty transposase enables robust stable gene transfer in vertebrates. Nat Genet, 2009. *41*, 753-761.
Matsuuchi, L., and Naus, C.C. Gap junction proteins on the move: connexins, the cytoskeleton and migration. Biochim Biophys Acta, 2013. *1828*, 94-108.
McCutcheon, S., and Spray, D.C. Glioblastoma-Astrocyte Connexin 43 Gap Junctions Promote Tumor Invasion. Mol Cancer Res, 2022. *20*, 319-331.

Meier, C., and Rosenkranz, K. Cx43 expression and function in the nervous system-implications for stem cell mediated regeneration. Front Physiol, 2014. *5*, 106.
Menyhart, O., and Gyorffy, B. Principles of tumorigenesis and emerging molecular drivers of SHH-activated medulloblastomas. Ann Clin Transl Neurol, 2019. *6*, 990-1005.
Michalski, J.M., Janss, A.J., Vezina, L.G., Smith, K.S., Billups, C.A., Burger, P.C., Embry, L.M., Cullen, P.L., Hardy, K.K., Pomeroy, S.L., Bass, J.K., Perkins, S.M., Merchant, T.E., Colte, P.D., Fitzgerald, T.J., Booth, T.N., Cherlow, J.M., Muraszko, K.M., Hadley, J., Kumar, R., Han, Y., Tarbell, N.J., Fouladi, M., Pollack, I.F., Packer, R.J., Li, Y., Gajjar, A., and Northcott, P.A. Children's Oncology Group Phase III Trial of Reduced-Dose and Reduced-Volume Radiotherapy With Chemotherapy for Newly Diagnosed Average-Risk Medulloblastoma. J Clin Oncol, 2021. *39*, 2685-2697.
Millard, N.E., and De Braganca, K.C. Medulloblastoma. J Child Neurol, 2016. *31*, 1341-1353.
Molina, J.R., and Adjei, A.A. The Ras/Raf/MAPK pathway. J Thorac Oncol, 2006. *1*, 7-9.
Morrissy, A.S., Garzia, L., Shih, D.J., Zuyderduyn, S., Huang, X., Skowron, P., Remke, M., Cavalli, F.M., Ramaswamy, V., Lindsay, P.E., Jelveh, S., Donovan, L.K., Wang, X., Luu, B., Zayne, K., Li, Y., Mayoh, C., Thiessen, N., Mercier, E., Mungall, K.L., Ma, Y., Tse, K., Zeng, T., Shumansky, K., Roth, A.J., Shah, S., Farooq, H., Kijima, N., Holgado, B.L., Lee, J.J., Matan-Lithwick, S., Liu, J., Mack, S.C., Manno, A., Michealraj, K.A., Nor, C., Peacock, J., Qin, L., Reimand, J., Rolider, A., Thompson, Y.Y., Wu, X., Pugh, T., Ally, A., Bilenky, M., Butterfield, Y.S., Carlsen, R., Cheng, Y., Chuah, E., Corbett, R.D., *et al.* Divergent clonal selection dominates medulloblastoma at recurrence. Nature, 2016. *529*, 351-357.
Munksgaard Thoren, M., Chmielarska Masoumi, K., Krona, C., Huang, X., Kundu, S., Schmidt, L., Forsberg-Nilsson, K., Floyd Keep, M., Englund, E., Nelander, S., Holmqvist, B., and Lundgren-Akerlund, E. Integrin alpha10, a Novel Therapeutic Target in Glioblastoma, Regulates Cell Migration, Proliferation, and Survival. Cancers (Basel), 2019. *11*.
Munoz, J.L., Rodriguez-Cruz, V., Greco, S.J., Ramkissoon, S.H., Ligon, K.L., and Rameshwar, P. Temozolomide resistance in glioblastoma cells occurs partly through epidermal growth factor receptor-mediated induction of connexin 43. Cell Death Dis, 2014. *5*, e1145.
Murphy, S.F., Varghese, R.T., Lamouille, S., Guo, S., Pridham, K.J., Kanabur, P., Osimani, A.M., Sharma, S., Jourdan, J., Rodgers, C.M., Simonds, G.R., Gourdie, R.G., and Sheng, Z. Connexin 43 Inhibition Sensitizes Chemoresistant Glioblastoma Cells to Temozolomide. Cancer Res, 2016. *76*, 139-149.

Mynarek, M., Obrecht, D., Sill, M., Sturm, D., Kloth-Stachnau, K., Selt, F., Ecker, J., von Hoff, K., Juhnke, B.O., Goschzik, T., Pietsch, T., Bockmayr, M., Kool, M., von Deimling, A., Witt, O., Schuller, U., Benesch, M., Gerber, N.U., Sahm, F., Jones, D.T.W., Korshunov, A., Pfister, S.M., Rutkowski, S., and Milde, T. Identification of low and very high-risk patients with non-WNT/non-SHH medulloblastoma by improved clinico-molecular stratification of the HIT2000 and I-HIT-MED cohorts. Acta Neuropathol, 2023. *145*, 97-112.

Nicoletti, I., Migliorati, G., Pagliacci, M.C., Grignani, F., and Riccardi, C. A rapid and simple method for measuring thymocyte apoptosis by propidium iodide staining and flow cytometry. J Immunol Methods, 1991. *139*, 271-279.

Nilsen, K.E., Kelso, A.R., and Cock, H.R. Antiepileptic effect of gap-junction blockers in a rat model of refractory focal cortical epilepsy. Epilepsia, 2006. *47*, 1169-1175.

Ning, M.S., Perkins, S.M., Dewees, T., and Shinohara, E.T. Evidence of high mortality in long term survivors of childhood medulloblastoma. J Neurooncol, 2015. *122*, 321-327.

Ning, N., Wen, Y., Li, Y., and Li, J. Meclofenamic acid blocks the gap junction communication between the retinal pigment epithelial cells. Hum Exp Toxicol, 2013. *32*, 1164-1169.

Northcott, P.A., Buchhalter, I., Morrissy, A.S., Hovestadt, V., Weischenfeldt, J., Ehrenberger, T., Grobner, S., Segura-Wang, M., Zichner, T., Rudneva, V.A., Warnatz, H.J., Sidiropoulos, N., Phillips, A.H., Schumacher, S., Kleinheinz, K., Waszak, S.M., Erkek, S., Jones, D.T.W., Worst, B.C., Kool, M., Zapatka, M., Jager, N., Chavez, L., Hutter, B., Bieg, M., Paramasivam, N., Heinold, M., Gu, Z., Ishaque, N., Jager-Schmidt, C., Imbusch, C.D., Jugold, A., Hubschmann, D., Risch, T., Amstislavskiy, V., Gonzalez, F.G.R., Weber, U.D., Wolf, S., Robinson, G.W., Zhou, X., Wu, G., Finkelstein, D., Liu, Y., Cavalli, F.M.G., Luu, B., Ramaswamy, V., Wu, X., Koster, J., Ryzhova, M., Cho, Y.J., *et al.* The whole-genome landscape of medulloblastoma subtypes. Nature, 2017. *547*, 311-317.

Northcott, P.A., Korshunov, A., Witt, H., Hielscher, T., Eberhart, C.G., Mack, S., Bouffet, E., Clifford, S.C., Hawkins, C.E., French, P., Rutka, J.T., Pfister, S., and Taylor, M.D. Medulloblastoma comprises four distinct molecular variants. J Clin Oncol, 2011. *29*, 1408-1414.

Northcott, P.A., Lee, C., Zichner, T., Stutz, A.M., Erkek, S., Kawauchi, D., Shih, D.J., Hovestadt, V., Zapatka, M., Sturm, D., Jones, D.T., Kool, M., Remke, M., Cavalli, F.M., Zuyderduyn, S., Bader, G.D., VandenBerg, S., Esparza, L.A., Ryzhova, M., Wang, W., Wittmann, A., Stark, S., Sieber, L., Seker-Cin, H., Linke, L., Kratochwil, F., Jager, N., Buchhalter, I., Imbusch, C.D., Zipprich, G., Raeder, B., Schmidt, S., Diessl, N., Wolf, S., Wiemann, S., Brors, B., Lawerenz, C., Eils, J., Warnatz, H.J., Risch, T., Yaspo, M.L.,

Weber, U.D., Bartholomae, C.C., von Kalle, C., Turanyi, E., Hauser, P., Sanden, E., Darabi, A., Siesjo, P., Sterba, J.*, et al.* Enhancer hijacking activates GFI1 family oncogenes in medulloblastoma. Nature, 2014. *511*, 428-434.
Northcott, P.A., Robinson, G.W., Kratz, C.P., Mabbott, D.J., Pomeroy, S.L., Clifford, S.C., Rutkowski, S., Ellison, D.W., Malkin, D., Taylor, M.D., Gajjar, A., and Pfister, S.M. Medulloblastoma. Nature Reviews Disease Primers, 2019. *5*, 11.
Oliveira, M.C., Verswyvel, H., Smits, E., Cordeiro, R.M., Bogaerts, A., and Lin, A. The pro- and anti-tumoral properties of gap junctions in cancer and their role in therapeutic strategies. Redox Biol, 2022. *57*, 102503.
Oliveira, R., Christov, C., Guillamo, J.S., de Bouard, S., Palfi, S., Venance, L., Tardy, M., and Peschanski, M. Contribution of gap junctional communication between tumor cells and astroglia to the invasion of the brain parenchyma by human glioblastomas. BMC Cell Biol, 2005. *6*, 7.
Osswald, M., Jung, E., Sahm, F., Solecki, G., Venkataramani, V., Blaes, J., Weil, S., Horstmann, H., Wiestler, B., Syed, M., Huang, L., Ratliff, M., Karimian Jazi, K., Kurz, F.T., Schmenger, T., Lemke, D., Gommel, M., Pauli, M., Liao, Y., Haring, P., Pusch, S., Herl, V., Steinhauser, C., Krunic, D., Jarahian, M., Miletic, H., Berghoff, A.S., Griesbeck, O., Kalamakis, G., Garaschuk, O., Preusser, M., Weiss, S., Liu, H., Heiland, S., Platten, M., Huber, P.E., Kuner, T., von Deimling, A., Wick, W., and Winkler, F. Brain tumour cells interconnect to a functional and resistant network. Nature, 2015. *528*, 93-98.
Pei, Y., Liu, K.W., Wang, J., Garancher, A., Tao, R., Esparza, L.A., Maier, D.L., Udaka, Y.T., Murad, N., Morrissy, S., Seker-Cin, H., Brabetz, S., Qi, L., Kogiso, M., Schubert, S., Olson, J.M., Cho, Y.J., Li, X.N., Crawford, J.R., Levy, M.L., Kool, M., Pfister, S.M., Taylor, M.D., and Wechsler-Reya, R.J. HDAC and PI3K Antagonists Cooperate to Inhibit Growth of MYC-Driven Medulloblastoma. Cancer Cell, 2016. *29*, 311-323.
Penketh, P.G., Baumann, R.P., Ishiguro, K., Shyam, K., Seow, H.A., and Sartorelli, A.C. Lethality to leukemia cell lines of DNA interstrand cross-links generated by Cloretazine derived alkylating species. Leuk Res, 2008. *32*, 1546-1553.
Pettet, G.J., Byrne, H.M., McElwain, D.L., and Norbury, J. A model of wound-healing angiogenesis in soft tissue. Math Biosci, 1996. *136*, 35-63.
Pollmann, M.A., Shao, Q., Laird, D.W., and Sandig, M. Connexin 43 mediated gap junctional communication enhances breast tumor cell diapedesis in culture. Breast Cancer Res, 2005. *7*, R522-534.
Potthoff, A.L., Heiland, D.H., Evert, B.O., Almeida, F.R., Behringer, S.P., Dolf, A., Guresir, A., Guresir, E., Joseph, K., Pietsch, T., Schuss, P., Herrlinger, U., Westhoff, M.A., Vatter, H., Waha, A., and Schneider, M. Inhibition of Gap Junctions Sensitizes Primary Glioblastoma Cells for Temozolomide. Cancers (Basel), 2019. *11*.

Purzner, T., Purzner, J., Buckstaff, T., Cozza, G., Gholamin, S., Rusert, J.M., Hartl, T.A., Sanders, J., Conley, N., Ge, X., Langan, M., Ramaswamy, V., Ellis, L., Litzenburger, U., Bolin, S., Theruvath, J., Nitta, R., Qi, L., Li, X.N., Li, G., Taylor, M.D., Wechsler-Reya, R.J., Pinna, L.A., Cho, Y.J., Fuller, M.T., Elias, J.E., and Scott, M.P. Developmental phosphoproteomics identifies the kinase CK2 as a driver of Hedgehog signaling and a therapeutic target in medulloblastoma. Sci Signal, 2018. *11*.

Qi, C., Acosta Gutierrez, S., Lavriha, P., Othman, A., Lopez-Pigozzi, D., Bayraktar, E., Schuster, D., Picotti, P., Zamboni, N., Bortolozzi, M., Gervasio, F.L., and Korkhov, V.M. Structure of the connexin-43 gap junction channel in a putative closed state. Elife, 2023. *12*.

Rainov, N.G. A phase III clinical evaluation of herpes simplex virus type 1 thymidine kinase and ganciclovir gene therapy as an adjuvant to surgical resection and radiation in adults with previously untreated glioblastoma multiforme. Hum Gene Ther, 2000. *11*, 2389-2401.

Rajagopal, R., Abd-Ghafar, S., Ganesan, D., Bustam Mainudin, A.Z., Wong, K.T., Ramli, N., Jawin, V., Lum, S.H., Yap, T.Y., Bouffet, E., Qaddoumi, I., Krishnan, S., Ariffin, H., and Abdullah, W.A. Challenges of Treating Childhood Medulloblastoma in a Country With Limited Resources: 20 Years of Experience at a Single Tertiary Center in Malaysia. J Glob Oncol, 2017. *3*, 143-156.

Ramaswamy, V., Remke, M., Bouffet, E., Bailey, S., Clifford, S.C., Doz, F., Kool, M., Dufour, C., Vassal, G., Milde, T., Witt, O., von Hoff, K., Pietsch, T., Northcott, P.A., Gajjar, A., Robinson, G.W., Padovani, L., Andre, N., Massimino, M., Pizer, B., Packer, R., Rutkowski, S., Pfister, S.M., Taylor, M.D., and Pomeroy, S.L. Risk stratification of childhood medulloblastoma in the molecular era: the current consensus. Acta Neuropathol, 2016. *131*, 821-831.

Ray, S., Chaturvedi, N.K., Bhakat, K.K., Rizzino, A., and Mahapatra, S. Subgroup-Specific Diagnostic, Prognostic, and Predictive Markers Influencing Pediatric Medulloblastoma Treatment. Diagnostics (Basel), 2021. *12*.

Raza, A., Ghoshal, A., Chockalingam, S., and Ghosh, S.S. Connexin-43 enhances tumor suppressing activity of artesunate via gap junction-dependent as well as independent pathways in human breast cancer cells. Sci Rep, 2017. *7*, 7580.

Revel, J.P., and Karnovsky, M.J. Hexagonal array of subunits in intercellular junctions of the mouse heart and liver. J Cell Biol, 1967. *33*, C7-C12.

Riquelme, M.A., Kar, R., Gu, S., and Jiang, J.X. Antibodies targeting extracellular domain of connexins for studies of hemichannels. Neuropharmacology, 2013. *75*, 525-532.

Robertson, P.L., Muraszko, K.M., Holmes, E.J., Sposto, R., Packer, R.J., Gajjar, A., Dias, M.S., Allen, J.C., and Children's Oncology, G. Incidence and severity of postoperative cerebellar mutism syndrome in children with medulloblastoma: a prospective study by the Children's Oncology Group. J Neurosurg, 2006. *105*, 444-451.
Roehlecke, C., and Schmidt, M.H.H. Tunneling Nanotubes and Tumor Microtubes in Cancer. Cancers (Basel), 2020. *12*.
Rosolen, A., Frascella, E., di Francesco, C., Todesco, A., Petrone, M., Mehtali, M., Zacchello, F., Zanesco, L., and Scarpa, M. In vitro and in vivo antitumor effects of retrovirus-mediated herpes simplex thymidine kinase gene-transfer in human medulloblastoma. Gene Ther, 1998. *5*, 113-120.
Rossi, A., Caracciolo, V., Russo, G., Reiss, K., and Giordano, A. Medulloblastoma: from molecular pathology to therapy. Clin Cancer Res, 2008. *14*, 971-976.
Rutkowski, S., Cohen, B., Finlay, J., Luksch, R., Ridola, V., Valteau-Couanet, D., Hara, J., Garre, M.L., and Grill, J. Medulloblastoma in young children. Pediatr Blood Cancer, 2010. *54*, 635-637.
Salloum, R., Chen, Y., Yasui, Y., Packer, R., Leisenring, W., Wells, E., King, A., Howell, R., Gibson, T.M., Krull, K.R., Robison, L.L., Oeffinger, K.C., Fouladi, M., and Armstrong, G.T. Late Morbidity and Mortality Among Medulloblastoma Survivors Diagnosed Across Three Decades: A Report From the Childhood Cancer Survivor Study. J Clin Oncol, 2019. *37*, 731-740.
Schneider, M., Potthoff, A.L., Evert, B.O., Dicks, M., Ehrentraut, D., Dolf, A., Schmidt, E.N.C., Schafer, N., Borger, V., Pietsch, T., Westhoff, M.A., Guresir, E., Waha, A., Vatter, H., Heiland, D.H., Schuss, P., and Herrlinger, U. Inhibition of Intercellular Cytosolic Traffic via Gap Junctions Reinforces Lomustine-Induced Toxicity in Glioblastoma Independent of MGMT Promoter Methylation Status. Pharmaceuticals (Basel), 2021a. *14*.
Schneider, M., Potthoff, A.L., Karpel-Massler, G., Schuss, P., Siegelin, M.D., Debatin, K.M., Duffau, H., Vatter, H., Herrlinger, U., and Westhoff, M.A. The Alcatraz-Strategy: a roadmap to break the connectivity barrier in malignant brain tumours. Mol Oncol, 2024.
Schneider, M., Vollmer, L., Potthoff, A.L., Ravi, V.M., Evert, B.O., Rahman, M.A., Sarowar, S., Kueckelhaus, J., Will, P., Zurhorst, D., Joseph, K., Maier, J.P., Neidert, N., d'Errico, P., Meyer-Luehmann, M., Hofmann, U.G., Dolf, A., Salomoni, P., Guresir, E., Enger, P.O., Chekenya, M., Pietsch, T., Schuss, P., Schnell, O., Westhoff, M.A., Beck, J., Vatter, H., Waha, A., Herrlinger, U., and Heiland, D.H. Meclofenamate causes loss of cellular tethering and decoupling of functional networks in glioblastoma. Neuro Oncol, 2021b. *23*, 1885-1897.

Schoen, L.F., Craveiro, R.B., Pietsch, T., Moritz, T., Troeger, A., Jordans, S., and Dilloo, D. The PI3K inhibitor pictilisib and the multikinase inhibitors pazopanib and sorafenib have an impact on Rac1 level and migration of medulloblastoma in vitro. J Cell Mol Med, 2022. *26*, 5832-5845.
Sharma, T., Schwalbe, E.C., Williamson, D., Sill, M., Hovestadt, V., Mynarek, M., Rutkowski, S., Robinson, G.W., Gajjar, A., Cavalli, F., Ramaswamy, V., Taylor, M.D., Lindsey, J.C., Hill, R.M., Jager, N., Korshunov, A., Hicks, D., Bailey, S., Kool, M., Chavez, L., Northcott, P.A., Pfister, S.M., and Clifford, S.C. Second-generation molecular subgrouping of medulloblastoma: an international meta-analysis of Group 3 and Group 4 subtypes. Acta Neuropathol, 2019. *138*, 309-326.
Shibayama, J., Paznekas, W., Seki, A., Taffet, S., Jabs, E.W., Delmar, M., and Musa, H. Functional characterization of connexin43 mutations found in patients with oculodentodigital dysplasia. Circ Res, 2005. *96*, e83-91.
Silberstein, S.D. Tonabersat, a novel gap-junction modulator for the prevention of migraine. Cephalalgia, 2009. *29 Suppl 2*, 28-35.
Sin, W.C., Crespin, S., and Mesnil, M. Opposing roles of connexin43 in glioma progression. Biochim Biophys Acta, 2012. *1818*, 2058-2067.
Sinkkonen, S.T., Mansikkamaki, S., Moykkynen, T., Luddens, H., Uusi-Oukari, M., and Korpi, E.R. Receptor subtype-dependent positive and negative modulation of GABA(A) receptor function by niflumic acid, a nonsteroidal anti-inflammatory drug. Mol Pharmacol, 2003. *64*, 753-763.
Slika, H., Shahani, A., Wahi, R., Miller, J., Groves, M., and Tyler, B. Overcoming Treatment Resistance in Medulloblastoma: Underlying Mechanisms and Potential Strategies. Cancers (Basel), 2024. *16*.
Smith, M.J., Beetz, C., Williams, S.G., Bhaskar, S.S., O'Sullivan, J., Anderson, B., Daly, S.B., Urquhart, J.E., Bholah, Z., Oudit, D., Cheesman, E., Kelsey, A., McCabe, M.G., Newman, W.G., and Evans, D.G. Germline mutations in SUFU cause Gorlin syndrome-associated childhood medulloblastoma and redefine the risk associated with PTCH1 mutations. J Clin Oncol, 2014. *32*, 4155-4161.
Srinivas, M., Jannace, T.F., Cocozzelli, A.G., Li, L., Slavi, N., Sellitto, C., and White, T.W. Connexin43 mutations linked to skin disease have augmented hemichannel activity. Sci Rep, 2019. *9*, 19.
Stoletov, K., Strnadel, J., Zardouzian, E., Momiyama, M., Park, F.D., Kelber, J.A., Pizzo, D.P., Hoffman, R., VandenBerg, S.R., and Klemke, R.L. Role of connexins in metastatic breast cancer and melanoma brain colonization. J Cell Sci, 2013. *126*, 904-913.

Sun, P., Liu, Y., Ying, H., and Li, S. Action of db-cAMP on the bystander effect and chemosensitivity through connexin 43 and Bcl-2-mediated pathways in medulloblastoma cells. Oncol Rep, 2012. *28*, 969-976.
Suzuki, H., Kumar, S.A., Shuai, S., Diaz-Navarro, A., Gutierrez-Fernandez, A., De Antonellis, P., Cavalli, F.M.G., Juraschka, K., Farooq, H., Shibahara, I., Vladoiu, M.C., Zhang, J., Abeysundara, N., Przelicki, D., Skowron, P., Gauer, N., Luu, B., Daniels, C., Wu, X., Forget, A., Momin, A., Wang, J., Dong, W., Kim, S.K., Grajkowska, W.A., Jouvet, A., Fevre-Montange, M., Garre, M.L., Nageswara Rao, A.A., Giannini, C., Kros, J.M., French, P.J., Jabado, N., Ng, H.K., Poon, W.S., Eberhart, C.G., Pollack, I.F., Olson, J.M., Weiss, W.A., Kumabe, T., Lopez-Aguilar, E., Lach, B., Massimino, M., Van Meir, E.G., Rubin, J.B., Vibhakar, R., Chambless, L.B., Kijima, N., Klekner, A., Bognar, L.*, et al.* Recurrent noncoding U1 snRNA mutations drive cryptic splicing in SHH medulloblastoma. Nature, 2019. *574*, 707-711.
Takeuchi, N., and Ueda, T. Down-regulation of the mitochondrial translation system during terminal differentiation of HL-60 cells by 12-O-tetradecanoyl-1-phorbol-13-acetate: comparison with the cytoplasmic translation system. J Biol Chem, 2003. *278*, 45318-45324.
Tarzemany, R., Jiang, G., Jiang, J.X., Larjava, H., and Hakkinen, L. Connexin 43 Hemichannels Regulate the Expression of Wound Healing-Associated Genes in Human Gingival Fibroblasts. Sci Rep, 2017. *7*, 14157.
Taylor, M.D., Northcott, P.A., Korshunov, A., Remke, M., Cho, Y.J., Clifford, S.C., Eberhart, C.G., Parsons, D.W., Rutkowski, S., Gajjar, A., Ellison, D.W., Lichter, P., Gilbertson, R.J., Pomeroy, S.L., Kool, M., and Pfister, S.M. Molecular subgroups of medulloblastoma: the current consensus. Acta Neuropathol, 2012. *123*, 465-472.
Tews, D., Pula, T., Funcke, J.B., Jastroch, M., Keuper, M., Debatin, K.M., Wabitsch, M., and Fischer-Posovszky, P. Elevated UCP1 levels are sufficient to improve glucose uptake in human white adipocytes. Redox Biol, 2019. *26*, 101286.
Thompson, E.M., Hielscher, T., Bouffet, E., Remke, M., Luu, B., Gururangan, S., McLendon, R.E., Bigner, D.D., Lipp, E.S., Perreault, S., Cho, Y.J., Grant, G., Kim, S.K., Lee, J.Y., Rao, A.A.N., Giannini, C., Li, K.K.W., Ng, H.K., Yao, Y., Kumabe, T., Tominaga, T., Grajkowska, W.A., Perek-Polnik, M., Low, D.C.Y., Seow, W.T., Chang, K.T.E., Mora, J., Pollack, I.F., Hamilton, R.L., Leary, S., Moore, A.S., Ingram, W.J., Hallahan, A.R., Jouvet, A., Fevre-Montange, M., Vasiljevic, A., Faure-Conter, C., Shofuda, T., Kagawa, N., Hashimoto, N., Jabado, N., Weil, A.G., Gayden, T., Wataya, T., Shalaby, T., Grotzer, M., Zitterbart, K., Sterba, J., Kren, L., Hortobagyi, T.*, et al.* Prognostic value of medulloblastoma extent of resection after accounting for molecular

subgroup: a retrospective integrated clinical and molecular analysis. Lancet Oncol, 2016. *17*, 484-495.
Tishchenko, A., Azorin, D.D., Vidal-Brime, L., Munoz, M.J., Arenas, P.J., Pearce, C., Girao, H., Ramon, Y.C.S., and Aasen, T. Cx43 and Associated Cell Signaling Pathways Regulate Tunneling Nanotubes in Breast Cancer Cells. Cancers (Basel), 2020. *12*.
Turi, Z., Lacey, M., Mistrik, M., and Moudry, P. Impaired ribosome biogenesis: mechanisms and relevance to cancer and aging. Aging (Albany NY), 2019. *11*, 2512-2540.
van Bree, N., and Wilhelm, M. The Tumor Microenvironment of Medulloblastoma: An Intricate Multicellular Network with Therapeutic Potential. Cancers (Basel), 2022. *14*.
Venkataramani, V., Schneider, M., Giordano, F.A., Kuner, T., Wick, W., Herrlinger, U., and Winkler, F. Disconnecting multicellular networks in brain tumours. Nat Rev Cancer, 2022. *22*, 481-491.
Venkatesh, H.S., Morishita, W., Geraghty, A.C., Silverbush, D., Gillespie, S.M., Arzt, M., Tam, L.T., Espenel, C., Ponnuswami, A., Ni, L., Woo, P.J., Taylor, K.R., Agarwal, A., Regev, A., Brang, D., Vogel, H., Hervey-Jumper, S., Bergles, D.E., Suva, M.L., Malenka, R.C., and Monje, M. Electrical and synaptic integration of glioma into neural circuits. Nature, 2019. *573*, 539-545.
Veruki, M.L., and Hartveit, E. Meclofenamic acid blocks electrical synapses of retinal AII amacrine and on-cone bipolar cells. J Neurophysiol, 2009. *101*, 2339-2347.
Vicario, N., Zappala, A., Calabrese, G., Gulino, R., Parenti, C., Gulisano, M., and Parenti, R. Connexins in the Central Nervous System: Physiological Traits and Neuroprotective Targets. Front Physiol, 2017. *8*, 1060.
Vinken, M., Decrock, E., Vanhaecke, T., Leybaert, L., and Rogiers, V. Connexin43 signaling contributes to spontaneous apoptosis in cultures of primary hepatocytes. Toxicol Sci, 2012. *125*, 175-186.
Virtuoso, A., D'Amico, G., Scalia, F., De Luca, C., Papa, M., Maugeri, G., D'Agata, V., Caruso Bavisotto, C., and D'Amico, A.G. The Interplay between Glioblastoma Cells and Tumor Microenvironment: New Perspectives for Early Diagnosis and Targeted Cancer Therapy. Brain Sci, 2024. *14*.
Wallenstein, M.C., and Mauss, E.A. Effect of prostaglandin synthetase inhibitors on experimentally induced convulsions in rats. Pharmacology, 1984. *29*, 85-93.
Wang, D.Q., Wang, Y.Y., Shi, Y.L., Zeng, B., Lin, Z.J., Deng, Q., and Ming, J. Correlation between connexin 43 expression in circulating tumor cells and biological characteristics of breast cancer. Heliyon, 2023. *9*, e18697.

Wang, Y., Li, Y., Jing, Y., Yang, Y., Wang, H., Ismtula, D., and Guo, C. Tubulin alpha-1b chain was identified as a prognosis and immune biomarker in pan-cancer combing with experimental validation in breast cancer. Sci Rep, 2024. *14*, 8201.
Waszak, S.M., Northcott, P.A., Buchhalter, I., Robinson, G.W., Sutter, C., Groebner, S., Grund, K.B., Brugieres, L., Jones, D.T.W., Pajtler, K.W., Morrissy, A.S., Kool, M., Sturm, D., Chavez, L., Ernst, A., Brabetz, S., Hain, M., Zichner, T., Segura-Wang, M., Weischenfeldt, J., Rausch, T., Mardin, B.R., Zhou, X., Baciu, C., Lawerenz, C., Chan, J.A., Varlet, P., Guerrini-Rousseau, L., Fults, D.W., Grajkowska, W., Hauser, P., Jabado, N., Ra, Y.S., Zitterbart, K., Shringarpure, S.S., De La Vega, F.M., Bustamante, C.D., Ng, H.K., Perry, A., MacDonald, T.J., Hernaiz Driever, P., Bendel, A.E., Bowers, D.C., McCowage, G., Chintagumpala, M.M., Cohn, R., Hassall, T., Fleischhack, G., Eggen, T., Wesenberg, F.*, et al.* Spectrum and prevalence of genetic predisposition in medulloblastoma: a retrospective genetic study and prospective validation in a clinical trial cohort. Lancet Oncol, 2018. *19*, 785-798.
Waszak, S.M., Robinson, G.W., Gudenas, B.L., Smith, K.S., Forget, A., Kojic, M., Garcia-Lopez, J., Hadley, J., Hamilton, K.V., Indersie, E., Buchhalter, I., Kerssemakers, J., Jager, N., Sharma, T., Rausch, T., Kool, M., Sturm, D., Jones, D.T.W., Vasilyeva, A., Tatevossian, R.G., Neale, G., Lombard, B., Loew, D., Nakitandwe, J., Rusch, M., Bowers, D.C., Bendel, A., Partap, S., Chintagumpala, M., Crawford, J., Gottardo, N.G., Smith, A., Dufour, C., Rutkowski, S., Eggen, T., Wesenberg, F., Kjaerheim, K., Feychting, M., Lannering, B., Schuz, J., Johansen, C., Andersen, T.V., Roosli, M., Kuehni, C.E., Grotzer, M., Remke, M., Puget, S., Pajtler, K.W., Milde, T., Witt, O.*, et al.* Germline Elongator mutations in Sonic Hedgehog medulloblastoma. Nature, 2020. *580*, 396-401.
Weil, S., Osswald, M., Solecki, G., Grosch, J., Jung, E., Lemke, D., Ratliff, M., Hanggi, D., Wick, W., and Winkler, F. Tumor microtubes convey resistance to surgical lesions and chemotherapy in gliomas. Neuro Oncol, 2017. *19*, 1316-1326.
Weiss, F., Lauffenburger, D., and Friedl, P. Towards targeting of shared mechanisms of cancer metastasis and therapy resistance. Nat Rev Cancer, 2022. *22*, 157-173.
Westhoff, M.A., Zhou, S., Bachem, M.G., Debatin, K.M., and Fulda, S. Identification of a novel switch in the dominant forms of cell adhesion-mediated drug resistance in glioblastoma cells. Oncogene, 2008. *27*, 5169-5181.
White, J., White, M.P.J., Wickremesekera, A., Peng, L., and Gray, C. The tumour microenvironment, treatment resistance and recurrence in glioblastoma. J Transl Med, 2024. *22*, 540.

White, J.S., Su, J.J., Ruark, E.M., Hua, J., Hutson, M.S., and Page-McCaw, A. Wound-Induced Syncytia Outpace Mononucleate Neighbors during Drosophila Wound Repair. bioRxiv, 2023.
Willems, T., Lefebvre, D.J., Neyts, J., and De Clercq, K. Diagnostic performance and application of two commercial cell viability assays in foot-and-mouth disease research. J Virol Methods, 2011. *173*, 108-114.
Wu, D.P., Zhou, Y., Hou, L.X., Zhu, X.X., Yi, W., Yang, S.M., Lin, T.Y., Huang, J.L., Zhang, B., and Yin, X.X. Cx43 deficiency confers EMT-mediated tamoxifen resistance to breast cancer via c-Src/PI3K/Akt pathway. Int J Biol Sci, 2021. *17*, 2380-2398.
Wu, K.S., Sung, S.Y., Huang, M.H., Lin, Y.L., Chang, C.C., Fang, C.L., Wong, T.T., Chen, H.H., and Tsai, M.L. Clinical and Molecular Features in Medulloblastomas Subtypes in Children in a Cohort in Taiwan. Cancers (Basel), 2022. *14*.
Xu, H., Wang, M., Li, Y., Shi, M., Wang, Z., Cao, C., Hong, Y., Hu, B., Zhu, H., Zhao, Z., Chu, X., Zhu, F., Deng, X., Wu, J., Zhao, F., Guo, J., Wang, Y., Pei, G., Zhu, F., Wang, X., Yang, J., Yao, Y., and Zeng, R. Blocking connexin 43 and its promotion of ATP release from renal tubular epithelial cells ameliorates renal fibrosis. Cell Death Dis, 2022. *13*, 511.
Xue, M., and Jackson, C.J. Extracellular Matrix Reorganization During Wound Healing and Its Impact on Abnormal Scarring. Adv Wound Care (New Rochelle), 2015. *4*, 119-136.
Young, S., Phaterpekar, K., Tsang, D.S., Boldt, G., and Bauman, G.S. Proton Radiotherapy for Management of Medulloblastoma: A Systematic Review of Clinical Outcomes. Adv Radiat Oncol, 2023. *8*, 101189.
Zhao, T., Wang, C., Zhao, N., Qiao, G., Hua, J., Meng, D., Liu, L., Zhong, B., Liu, M., Wang, Y., Bai, C., and Li, Y. CYB561 promotes HER2+ breast cancer proliferation by inhibiting H2AFY degradation. Cell Death Discov, 2024. *10*, 38.
Zhou, J.X., Taramelli, R., Pedrini, E., Knijnenburg, T., and Huang, S. Extracting Intercellular Signaling Network of Cancer Tissues using Ligand-Receptor Expression Patterns from Whole-tumor and Single-cell Transcriptomes. Sci Rep, 2017. *7*, 8815.
Zhou, M., Zheng, M., Zhou, X., Tian, S., Yang, X., Ning, Y., Li, Y., and Zhang, S. The roles of connexins and gap junctions in the progression of cancer. Cell Commun Signal, 2023. *21*, 8.
Zoteva, V., De Meulenaere, V., Vanhove, C., Leybaert, L., Raedt, R., Pieters, L., Vral, A., Boterberg, T., and Deblaere, K. Integrating and optimizing tonabersat in standard glioblastoma therapy: A preclinical study. PLoS One, 2024. *19*, e0300552.

9. Acknowledgments

I do not like studying. Therefore, I had never imagined that I would be sitting here writing my doctoral thesis. In October 2018, I left my lovely family and so-called nice job in Taiwan and came to Germany for my Master's at Uni Bonn. I did not know that after finishing my Master's, I would be offered a PhD position in PD Dr. med. Matthias Schneider's lab, introduced by Prof. Dr. Michael Hölzel, who is also my second thesis reviewer. I am honored to have completed my projects under the leadership of Prof. Dr. med. Hartmut Vatter.

First of all, I want to thank Matthias—not only for offering me this opportunity but also for helping me with his genuinely kind heart. I have never doubted that Matthias is a great boss because he is someone with kindness and warmth whom I can fully trust. Many people could hardly believe he is my boss because he is so young and already so successful in his career. What I admire most about him is his passion and even craziness for research. In some ways, I am also a bit jealous that he has found this obsession in his life. I am especially grateful that he always allowed me to contact him anytime—even early in the morning when I knew that my grandpa had passed away (though I still don't know why I called him at that moment). I also know it was not easy for him to revise my thesis, but through his revisions, I gained a deeper understanding of the meaning of my project, and I'm glad we went through this process together.

Starting during COVID was not easy. Although I had already earned a master's degree, everything about my PhD project felt completely new to me (and to everyone in the lab). Fortunately, Dr. med. Anna-Laura Potthoff, my young supervisor, had a gap month to organize EVERYTHING for me—even a coffee machine! She also helped me get into the workflow. I am truly grateful for her constant support, whether it was offering help, cheering me up, or comforting me when I couldn't get any significant data from flow cytometry.

Sometimes I forget how young she is because she has achieved so much at her age. Her mature attitude, extraordinary memory, and impressive IT skills never fail to amaze me. She also plays the role of an excellent note-taker and translator, quickly explaining to Matthias what I have just reported.

Next, I want to thank Barbara Pregler, who joined me after one and half year but supported me so much. She not only helped me analyze my RNA-seq data but also stood by me during times when I felt frustrated and disappointed with relationships. I am especially grateful to her for being there before Christmas 2023 and on the day my grandpa passed away. Without her, I wouldn't have been able to finish my progress report slides or stay focused on my work. Even though we shared the same office for only half a year, it was a really nice time. We talked about our experimental progress—and, of course, some gossip... haha. I won't forget how loud we laughed in the office.

I also want to thank everyone who works in Neuropathology, including Prof. Dr. med. Pietsch and Prof. Dr. rer. nat. Waha, Anja, Dorota, Lyn, Tobias, Verena, and everyone else were always so nice and friendly, helping me with any questions I had and offering active support. A special thanks to Rebecca Klein, who started around the same time as me, and with whom I always encouraged each other. I want to thank her for the great times we shared (including her birthday party) and the support she gave me when I needed it. Hans im Glück is always the place where we could laugh, drink, and gossip the whole evening.

Xinyu Han and Yanxia Liu are very important friends to me during my PhD. They gave me much energy when I was down. We encouraged each other and cooked hotpot together. Also, thanks to Han, my painful Western blots were finally completed. My daily routine was going to Han's office to complain and going to the gym with Yanxia. These memories are very meaningful to me.

Moreover, I sincerely want to thank Elena Schmidt, who provided many protocols and technical assistance to help me start with my projects. Susanna Ng is a very friendly and professional person who helped me establish a protocol and offered me so much assistance. Hannah Strahl shared everything she knew with me and helped me generate the Cx43 KO clone of MB cell lines. Sandra Theil always smiles and welcomes me to their lab to use the equipment.

I would like to thank Dr. Joachim Mehler. Although he had the bad luck to meet me during this period, he has always given me encouragement and positive energy whenever I doubted myself. He has faith in me and has endured my bad moods and my stress during the writing process and job applications. He has done everything to make me feel better, taking me into his arms, wiping away my tears and snivels, and supporting me when I needed it. I truly appreciate having his companionship during this time.

The most important people I want to thank are my family in Taiwan. I really want them to be proud of me, and I know they are. During many difficult moments, especially the 2.5 years I couldn’t see them because of Covid, the connections with them kept me going. Stacy always listens when I cry, shouts with me, and comforts me, sending cards to cheer me. I really appreciate that she is always there for me, no matter the time difference or distance. Also, my friends Anna, Farrah, Ping-hui, and so many others have supported me in every way whenever I needed it. Thanks to Cindy and Shu-Yu for helping me with the final check in such limited time.

Last, I thank myself for keeping curiosity, energy, and kindness toward this world. I am lucky enough to have so many great people in my life and have received so much help. It was challenging, but I never gave up! I am very proud of myself.

This thesis is also dedicated to my lovely grandpa. I wish you could see it now. I believe you would be proud of me as well.